

NAM

An estimate of the earthquake hypocenter locations in the Groningen Gas Field

Matt Pickering

Datum June 2015

Editors Jan van Elk & Dirk Doornhof

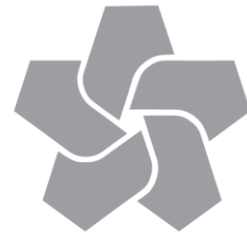
General Introduction

In 2013 NAM installed a string of geophones at reservoir depth in two existing monitoring wells; Stedum-1 and Zeerijp-1. The geophones in these two wells have monitored seismicity in the Loppersum area and delivered valuable information.

Based on this data the hypocentres of the earthquakes in this area can be assessed more accurately than with the geophone network of shallow wells. In particular, the vertical depth can also be determined. This allows better placement of the earthquake hypocenters at faults in the reservoir. Several methods for determination of the hypocentres have been tried.

1. Magnitude, a company specialized in seismic analysis reviews all seismic events and determines the hypocenter location of each recorded earthquake.
2. In the Shell laboratory in Rijswijk the seismic events before October 2014 have been analysed. The current report describes this assessment.
3. Both previous methods are based on picking of arrival times. Additionally, in Shell research a method is developed to determine the hypocenter based on Full Waveform Inversion. This method demands a lot of computer power. Hypocenters for the strongest 7 events have been accurately determined using this method.

These measurements will be important to gain an understanding of the rupture process and help to provide an event database that can be used for testing geomechanical modelling results.



NAM

Title	An estimate of the earthquake hypocenter locations in the Groningen Gas Field		Date	June 2015
			Initiator	NAM
Autor(s)	Matt Pickering	Editors	Jan van Elk Dirk Doornhof	
Organisation		Organisation	NAM	
Place in the Study and Data Acquisition program	<p><u>Study Theme:</u> Seismological modelling and Geomechanics</p> <p><u>Comment:</u> This report describes a methodology for determination of the hypocentres of small earthquakes in the Loppersum area from the data collected by the geophones placed in deep wells.</p>			
Directly linked research	<p>(1) Alternative methods for determination of hypocentre location developed by magnitude based on event picking.</p> <p>(2) Alternative methods for determination of hypocentre location based in full wave form inversion.</p> <p>(3) Geomechanical modelling of rupture processes on faults.</p>			
Used Data	Data collection.			
Associated Organisations	Baker-Hughes, Magnitude, Shell laboratory Rijswijk.			
Assurance	-			

Restricted

A re-estimate of the earthquake hypocenter locations in the Groningen Gas Field.

**by
Matt Pickering**

This document is classified as Restricted. Access is allowed to Shell personnel, designated Associate Companies and Contractors working on Shell projects who have signed a confidentiality agreement with a Shell Group Company. 'Shell Personnel' includes all staff with a personal contract with a Shell Group Company. Issuance of this document is restricted to staff employed by a Shell Group Company. Neither the whole nor any part of this document may be disclosed to Non-Shell Personnel without the prior written consent of the copyright owners.

Copyright SIEP B.V. 2014.

Shell International Exploration and Production B.V., Rijswijk

Further electronic copies can be obtained from the Global Information Centre.

Editorial note

This report was prepared by Matthew Pickering, a student on the Leeds University MSc course in Exploration Geophysics who worked as an intern in Shell Rijswijk. In order to meet the University's requirement for an independently prepared report which could be assessed as part of the course and contribute to the final appraisal, this report has not been through the internal peer reviews that are a requirement for Shell reports. Only minimal light editing has been carried out after submission to the University.

Steve Oates, Shell Global Solutions, Rijswijk, October 2014

Abstract

Earthquakes located within the Groningen gas field (north of the Netherlands) are assumed by the field operator NAM to be occurring in and around the Rotliegend reservoir, due to production induced seismicity. This study reprocessed 32 of the seismograms of the induced seismic events obtained from the Stedum-1 and Zeerijp-1 reservoir-level arrays in the study area of the Groningen field to obtain estimates for the earthquake hypocenters. Previous work on this dataset by a microseismic service company had produced anomalous depth estimates, justifying a reassessment of the earthquake event locations. Forward modelling of the events and analysis of the source vector, polarity and linearity of the waveforms were used to determine P and S wave direct arrival times in the seismograms. This was used to estimate the earthquake hypocenters by arrival time inversion using Tian's method of ray tracing, and the grid search location algorithm. All the events were determined to have occurred at a depth within 100 metres of the Rotliegend reservoir, with a mean depth of 2921m approximately corresponding to the reservoir centre.

Table of contents

Abstract	II
1. Introduction	1
1.1. Groningen Gas field overview	1
1.2. Seismicity background	1
1.3. Seismic monitoring studies	2
1.4. Aims & objectives	2
1.5. Software overview	2
2. Geological setting	3
2.1. Overview	3
2.2. Field stratigraphy	3
2.2.1. <i>Zechstein</i>	4
2.2.2. <i>Rotliegend</i>	4
2.2.3. <i>Carboniferous</i>	4
3. Theory	5
3.1. Geomechanics	5
3.1.1. <i>Compaction and seismic moment</i>	5
3.1.2. <i>Expected earthquakes depths</i>	5
3.1.3. <i>Nature of seismicity</i>	5
3.1.4. <i>Faulting</i>	6
3.1.5. <i>Moment Magnitude</i>	7
3.1.6. <i>Maximum magnitude</i>	7
3.2. Raytracing	8
3.2.1. <i>Ray-tracing methods</i>	8
3.2.2. <i>Tian ray-tracing overview</i>	8
3.3. Source vector determination	9
3.4. Location methods	9
3.4.1. <i>Geiger method of event location</i>	10
3.4.2. <i>Collapsing grid search method</i>	10
3.4.3. <i>Errors</i>	11
3.4.4. <i>Relative location methods</i>	11
4. Data	13
4.1. Data Acquisition	13
4.1.1. <i>Monitoring arrays</i>	13
4.1.2. <i>Well Location</i>	13
4.1.3. <i>Sensor</i>	13
4.1.4. <i>Equipment failures</i>	13
4.1.5. <i>Data recording periods</i>	13
4.1.6. <i>Data format</i>	14
4.2. Data pre-processing	14

4.2.1.	<i>Data selection</i>	14
4.2.2.	<i>Attenuation</i>	14
4.2.3.	<i>Bandpass filter</i>	14
5.	Analysis of Magnitude's results	15
6.	Waveform interpretation Methods	17
6.1.	Overview	17
6.2.	Finite difference modelling	17
6.3.	InSite event picking	22
6.3.1.	<i>Arrival time foreword modelling</i>	22
6.3.2.	<i>Layer discrimination</i>	22
6.4.	Use of source angle	22
6.4.1.	<i>Linearity</i>	24
6.4.2.	<i>Waveform polarisation</i>	25
7.	Results	27
8.	Discussion on results	30
8.1.	Overview	30
8.2.	Result accuracy	30
8.2.1.	<i>Uncertainty estimates</i>	30
8.2.2.	<i>Limitations of velocity model</i>	31
8.3.	Use of grid search method	32
8.4.	Analysis of relative location methods	32
8.5.	Azimuth & dip angle	32
8.6.	Evidence of Faults	32
8.7.	Discussion on Magnitude's work	33
8.8.	Future work & and result implications	33
9.	Conclusion	35
10.	References	36
	APPENDIX	38
A1.1.	Table of Results	39
A1.2.	Geophone information and orientations	40
A1.2.1.	Check shots	40
A1.2.2.	Orientation coordinates & Geophone information	40
A1.3.	Analysis of Magnitude's Data	46
A1.3.1.	Example interpreted seismograms	47
	<i>22/03/14 15:10:08</i>	47
A1.3.2.		47
	<i>25/03/14 13:20:56</i>	48
A1.3.3.	Effect of propagation distance on waveform	49
A1.3.4.	Magnitudes event depths	50
A1.3.5.	Gutenberg-Richter plot	50
A1.4.	Further finite difference modelling analysis	51

A1.4.1.	Source at 3000m	51
A1.4.2.	Source at 2800m	52
A1.4.3.	Source at 4600m	53
A1.5.	Layer discrimination from waveform character	54
A1.6.	Example trace interpretation	56
A1.6.1.	Event 25/04/14 13:20:56	56
A1.6.2.	Event 22/03/14	58
A1.6.3.	Event 23/03/14 02:23:55 Stedum Well	60
A1.6.4.	Event 15/04/14 09:43:24 Stedum Well	62
A1.6.5.	Event 01/04/14 20:08:56 Stedum well	64
A1.7.	Velocity model	66
A1.7.1.	Sonic logs	66
A1.7.2.	InSite	67
A1.7.3.	Finite difference modelling	68
A1.8.	Analysis of event 09/04/14. Accuracy determination.	69
A1.9.	Trace Arrival time P and S picks	71
	15/12/13 06:48:25	71
	15/12/13 07:39:55	72
	12/04/14 05:36:04	73
	12/04/14 12:56:10	74
	17/04/14 20:21:01	75
	22/03/14 17:16:15	76
	22/04/14 03:13:14	77
	30/11/13 19:29:01	78
	01/04/14 18:35:13	79
	01/04/14 14:13:06	80
	06/04/14 14:47:18	81
	10/04/14 20:56:15	82
	11/04/14 20:48:31	83
	03/05/14 20:39:06	84
	17/12/13 21:37:55	85
	01/12/13 09:21:03	86
	23/03/14 02:23:55	87
	21/03/14 11:28:25	88
	20/04/14 11:20:14	89
	20/04/14 08:36:00	90
	17/04/14 01:46:35	91
	06/05/14 03:23:58	92
	06/05/14 11:31:57	93
	Bibliographic information	94

- Figure 1: Epicentre locations of earthquakes in the north of the Netherlands recorded by KNMI. Gas fields are coloured in green (NAM, November 2013). 1
- Figure 2: shows the subsurface structure of the Groningen field highlighting the Carboniferous, Rotliegend reservoir and the basal Anhydrite. The seismic line is aligned along the direction connecting the Stedum (STD) and Zeerijp (ZRP) wells. Image provided by NAM. 3
- Figure 3: *shows the increase in the cumulative seismic energy release and production through time* (Ministry of Economic affairs, 2013). 5
- Figure 4: (NAM, November 2013): shows the normalised compaction over the Groningen field. Earthquake epicentres are dotted on the map in black and mostly correspond to the areas where the highest level of compaction has occurred. 6
- Figure 5: *shows the location of the two monitoring wells and the fault network through the Groningen field. The Stedum-1 and Zeerijp-1 well locations are indicated by the red and blue circle respectively* (NAM, November 2013). 7
- Figure 6 shows a 2D representation of the identification of an event location observed from two receivers using the source azimuth. 9
- Figure 7: shows the functionality of the collapsing grid search method used in InSite. The volume is described into grid point positions and the residual is calculated at each point. This grid is then collapsed by a specified value to refine the search (Applied seismology Consultants, 2014). 11
- Figure 8: shows the locations of a subset events processed by Magnitude showing their estimated event hypocenters and error surface. Image courtesy of Magnitude. 15
- Figure 9: Histogram of all events depths determined by Magnitude. 15
- Figure 10 Image courtesy of Magnitude: shows the estimation of the event depth plotted against the source receiver distance observed. The red points show their previous depth estimates based on the arrival time inversion using P and S wave arrival times; the green dots show their revised estimates as of 04/08/14 based on using arrival time picks of P, S and S to P conversions. 16
- Figure 11 results of finite difference modelling of an event at a depth of 2900m showing the propagation of a wave through the subsurface at source-receiver distances of under 1 Km. 20
- Figure 12 the results of the finite difference modelling of an event at a depth of 2900m showing the propagation of a wave through the subsurface at source receiver spacing's of over 1Km. 21
- Figure 13 Shows a the direct arrival pick made on the event 22/03/14 15:10:08 made on the P component of the 6th geophone on the Zeerijp well. 23
- Figure 14 the dip angle for the p wave for the pick made in Figure 13. The image shows the source angle on the up-east plane. 23
- Figure 15 shows the azimuth of the p wave for pick given in Figure 13. The image shows the source angle on the north-east plane 23
- Figure 16 shows a P-Wave pick made on the headwaves on the event 22/03/14 15:10:08 on the 6th geophone of the Zeerijp well. 24
- Figure 17 shows the dip of the source vector on the headwaves pick made in Figure 16 pointing towards the vertical. The image shows the source angle on the East-Up plane. 24

Figure 18 shows a P-pick made after the direct arrival to highlight the effect on the wave linearity.	25
Figure 19 shows the effect on the p wave motion of the particles in terms of north-east plane and the vertical-east plane at the time located in Figure 18.	25
Figure 20 shows how the polarisation of the waveform was used to judge direct P arrival time. Image shows the response from the rotated P component of the 7 th geophone of the Zeerijp well on the event 21/03/14 11:28:25.	26
Figure 21 shows how the polarisation of the waveform was used to judge direct S arrival time. Image shows the response from the rotated S _H component of the 7 th geophone of the Zeerijp well on the event 21/03/14 11:28:25.	26
Figure 22 shows the northing and easting components of the event epicentres located in this project.	27
Figure 23 shows the locations of the seismic events in terms of easting and true vertical depth below sea level. The top and base of the reservoir is shown in addition to the location of the Stedum (STD) and Zeerijp well (ZRP).	28
Figure 24: shows a histogram of the estimated event depths located by Magnitude with an estimated magnitude above 0.	50
Figure 25 Image shows a Gutenberg-Richter plot of the events with a magnitude greater than 0. Magnitude was plotted against the logarithm of the fraction of the total events with a magnitude greater than this value. This produced a 'b' value of 0.97. This figure was produced using the moment magnitudes quoted by the service company Magnitude.	50
Figure 26 shows the P wave sonic log from the Zeerijp-1 well array covering depths from the top of the Basal Anhydrite to the base of the well in the Carboniferous	66
Figure 27 shows the abbreviated P wave sonic log from the Stedum-1 well array covering depths from the top of the Basal Anhydrite to the base of the well in the Carboniferous	66
Figure 28 shows the velocities used in the finite difference modelling. A constant gradient was used in the velocity model.	68

1. Introduction

1.1. Groningen Gas field overview

Located in the North-East of the Netherlands, the Groningen field is operated by Nederlandse Aardolie Maatschappij (NAM) a joint venture of Shell and Exxon Mobil. Covering an area of 900 square kilometres, the field is the one of the largest gas reservoirs in the world. Originally containing 2.9 trillion m^3 of recoverable gas reserves of which 60% has been produced and with the remaining gas expected to be extracted over the next 50 years (Grotsch.J, 2011).

1.2. Seismicity background

Since 1986, gas production in the Groningen field has been known to have caused earthquakes in the area (Dost, Goutbeek, Eck, & Kraaijpoel, 2010). As the region is not affected by tectonic movement and no notable earthquakes were recorded before gas extraction began, it can be assumed that the observed seismicity is directly caused by gas production. Due to the shallow depth of the seismic events, thought to originate from the depth of the reservoir around 2.6.-3.1Km, large peak ground accelerations are observed (PGA) in addition to short pulse durations causing a larger amount of damage compared to earthquakes of a similar magnitudes caused by deeper tectonic movement.

In more recent years, earthquakes felt at ground level have increased both in frequency and magnitude, adding to the concern of residents in the area. In August 2012, an earthquake of magnitude 3.6 was recorded causing some structural damage close to its epicentre (NAM, November 2013). The earthquakes have provoked intense public pressure, demonstrations, and widespread media coverage. The Dutch government made the decision to both cut production on the Groningen field and provide compensation to those affected.

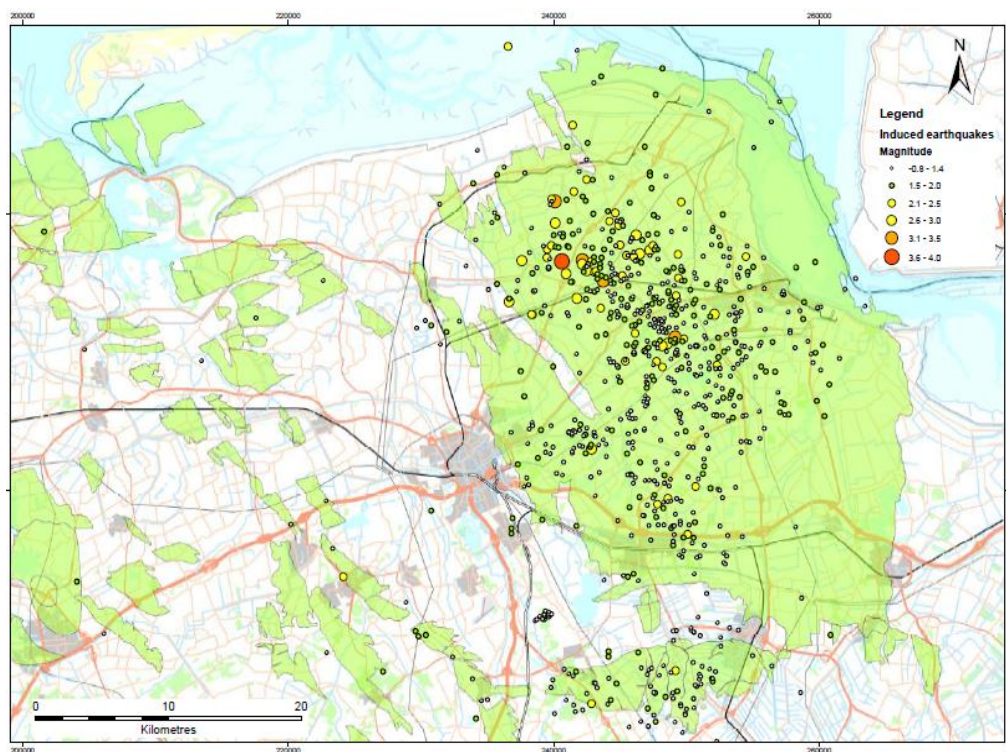


Figure 1: Epicentre locations of earthquakes in the north of the Netherlands recorded by KNMI. Gas fields are coloured in green (NAM, November 2013).

1.3. Seismic monitoring studies

In 1995, the Dutch Meteorological Institute (KNMI) installed 20 passive seismic monitoring borehole stations located across the field¹. Between April 1995 and October 2012, these have recorded 188 seismic events greater than a magnitude of 1.5M (NAM, November 2013). The uncertainties in the location of the epicentres of the seismic events have been large, with uncertainties up to 500m laterally and several kilometres vertically.

To obtain better location estimates of the seismic events, and specifically to determine the depths of the events, the field operator NAM has installed two reservoir level geophone arrays in the Stedum-1 and Zeerijp-1 wells to acquire microseismic data. This aimed to provide more accurate event locations in a small volume of the subsurface near the centre of the field where the greatest seismicity has been observed.

Magnitude, a microseismic service company, was contracted to process this deep well microseismic data in order to obtain location estimates for the seismic events. It was predicted that the seismicity was originating from in and around the reservoir due to gas extraction (see section 3.1.1). However, Magnitude's results gave hypocenters for the majority of the larger events deep within the Carboniferous, 1-2km below the Rotliegend reservoir (see section 4.2). A smaller number of events, recorded at a close distance to one or other of the monitoring wells, were located inside the reservoir. It was found that Magnitude's locations for the larger events fall on a common sloping trajectory, strongly suggesting that the deep locations are erroneous and possibly explained by incorrect straight extrapolation of rays associated with interface or turning waves.

NAM is currently examining the causes and mitigation measures for the earthquakes in the Groningen field and requires the location of the earthquakes to be identified accurately. The operator is also under significant public pressure to disclose the depths of the earthquakes.

1.4. Aims & objectives

The aim of this project was to examine the microseismic data obtained from the two reservoir level monitoring arrays, to provide an independent view on the location of the seismic events. The main area of interest of this work will be on the depths of the events. This will aim to conclude whether the seismic events are located at a large range of depths spanning from the top of the reservoir to several kilometres into the Carboniferous below as Magnitude's initial results have suggested, or whether the events are located at around reservoir level.

1.5. Software overview

The software InSite, produced by Applied Seismology consultants (ASC) was used to process the microseismic data, and provide location estimates using arrival time inversion. Full details of the software functionality can be found in the InSite software manual (Applied seismology Consultants, 2014). A shell in-house finite difference modelling software program known as WFD was used to model the waveform propagation.

¹ Editor's comment: see "*Monitoring induced seismicity in the North of the Netherlands: status report 2010*" KNMI Scientific report WR 2012-03, by Bernard Dost, Femke Goutbeek, Torild van Eck and Dirk Kraaijpoel for a more complete description of the deployment and evolution of the KNMI monitoring network.

2. Geological setting

2.1. Overview

The Groningen field is situated in the ‘Groningen high’, a structural high point that has existed as a stable block since the Kimmerian inversion. The Permian Rotliegend Slochteren formation forms the main gas bearing reservoir in the Groningen field whilst further minor quantities of gas are found in the underlying Carboniferous (Grotsch.J, 2011) The reservoir is sealed from above by Zechstein evaporates. The field is bounded by the Lauwerzee trough to the west and the Ems Graben and Lower Saxony basin to the east of the field (Grotsch.J, 2011). The reservoir is predominantly fault bounded around the rest of the field and confined by dip closure in the north (Grotsch.J, 2011). A full geological description of the field can be found from Stauble and Milius (Stauble & Milius, 1970).

The crucial formations in the Groningen field which play a role in the identification of the microseismic events are the Rotliegend, the Basal anhydrite layer capping this Reservoir and the Carboniferous layer below. Table 1 shows the depths of the top of these interfaces determined at the Stedum and Zeerijp well locations. Details on the velocity can be found in the appendix.

2.2. Field stratigraphy

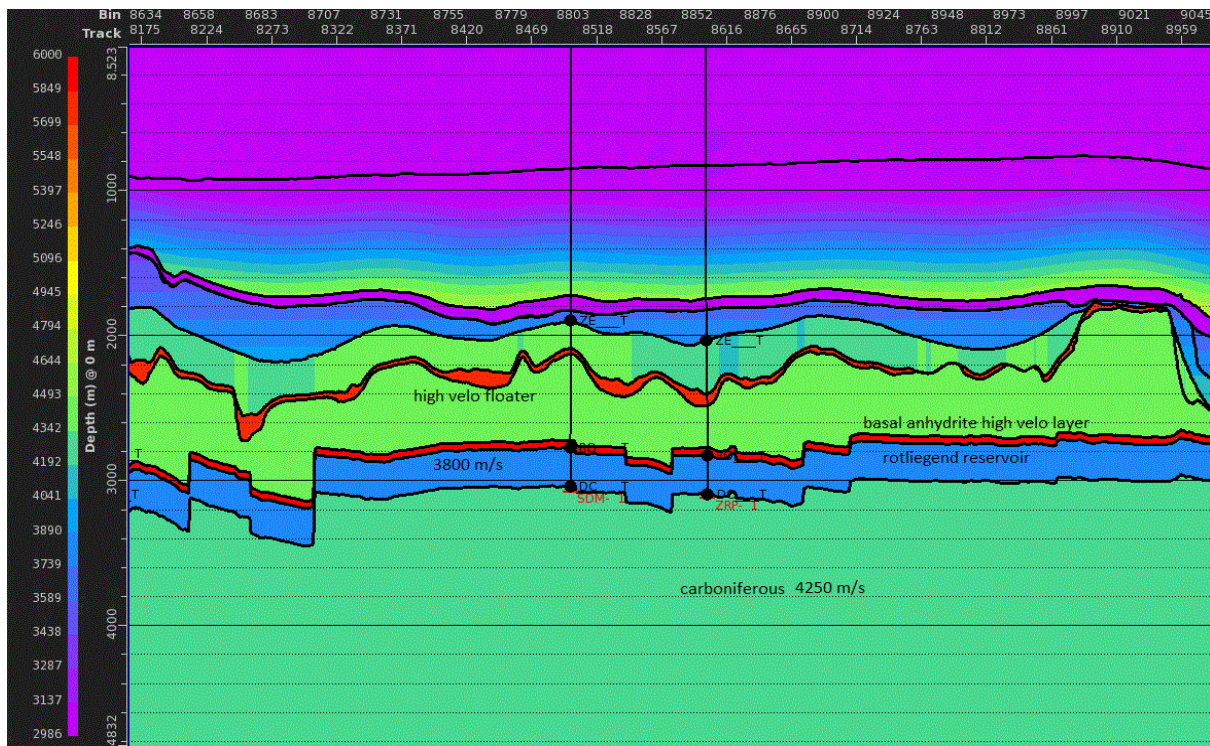


Figure 2: shows the subsurface structure of the Groningen field highlighting the Carboniferous, Rotliegend reservoir and the basal Anhydrite. The seismic line is aligned along the direction connecting the Stedum (STD) and Zeerijp (ZRP) wells. Image provided by NAM.

2.2.1. Zechstein

The Zechstein is formed predominantly of evaporate deposits. A 50m thick basal anhydrite layer forms the lowest interval of the Zechstein overlying the Rotliegend below. The high density of this layer combined with its high p-wave velocity of 6km/s results in a strong acoustic impedance contrast between the Rotliegend and Zechstein Anhydrite layers. This interface acts as a strong seismic reflector, which was predicted to cause difficulty in the identification of the direct arrivals in the microseismic data, due to high amplitude reflections and mode conversions at this interface.

2.2.2. Rotliegend

The upper Slochteren formation is formed largely of Aeolian sandstone; whilst the lower half is formed from fluvial deposits of sand, conglomerates and clay (Stauble & Milius, 1970). The best reservoir quality is found in the Aeolian sandstone in the central parts of the field where the porosity can be up to 25% (Grotsch.J, 2011). The porosity decreases towards the north as the shale content increases and around the southern margin of the field due to conglomerate rich facies (Grotsch.J, 2011). The Ten-Boer member of the Rotliegend is formed from beds of silty to fine sandy claystone (Stauble & Milius, 1970).

The reservoir rock properties of the field also play a contributing factor in the induced seismicity. It is expected that the central regions of the Slochteren, where the porosities are the highest, have the greatest potential for reservoir compaction from gas extraction (NAM, November 2013). Figure 4 appears to support this hypothesis by showing that the earthquakes have largely occurred in regions with the highest level of compaction.

This Rotliegend formation has an average p wave velocity of 3800m/s with the velocity falling towards its centre to approximately 3500m/s. A sonic log covering the depths of interest in the field can be found in the appendix. The thickness of the Rotliegend varies across the field from a thickness of 140m in the SSE to 300m in the north NNW of the field (NAM, November 2013). The top of the reservoir is found at 2768.9m at the Stedum well location and at 2826.1m at the Zeerijp well.

2.2.3. Carboniferous

The carboniferous deposits encountered in the field range from the Westphalian-A to the Westphalian-D era, formed from redbed facies of sandstone and shales (Stauble & Milius, 1970). The P wave velocity in the formation increases gradually from the reservoir to the Carboniferous to a velocity of approximately 4200m/s.

Interface top	Stedum (m)	Zeerijp (m)
Basal Anhydrite	2099.8	2383.4
Halite	2144.8	2493.3
Basal Anhydrite	2720.0	2775.3
Rotliegend	2768.9	2826.1
Carboniferous	3040.0	3093.0

Table 1 shows the heights of the layer tops of the key interfaces in the Groningen field at each well location. Heights are true vertical depth below sea level.

3. Theory

3.1. Geomechanics

3.1.1. Compaction and seismic moment

The decrease in bulk reservoir volume due to gas production is accepted by the operator NAM to be responsible for the seismicity observed in the Groningen field (NAM, November 2013). The extraction of gas has reduced the rock pore pressure inside the reservoir; as the pressure of the overburden remains constant, the effective pressure on the depleted reservoir increases. This effect exerts a vertical strain on the rock and has resulted in a predominantly vertical compaction of the reservoir in the Groningen field (Ketelaar, 2009). The compaction of the reservoir alters the stress field across the rock; this can cause fault slip to occur whereby elastic strain in the rock overcomes the frictional force across a fault plane.

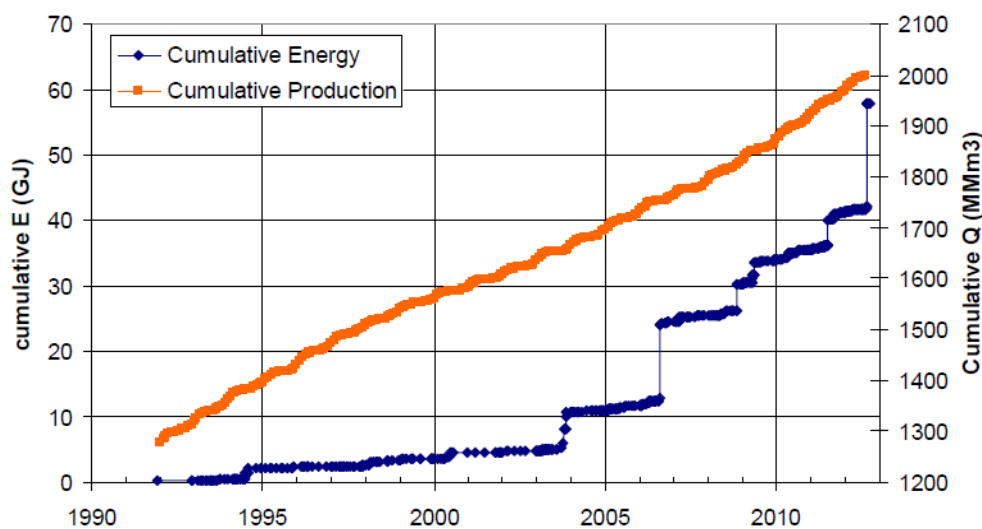


Figure 3: shows the increase in the cumulative seismic energy release and production through time (Ministry of Economic affairs, 2013).

Figure 3 above shows that the rate of seismic energy release by the Groningen field has increased with time particularly in the period from 2003 onwards. It is worth noting that cumulative release of the seismic moment is dominated by high magnitude events (above a magnitude of 3).

3.1.2. Expected earthquakes depths

Due to the effect of reservoir compaction, the seismic events are expected to originate from in and around the reservoir. Reservoir compaction causes subsidence at the top of the reservoir and uplift at its base. Therefore, events may also be expected to extend through the upper Carboniferous due to the stress caused by the reservoir subsidence. Faults may also extend from the reservoir itself into this layer. It is possible that events may also occur within the Zechstein salt. However, the flow of salt under pressure can alleviate stresses within this layer; this may prevent the build up of the stress required for a large earthquake to occur in the Zechstein.

3.1.3. Nature of seismicity

There is no record of seismicity in the region before gas extraction, from either natural events or mining (Houtgast, 1991). It is therefore assumed that there is no potential for triggered seismic events based on the fact that there are no faults in a naturally critically stressed state whereby further strain could potentially trigger a larger release of stress (Eck, Goutbeek, Haak, & Dorst,

2004). Consequently, the earthquakes are assumed to be entirely induced and this establishes an upper bound on the maximum magnitude possible of an earthquake.

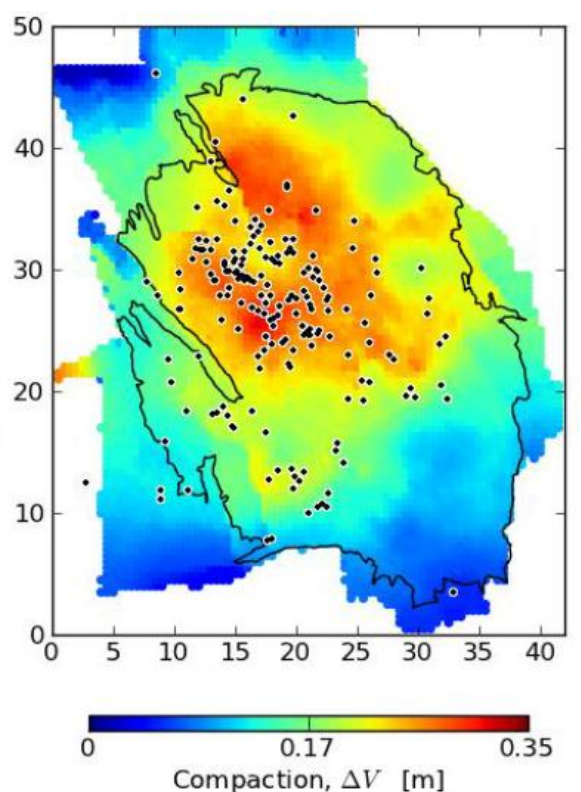


Figure 4: (NAM, November 2013): shows the normalised compaction over the Groningen field. Earthquake epicentres are dotted on the map in black and mostly correspond to the areas where the highest level of compaction has occurred.

3.1.4. Faulting

Abrupt fault movement is the mechanism that triggers earthquakes in the Groningen field. Reservoir compaction does not necessarily result in seismicity; energy can be dissipated via deformation and fault slip can occur over a more gradual period. A restriction in the movement of a fault in a compacting rock can increase the shear stress across a fault plane. It was noted by Brace and Byerlee that Earthquakes are the result of a 'stick slip' frictional instability of faults, whereby seismic strain accumulates by a restriction in fault movement, until a sudden slip releases this energy (Brace & Byerlee).

The Groningen reservoir is dissected by natural faults that predominantly trend in the northwest-southeast direction (Stauble & Milius, 1970). As the stress field changes across the reservoir, the existing faults act as areas of weakness in the field, where seismicity is expected to occur (Dost & Haak, 2007). Computer simulations have highlighted that pressure change from gas production can cause stress change across existing faults leading to their reactivation and the release of seismic energy (NAM, November 2013).

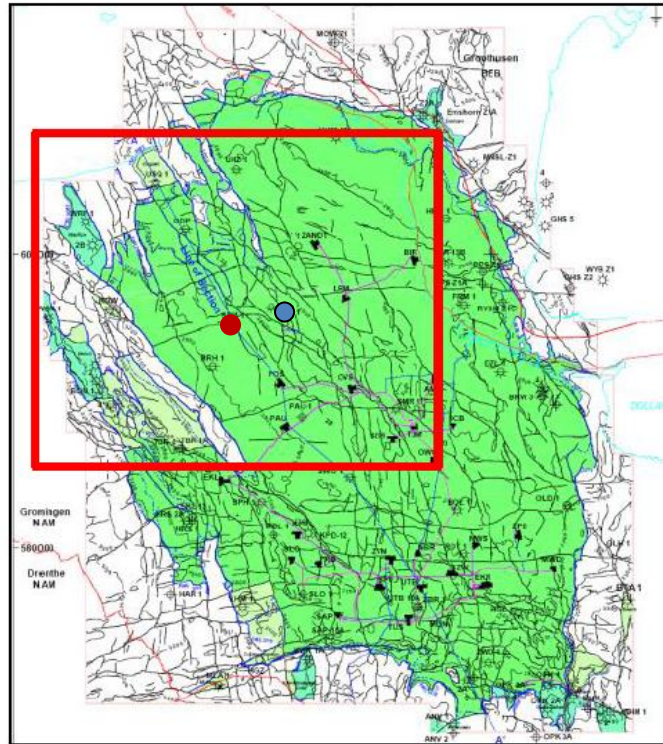


Figure 5: shows the location of the two monitoring wells and the fault network through the Groningen field. The Stedum-1 and Zeerijp-1 well locations are indicated by the red and blue circles respectively (NAM, November 2013).

3.1.5. Moment Magnitude

The seismic moment gives a measure of the total size of an earthquake. This is calculated as the product of the average fault slip, the area of slip and the shear modulus of the medium. The relationship between the seismic moment and the moment magnitude of an earthquake can then be defined as:

$$\log_{10}M_0 = c + dM$$

Where M_0 is the seismic moment, M is the moment magnitude. The constants c and d for shallow earthquakes are 9.1 and 1.5 (C.Hanks & Kanamori, 1979). For this report, the 'magnitude' will refer to moment magnitude.

3.1.6. Maximum magnitude

The seismic moment can be calculated from the effect of compaction from the product of the bulk reservoir volume decrease and the shear modulus (McGarr, 1976). The expected bulk reservoir volume decrease is $3.3 \times 10^8 \text{ m}^3$ with a shear modulus of 10 GPa giving a total maximum seismic moment of 7.7×10^{18} (NAM, November 2013). This establishes a hypothetical upper bound on the maximum earthquake size possible at a magnitude of 6.5, corresponding to the unlikely scenario that the entire seismic moment is released in a single event (NAM, November 2013). NAM estimates that the proportion of reservoir compaction that is accommodated by earthquake inducing fault slips to be roughly 0.1%; this establishes a maximum possible magnitude of 4.5 with a 95% upper bound of 5.5 (NAM, November 2013).

However, its maximum value is uncertain due to lack of data of higher magnitude events as expected from the Gutenberg-Richter frequency magnitude relationship (Gutenberg & Richter, 1949) and the uncertainty over the maximum size of the fault slip area.

3.2. Ray-tracing

The seismic events in the Groningen field were located from the inversion of the P and S arrival times. The accuracy in the event location depended on the accuracy of modelling the ray-paths the rays propagated through the subsurface between the source and the monitoring array.

3.2.1. Ray-tracing methods

Seismic ray-tracing is the process of identifying the ray-paths through refracting and reflecting surfaces due to velocity variations. The path is calculated assuming the wave has an infinitely high frequency. For a homogeneous subsurface, the ray path is simply a straight line connecting the source point to the receiver; however, more complex velocity models require more complex and hence computationally expensive ray-tracing solutions.

There are numerous different seismic ray-tracing methods for velocity models of varying complexity. In Point-to-curve ray-tracing methods described by Hanyga (Hanyga, 1991), the receiver is allowed to vary along the curve of the ray whilst the algorithm defines the receiver and its ray-path. Finite difference methods, such as the method developed by Vidale (Vidale J. , 1988), functions by extrapolating travel times away from the source by dividing a 2D surface into cells, with travel times calculated at each cell corner. This method was further developed to function for three dimensional velocity models (Vidale J. , 1990).

Wave-front construction methods developed by Vinje (Vinje, Iversen, & Gjoystdal, 1993) provide a more accurate 2D ray tracing procedure compared to finite difference modelling. These have the advantage that they are able to estimate amplitudes and later arrivals, in addition to the first arrivals. However, the drawback of this method is that it requires significantly more computational time (Mendecki A. , 1997). A previous trial of this method had shown that it was too time consuming to be used functionally in this project.

Tian ray-tracing (sec 3.2.2) developed by Tian and Chen (Tian & Chen, 2005) was determined to provide the most suitable compromise between precision and computational time in the 1D variant velocity model used. This method had the advantage that it provided both a rapid and stable convergence, which could determine ray-paths in all source-receiver orientations.

A horizontally layered velocity model using constant velocity layers was used in this project (full details can be found in the appendix). Whilst determining results to a higher level of precision, ray-tracing through a three dimensionally variant velocity model is computationally expensive and has consequently been avoided in this project. A one-dimensional model was not ideal given that the heights of the formation tops varied across the field, however, it was deemed appropriate due to the time constraints.

3.2.2. Tian ray-tracing overview

The method determines the ray paths of direct and refracted waves in a one dimensional velocity structure by searching through grid points in a specified volume divided into L layers (Tian & Chen, 2005). The ray-path is determined by the ray parameter p; the algorithm in the software searches for the ray parameter that solves the epicentral equation.

$$\Delta = p \sum_{k=1}^L \frac{h_k v_k}{\sqrt{1-p^2 v_k^2}} - \Delta_0 \quad (1)$$

Where v_k is the propagation velocity, h_k is the thickness of the K^{th} layer traversed by the ray, Δ is the epicentral distance. The ray parameter for the ray-path gives the refraction angle for the K^{th} layer. The travel time is calculated as the shortest possible direct wave to travel through the interface; this process is repeated for S-waves.

3.3. Source vector determination

Amplitudes are recorded on the x, y and z components of the geophone. The compressional and shear wave energy was differentiated in the software InSite using the Montalbetti and Kanasewich algorithm (Montalbetti & Kanasewich, 1970) using a time domain polarisation filter. In the algorithm, the covariance matrix constructed from the x, y and z instrument axes is transformed into its three eigenvalues and eigenvectors. The direction of P-wave polarisation is determined from the eigenvector that corresponds to the largest eigenvalue. This provides the source vector; the two remaining eigenvectors correspond to the orthogonal horizontal S_H and vertical S_V transverse wave polarisations.

The source vector helps constrain the location of the seismic event. Whilst the P and S arrival times on a receiver identify the propagation distance, which can be thought of as a sphere around the event, the source vector determines the location on this sphere. Consequently, the estimation of event locations from single receivers are highly dependent on the accuracy of the source vector. Furthermore, when the source-receiver offset is large compared to the length of a receiver array, the array will in effect act as a single receiver station as move-out discrimination is poor.

For events observed by two receiver arrays, the source vector determines which of the intersection points correspond to the location of the event. Figure 6 helps to highlight this: the P and S arrival times observed from receiver arrays A and B provide a circle encompassing the radius of distances of origin locations; these circles intersect at two points giving two possible locations for the events. The source azimuth, shown in red, recorded at receivers A and B identifies which of these intersection points the event could have originated from

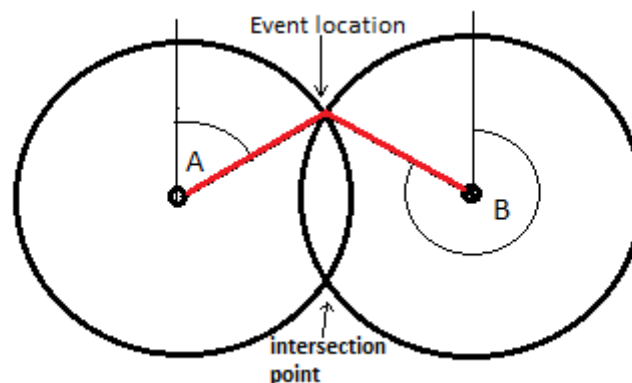


Figure 6 shows a 2D representation of the identification of an event location observed from two receiver arrays using the source azimuth.

3.4. Location methods

Both the grid search and the relative location methods were trialled to locate the seismic events in this project. The relative location method was tested to locate clusters of spatially close events, however, no conclusive results were produced using this method as detailed in 8.3. The grid search method was used to locate all the event location results published in this report.

The Geiger method of event location was not used to locate events in this project. However, the Geiger method is the archetype for other location methods, hence an understanding of this method is required as both the grid search and relative location methods build on the original method developed by Geiger.

3.4.1. Geiger method of event location

Geiger's method of event location (Geiger, 1912) is an iterative approach to solving location times and hypocenters and is one of the first and most widely used methods in earthquake seismology. The method involves initially estimating the event time and three dimensional position coordinates; these parameters are then updated iteratively based on the arrival time residuals.

Given the arrival time measured at n receivers t_j an estimate of the spatial co-ordinates defining the event hypocenter (X, Y, Z) and the event time of the earthquake is made. The residual at the j^{th} receiver (r_j) is calculated based on the observed time at the station t_j , the estimated event time t_0 , and the theoretical travel time from the hypocenter to the receiver coordinates $T(X_0, Y_0, Z_0)$ based on the velocity model.

$$r_j = t_j - t_0 - T(X_0, Y_0, Z_0) \quad (2)$$

The Geiger method aims to minimise the sum of the squared time residuals by adjusting the trial location and timing. The relationship between the arrival times and the event timing and hypocenter is non-linear. To linearise the problem, the source co-ordinates are perturbed by a small value $X_0 + \Delta X, Y_0 + \Delta Y, Z_0 + \Delta Z$ and a first order Taylor expansion is applied to the travel times T giving an equation for the arrival time to the j^{th} receiver of:

$$t_j = t_0 + \delta t_0 + T(x_0, y, z_0) + \frac{\delta T}{\delta x_0} \delta x_0 + \frac{\delta T}{\delta y_0} \delta y_0 + \frac{\delta T}{\delta z_0} \delta z_0 \quad (3)$$

The residual is determined by the change in event position and time combining equations 2 and 3

$$r_j = \frac{\delta T}{\delta x_0} \delta x_0 + \frac{\delta T}{\delta y_0} \delta y_0 + \frac{\delta T}{\delta z_0} \delta z_0 + \delta t_0 \quad (4)$$

A set of linear equations is made for all the receivers in the array. The solutions to the set of linear equations gives the new change in the event position and timing such that.

$$x = x_0 + \Delta x, y = y_0 + \Delta y, z = z_0 + \Delta z, T = T + \Delta T \quad (5)$$

The iteration process is repeated until a set convergence criterion is met. A non-zero time residual will remain after successive iterations due to both the inaccuracy of the velocity model and uncertainty picking exact arrival times in data with poor signal to noise ratio. A low residual error does not necessarily imply an accurate location as the residual determines the precision of the source parameters for an assumed model of the subsurface (Lee & Stewart, 1981).

The method assumes that each receiver is equally reliable. Consequently, large individual errors can disproportionately distort the solution. There is no method to determine whether the minimum of the sum of the squared residuals obtained is a local or global minimum (Lee & Stewart, 1981). Furthermore, the method assumes that the estimated location is close enough to the true location for the travel-time residuals to be calculated as a linear function of the spatial correction made to the event location (Havskov, 2002). Consequently, the final location is dependent on the initial location estimate input into the calculation; as the iteration is linear, the solution may find a local minima instead of the global minimum.

3.4.2. Collapsing grid search method

The collapsing grid search method builds on the Geiger method of event location and was used as an improvement to the Geiger method due to its more rapid convergence time.

The ray-path is calculated as a vector in terms of distance, azimuth and dip. Instead of iterating linearly towards a minimum residual solution, the grid search algorithm searches over a volume for a point that minimizes the misfit between the picked travel times and the theoretical travel times produced by the ray-tracing algorithm using the velocity model. This is performed for every receiver for a source location. When a source position is found that minimizes the sum of the

square residuals, a smaller densely sampled grid volume is defined around this point. It is assumed that each minimum found is the closest grid point to the global minima (Applied seismology Consultants, 2014).

InSite uses a collapsing grid search algorithm to calculate the event locations based on this method.

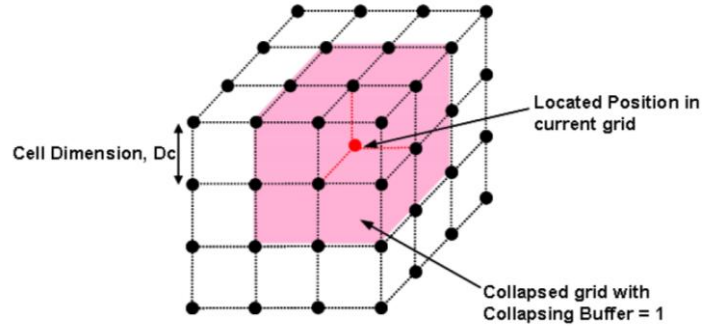


Figure 7: shows the functionality of the collapsing grid search method used in InSite. The volume is discretised into grid point positions and the residual is calculated at each point. This grid is then collapsed by a specified value to refine the search (Applied seismology Consultants, 2014).

3.4.3. Errors

The remaining residual gives a measure of the error of the location produced. A residual is determined for each receiver arrival time as given by equation (2). The root mean square error (E_{RMS}) in the source position is calculated from the arrival time residual using equation:

$$E_{RMS} = 0.5 \left(\sqrt{\frac{\sum_{j=1}^{j=N^P} r_j^P}{N^P} V^P} + \sqrt{\frac{\sum_{j=1}^{j=N^S} r_j^S}{N^S} V^S} \right) \quad (6)$$

Where N^P and N^S are the respective numbers of P and S arrivals, r_j^P and r_j^S are the respective p and s wave residuals, and V^P and V^S are the p and s wave velocities.

3.4.4. Relative location methods

The master event location method (Waldhauser & Ellsworth, 2000) locates an event relative to a reference point that is considered to have an accurate location. This method assumes the locations of the event and reference event are similar enough to assume that the ray paths of both events traverse the same path through the subsurface (Gibowicz & Kijko, 1994). Consequently, the travel times are dependent on the velocity between the master and located event. If the master event location is assumed to be accurate, this removes the travel time residuals arising from the uncertainty in the velocity model across the whole source-receiver volume, by producing a location in reference to the master event. It is generally accepted that the hypocentral distance between the source and master event should be less than 10% of the total source receiver distance for this method to be used accurately (Mendecki, Aswegen, & Mountfort, 1999).

Under the Geiger or grid search methods, the arrival time at a receiver can be shown to be:

$$t_j = t_0 + T(X_0, Y_0, Z_0, M_j) + \Delta T(X_0, Y_0, Z_0, M_j) + \epsilon_j \quad (7)$$

where $T(X_0, Y_0, Z_0, M_j)$ is the calculated travel time from the source hypocenter to the j th station calculated using an average velocity model and $\Delta T(X_0, Y_0, Z_0, M_j)$ is an unknown anomaly resulting from the difference between the travel time calculated using an average velocity model and that of the true velocity of the Earth; ϵ is an unknown measurement error in the arrival time following a Gaussian distribution (Gibowicz & Kijko, 1994).

Similarly, the arrival time recorded for a reference event R is equal to:

$$t_{Rj} = t_{R0} + T(X_{R0}, Y_{R0}, Z_{R0}, M_{Rj}) + \Delta T(X_{R0}, Y_{R0}, Z_{R0}, M_{Rj}) + \epsilon_{Rj} \quad (8)$$

Applying a first order Taylor expansion of 7 around the master event hypocenter:

$$t_j = t_{R0} + \delta t_0 + T(X_{R0}, Y_{R0}, Z_{R0}, M_j) + \frac{\delta T_j}{\delta x_0} \delta x_0 + \frac{\delta T_j}{\delta y_0} \delta y_0 + \frac{\delta T_j}{\delta z_0} \delta z_0 + \Delta T(X_0, Y_0, Z_0, M_{Rj}) + \epsilon_{Rj} \quad (9)$$

Where δt_0 , δx_0 , δy_0 , and δz_0 are the corrections to the event origin time and hypocenter and $\delta T_j = T(X_{R0}, Y_{R0}, Z_{R0}, M_j)$. Under the assumption that the ray paths between the event and the master event are the same, the arrival time anomalies $\Delta T(X_0, Y_0, Z_0, M_j)$ and $\Delta T(X_{R0}, Y_{R0}, Z_{R0}, M_{Rj})$ are also approximated to be the same. Subtracting equation (8) from (9) gives the linear equation:

$$t_j - t_{Rj} = \frac{\delta T}{\delta x_0} \delta x_0 + \frac{\delta T}{\delta y_0} \delta y_0 + \frac{\delta T}{\delta z_0} \delta z_0 + \delta t_0 \quad (10)$$

4. Data

4.1. Data Acquisition

4.1.1. Monitoring arrays

Two reservoir level borehole seismic monitoring geophone arrays were installed in the Stedum-1 and Zeerijp-1 wells using a string of geophones separated at intervals of 30m. Ten geophones were installed in the Stedum well at depths of 2751-3017.4m (depths relative to sea level); with 1 positioned in the Anhydrite, 8 positioned in the Rotliegend reservoir and one positioned in the Carboniferous below. Seven geophones were positioned in the Zeerijp well at depths of between 2781.2-2960.8m with 2 geophone covering the Anhydrite, 5 in the Rotliegend. The lateral distance between the boreholes was 2.9Km.

4.1.2. Well Location

The wells are located in the northwest of the field around the region where the greatest seismicity is observed. The location of these wells in reference to the field can be seen on image Figure 5.

Coordinate	ZRP	SDM
Northing	596471.1	595147.2
Easting	245010.1	242423.2

Table 2: shows the average of the easting and northing coordinates of the geophone arrays in the Stedum and Zeerijp wells.

4.1.3. Sensor

The arrays consisted of Slimwave three-component geophones produced by Sercel measuring orthogonal x,y and z components in a left handed co-ordinate system. Full details can be found in the tool specifications (Seismic tools specifications, 2014). Checkshots were used to determine the orientation of the components. These were undertaken on the 27/11/13 following the placement of the geophones and repeated after the replacement of the geophone arrays on the 25th Mach. The gain was set at 52V/m/s and data was sampled every 0.5ms. Further details on the orientation and sensor can be found in A1.2.

4.1.4. Equipment failures

The data recording was affected by repeated geophone failures. The Slimwave sensors had proved successful in a previous data acquisition study by Shell in the Bergermeer field at a temperature 30C lower than in Groningen. The sensors are quoted to have an operational temperature of up to 135C and a peak temperature of 150C (Seismic tools specifications, 2014), compared to the Groningen reservoir temperature of 110C. However, in correspondence with Sercel, it was highlighted that the tools may not be suitable for continuous deployment in the field. Their laboratory tests on the equipment are ongoing.

4.1.5. Data recording periods

The dataset featured in this report was recorded between 12/10/13 to the 10/05/14. The data for this period is examined in this study, whilst the recording and processing of data by Magnitude is however a continuous process.

Due to equipment failures both wells were not recording continuously through this period. The Stedum well array was operational from 12/10/13 until 23/12/13 and was repaired and

operational from 19/03/13. The Zeerijp well array was operational from 21/11/13 until 03/02/14; and recorded again from 22/02/14. This project focused on events recorded when both wells were operational. This splits the data into two phases between 21/11/2013 – 23/12/2013 and 19/03/14-10/05/14.

On the 15/04/14, geophones 7-10 on the Stedum well failed. No data is available for these geophones from this period onwards.

4.1.6. Data format

The processed data were in SEG-2 format. The seismograms consist of data recorded over a period of ten seconds over a time window around the event.

4.2. Data pre-processing

4.2.1. Data selection

Due to the time constraint of the project and the need to examine the events in detail, not all the events processed by magnitude were re-processed in this study. The analysis will focus on the higher magnitude results, as these tend to produce the greatest signal to noise ratio recorded by both wells. These events were also identified as the greatest interest to NAM as they tended to be located at unexpected depths (see section 5).

Only events that were recorded at a time when both observation well arrays were functioning were processed in this study. Events observed only by one operational well array (due to the failure of the other array) were not processed in this study due to the difficulty in locating events from single well arrays and the lack of confidence in the accuracy in the event. Single well arrays can determine event locations accurately at close source receiver spacings, as is standard in hydraulic fracturing monitoring. However, for large offset events, as the geophone interval spacing is small compared to the source- receiver spacing, the move-out discrimination is poor and the array in effect acts as a point receiver.

Consequently, for these events, the location accuracy is highly dependent on the accuracy of the source vector. The source vector gave a 180 degree uncertainty in the location of the event at far offsets, making it difficult to determine the location of the event without the presence of a second well. At close events, this proved not to be the case as the ray vectors of the array could converge on the source point, eliminating this uncertainty. Furthermore, vertical heterogeneity in the subsurface and azimuthal anisotropy can give unreliable source vector directions. It was concluded in a study by Grechka (Grechka & Yaskovich, 2013) that using multiple observation wells is required for the accurate location of microseismic events with large source vector uncertainties. Consequently, only events recorded at both monitoring wells were processed in this study.

4.2.2. Attenuation

The attenuation Q value was set at both 120 for both P and S waves.

4.2.3. Bandpass filter

A bandpass filter of between 5Hz-70Hz was generally used to process the waveforms prior to analysis. This was used to remove the high frequency noise that appeared in the signal. The frequency of an event is related to its magnitude; higher magnitude events will emit lower frequency energy. The Fourier spectrum of an event was analysed and if a clear peak could be observed over a defined bandwidth, the filter was often narrowed around this bandwidth to improve the signal to noise ratio of the specific event.

5. Analysis of Magnitude’s results

The data were recorded and processed by the microseismic service company Magnitude. A total of 267 events were located through the entire period of recording; these had a range in magnitude from -2.8 to 1.9. In the dataset, a peak in the frequency of magnitude was observed at -0.75 (low magnitude events are expected to be more common in accordance with the Gutenberg-Richter law (Gutenberg & Richter, 1949) however are less likely to be detected due to attenuation with distance). The data followed a Gutenberg-Richter law from a magnitude of 0 onwards with a b value of 0.97 (see appendix A1.3.5).

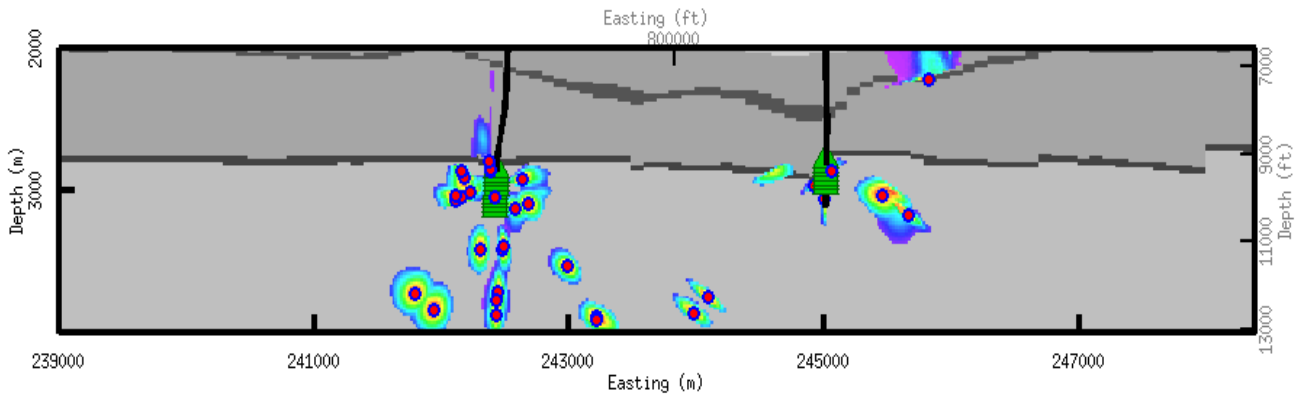


Figure 8: shows the locations of a subset events processed by Magnitude showing their estimated event hypocenters and error surface. Image courtesy of Magnitude.

The majority of events that were located with epicentres close to one of the well monitoring arrays had depths that were located in and around the reservoir itself as predicted. However, in most of the events where epicentres were located away from the monitoring arrays, the events were located at depths far deeper than reservoir level.

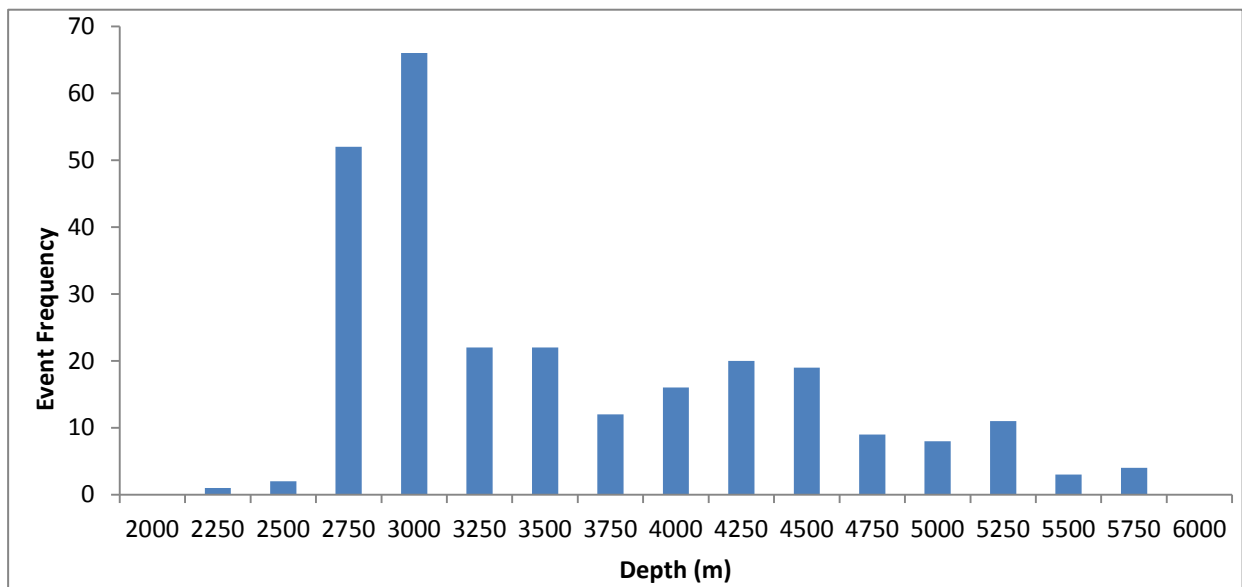


Figure 9: Histogram of all events depths determined by Magnitude.

Figure 9 shows Magnitudes estimated event depths provided by the service company. There is a clear peak in the event frequency occurring at reservoir level. These events are largely located close to the array itself and tend to be low in magnitude as in accordance to the Gutenberg-

Richter relationship, the event frequency decreases exponentially with increasing magnitude. In contrast, large offset events are high in magnitude due to the attenuation of low energy events with distance to amplitudes below the resolution of the receivers. Figure 24 in the appendix A1.3.4 shows the events depths determined for events over a magnitude of 0: these events were determined to be much lower than reservoir level, with an average depth of 4.6Km.

Figure 10 highlights the trend of event depths appearing to become deeper as the source- receiver offset increases. This indicates that the far offset event depths estimated to occur deep in the Carboniferous are likely due to an error produced in ray-tracing over long distances. On the 4th of August, Magnitude revised these estimates by basing the location on arrival times of S to P conversions in addition to the P and S arrival times. The events also appear to follow the same trend of increasing apparent depth with source-receiver offset, although at far offsets the events depth estimates level off around the 3500m mark 500m below the base of the reservoir. The change in apparent event depth with source-receiver distance however indicates that these results are also likely to be inaccurate. As discussed in 3.1.2 events may be possible in the Carboniferous as reservoir compaction exerts stress on this layer, although they are unlikely to occur at depths far into this layer. Further detailed analysis of Magnitudes results and event location procedure can be found in A1.3.

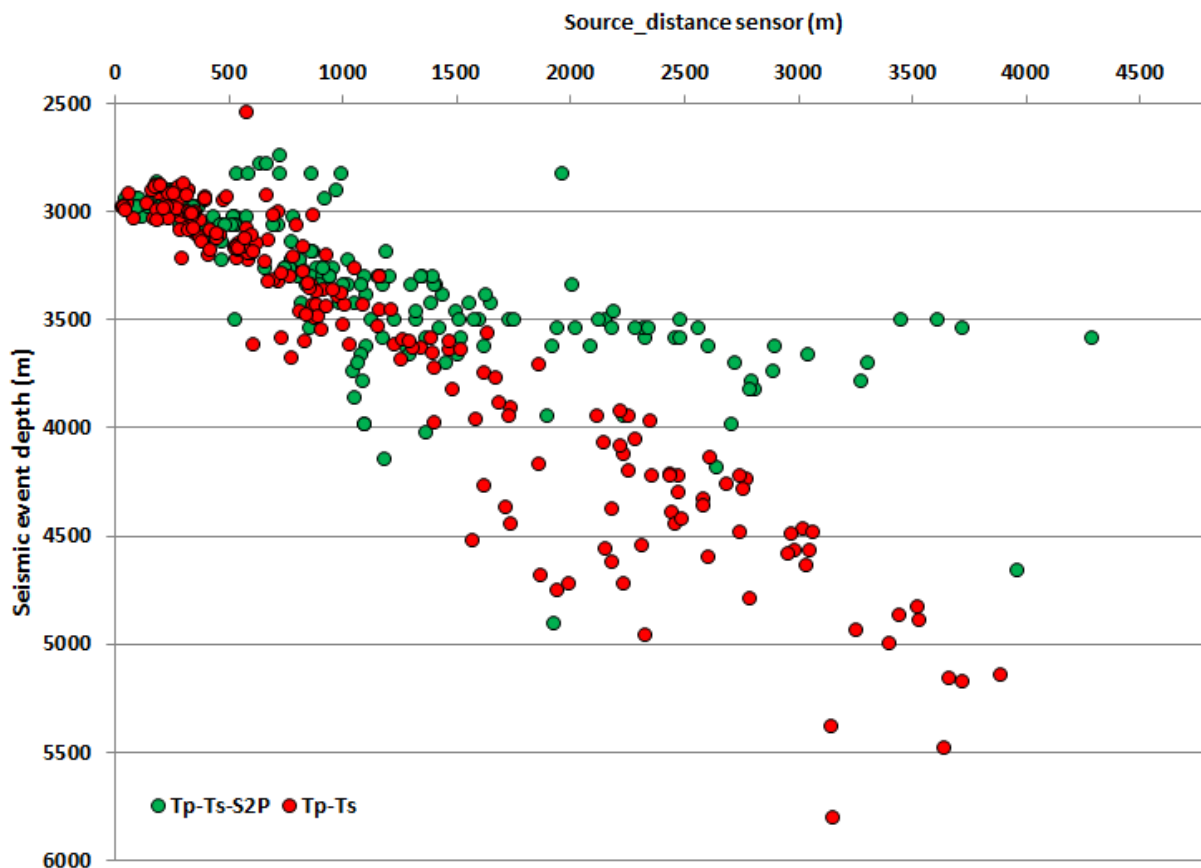


Figure 10 Image courtesy of Magnitude: shows the estimation of the event depth plotted against the source receiver distance observed. The red points show their previous depth estimates based on the arrival time inversion using P and S wave arrival times; the green dots show their revised estimates as of 04/08/14 based on using arrival time picks of P, S and S to P conversions.

6. Waveform interpretation Methods

6.1. Overview

Accurate locations of the seismic events required the P and S wave arrival times to be determined accurately from the earthquake seismograms recorded. The waveforms analysed in this project were largely very complex making the identification of the P and S arrival times difficult to determine. The seismograms largely did not have the clean P and S arrivals seen in standard microseismic data; and explains why Magnitude, an experienced microseismic service company, had produced anomalous event locations.

The identification of the arrivals of the direct P and S waves became an interpretive process, and rarely could be identified directly from the first break in compressional and shear wave energy observed in the seismograms. This ruled out the possibility of using a simple auto-picker that picked arrivals on first break energy. Detailed interpretations of the waveforms were required to manually identify the direct arrival times in the seismograms. The seismograms with their arrival time picks for events located in this study are all shown in the appendix.

Finite difference modelling (6.2) was used to characterize each of the P and S arrivals observed in the seismograms and gain an understanding of the wave propagation in the subsurface. The P and S arrivals were picked on the seismograms based on this analysis. The source azimuth was determined for both wells, which gave an estimate of the event location at the ray-path intersection point (6.4). This also was used to distinguish direct arrivals from headwaves and later reflected waves. Forward modelling used in InSite could be used to pick arrivals on wells with poor signal to noise ratio, based on the results on the other well where arrivals could be identified more clearly (6.3.1). Analysis of waveform polarisation was also used to identify direct waves from converted or reflected arrivals 6.4.1. This methodology is explained in the subsequent section.

6.2. Finite difference modelling

Finite difference modelling was used to aid the interpretation of the traces observed. The algorithm simulates the propagation of the waveform through a 2D surface by solving the wave equation through finite differences. See reference for further details on functionality (Igel, Mora, & Riollet, 1995).

Events were modelled at varying depths in the subsurface to view the propagation of the waves. This forward modelling approach was used to gain an understanding of the seismograms observed, to guide the arrival time picking process.

A grid of length 5000m and of depth 5000m was modelled at points separated in length and depth by 2.5m. Whilst the Tian ray-tracer used in InSite functioned with constant velocity layers, a velocity gradient could be established in the finite difference model to account for these small layer velocity variations.

The model produced a snapshot of the ray propagation every 0.001 seconds. The program models the wave propagation over a 2D area, rather than a 3D spherical volume. Therefore, the waves observed are not the true relative amplitude. However, this method was used for a visual aid to the interpretation instead of for a quantitative trace correlation, and therefore was suitable for the purposes of the project.

The images were used to identify the direct waves, headwaves and mode conversions observed after a seismic event. The event depth was varied to determine its effect on the wave propagation. This was used to aid the interpretation of the real waveforms observed to guide the P and S arrival picking.

The algorithm was supposed to model perfectly absorbing boundaries; in practice, this was found not to be the case and reflections could be observed off the sides of the model. The model was limited in size due to the computational cost of running the finite difference algorithm. The very high impedance contrast of the Rotliegend- Anhydrite boundary produced strong headwaves, reflections and mode conversions in the model. This confirmed the expectation that this interface was responsible for the complexity of the waveforms observed.

Although the geophone arrays cover only a small proportion of the depths around the Rotliegend, a large cross section of the subsurface was observed to provide more information on the wave propagation. In the interpretation of the traces observed in the dataset, the epicentre location of the event given by Magnitude was used to estimate the source-receiver offset of the event at each well. The finite difference model was then examined to judge the expected waveform observed at this offset distance, to guide the picking of the P and S direct arrivals.

Figure 11 shows the results of the finite difference modelling of an event located at a depth 2900m. This image firstly indicates that headwaves are produced off the reservoir-Anhydrite interface. This energy begins to decay at a faster rate than the direct arrivals. Strong P wave reflections can be seen propagating from this interface due to the high impedance contrast. Due to the velocity contrasts at this interface, energy is expected to be reflected back past the critical incidence angle of approximately 40 degrees. Consequently, a very high amplitude reflected arrival follows behind the direct P. This effect was observed in the majority of traces; an example of this can be observed on event 15/12 07:39 in the appendix.

In Figure 12, it appears that high amplitude P wave energy propagates through the reservoir behind the direct arrival. This may be a tunnelling effect of the reservoir as the waves refract inside this layer causing constructive interference. The direct arrival appears to attenuate with propagation distance. However, this trapped wave appears to attenuate at a slower rate. In far offset events observed at the observation well seismograms, this increased the uncertainty in picking the direct arrivals which were a lower amplitude than the subsequent P arrivals. An example of this can be seen in event 06/05/14 03:23. Arrival time forward modelling (see 6.3) was used to guide the picking when subsequent high amplitude arrivals disguised these lower amplitude direct P arrivals.

The strength of the reflections may also be dependent on the source depth below the Anhydrite. A large amount of the reflected energy will be due to critical refraction. Events located close to the Anhydrite would hit the layer at a large incidence angle and be critically refracted back into the reservoir. This can be observed in the wave propagation of an event that was modelled at a depth of 2800m, 30m below the Anhydrite interface (see A1.4.2), where the reflected P wave was at a far higher amplitude than the direct wave.

The finite difference modelling also indicated that the direct s-wave arrival would be very difficult to pick accurately at a larger source-receiver distance. Strong P-S mode conversions were expected to occur off the Anhydrite-Rotliegend interface obscuring the direct s-wave arrival. As the P-S conversions propagated downwards off this interface, it was expected that this downwards propagation would be observed in the move-out down receiver array. This would aid the interpretation of the S-wave arrival, as the P-S conversions and direct waves could be distinguished from each other from their move-out. Event 25/03/14 (see appendix A1.6.1) shows a clear example of this. At the receiver positions in the low Rotliegend and Carboniferous where the P-S conversions arrives after the direct S-wave, the direct s wave was easier to locate.

The direct S arrivals in the upper reservoir and Anhydrite geophones (roughly the first 3-4) were picked aided by the move-out trend on the lower geophones.

It is worth noting that the Carboniferous-reservoir interface does not appear to have a significant effect on the waveform. In initial discussions with Magnitude, it was suggested that reflections and mode conversions off this interface also had a significant effect on the wave. This effect however was not seen in the finite difference model or could not be interpreted in the traces themselves. Due to the velocity gradient in the reservoir, both the velocity difference and impedance contrast between these two layers does not appear to be high enough to cause reflections and mode conversions of significant amplitude.

A finite difference model with a source at a depth of 4600m was run to examine the waveforms predicted from the deep event locations estimated by Magnitude. This can be seen in A1.4.3. The model predicts strong clear direct arrivals from this depth, with a clear P and S separation. Reflections and mode conversions can be seen at further source-receiver offsets; however, these appear to be much weaker in amplitude. Overall simple waveforms that would produce easily identifiable direct arrivals were predicted for events at this depth in the finite difference modelling. This propagation expected did not correspond to any of the seismogram traces observed, therefore it was considered unlikely that earthquakes were occurring at this depth based on the dataset examined.

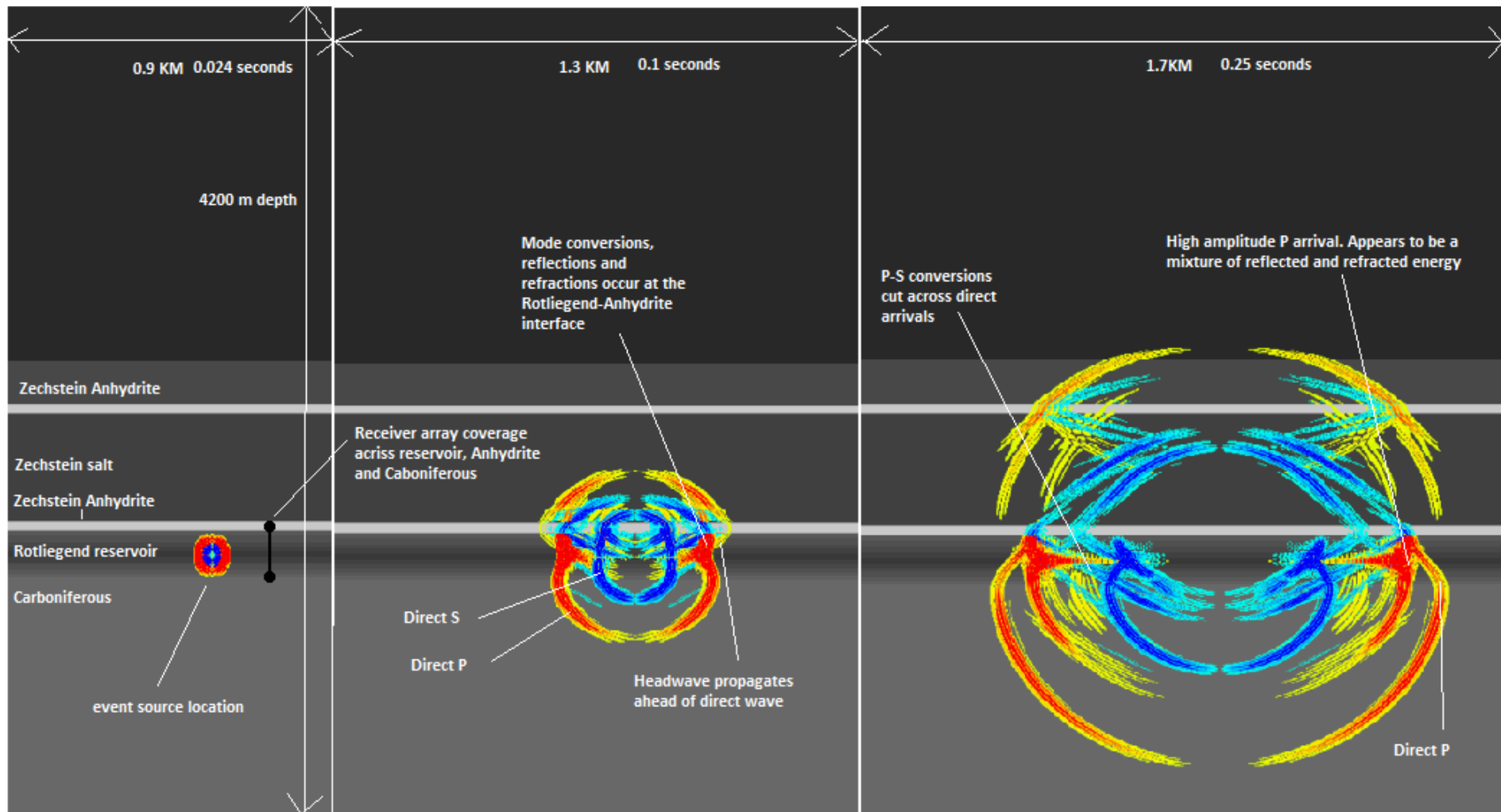


Figure 11 results of finite difference modelling of an event at a depth of 2900m showing the propagation of a wave through the subsurface at source-receiver distances of under 1 Km.

Red indicates P wave energy whilst blue represents shear wave energy. The lighter areas of the subsurface indicate layers of higher velocity. The receiver array is drawn on for visual effect to highlight the vertical extent of coverage in the subsurface.

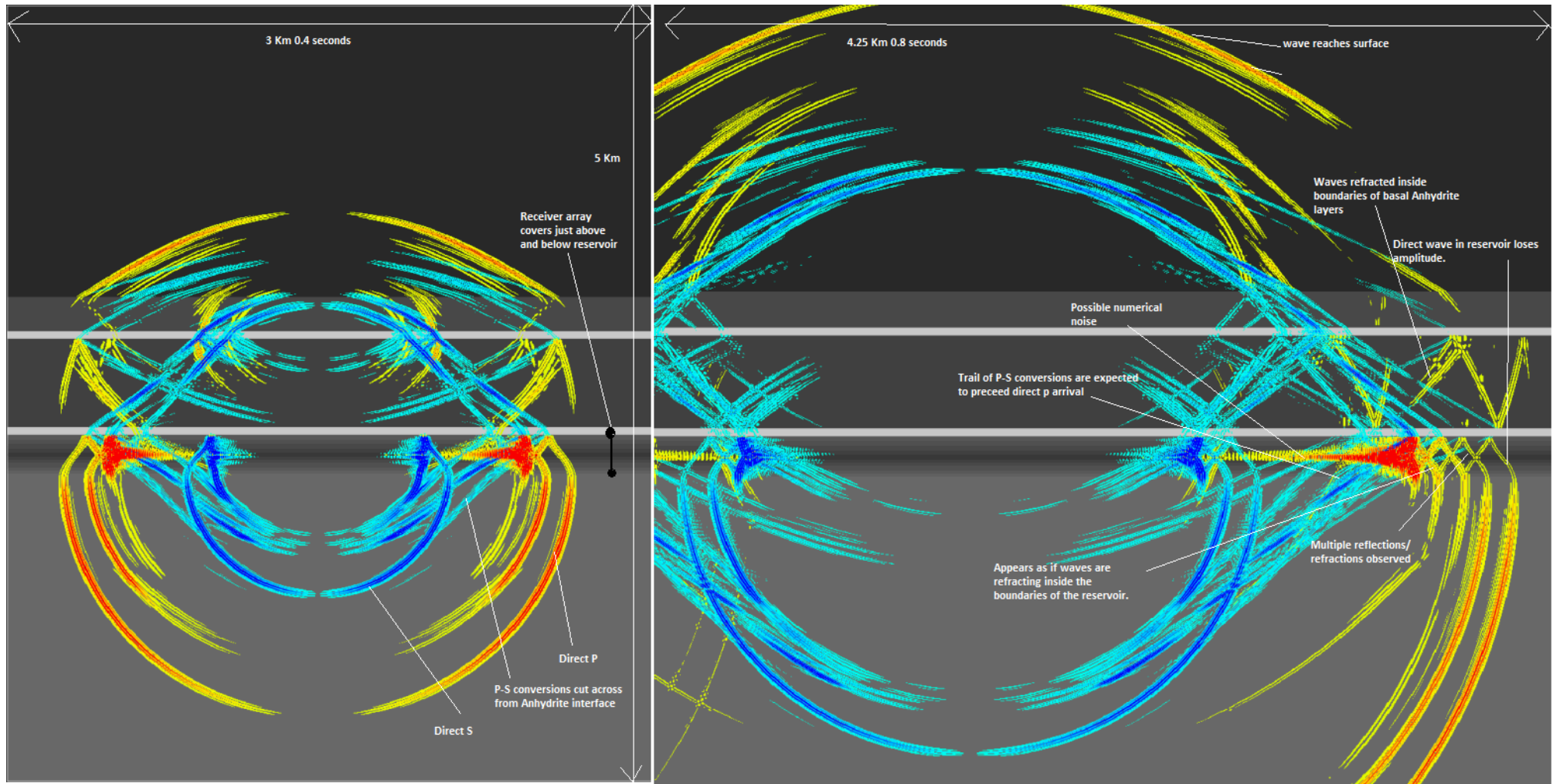


Figure 12 the results of the finite difference modelling of an event at a depth of 2900m showing the propagation of a wave through the subsurface at source receiver spacing's of over 1Km.

6.3. InSite event picking

6.3.1. Arrival time forward modelling

In certain events, the P and S arrival times could be more accurately determined on one well array compared to the other. This often occurred in a case where the source epicentre was located much closer to one particular well. An estimate of the source location was made using the arrival time information of a single well. InSite had the function to forward model the predicted P and S time curves based on a user defined source location in the model. This gave the predicted move-out curve and P and S arrival time separation. The expected P and S separation forward modelled using the event location obtained from one wells, was used to guide the arrival time picking of the event observed from the second well array. This was used to aid the interpretation of the p and s arrival times, helping to differentiate between the direct arrivals and noise.

6.3.2. Layer discrimination

One benefit of the high velocity contrasts observed above and below the reservoir was the ability to distinguish the layer the event was located in, by the waveform move-out and P and S arrival time separation. This helped to establish whether a layer was located inside the Anhydrite, Rotliegend Reservoir, or the Carboniferous based on the velocity model.

A small location difference above and below an interface significantly affected the propagation path due to the refraction angle change from the velocity contrasts. For an event located inside the reservoir, very little move out discrimination was predicted as the geophone array is small compared to the source-receiver distance. For an event located in the carboniferous, as the direct wave enters the lower velocity reservoir from the higher velocity carboniferous, it refracts towards the normal causing the direct waves to arrive at an even earlier time at the base of the geophone array than at the top, increasing the level of move-out observed. Event 22/03 at 15:10:08 shows the seismogram characteristics of an example event located just inside the Carboniferous layer (see A1.5 for analysis of this event using this method). It can be concluded with relative confidence, whether an event is positioned in the Anhydrite, the reservoir or the carboniferous. However, it is also worth noting that the uncertainty bounds in layer are relatively large, as moderate changes in the event depth result in minor changes in the arrival times as the examples above highlight.

6.4. Use of source angle

The software used in InSite split the wave energy into one primary and two orthogonal shear wave modes as discussed in 3.3. The orientation of the P wave motion provided the source vector for the event. The dip angle of this source vector was used to determine the direct P arrival time. The headwaves preceding the direct arrivals had large dip angles indicative of reflections off layer interfaces; they appeared to have a dip angle directed at the Rotliegend-Anhydrite layer interface. At the point in time of the direct arrival, the dip angle changed to an angle roughly 90 degrees to the vertical receiver array suggesting an event occurred at roughly reservoir level.

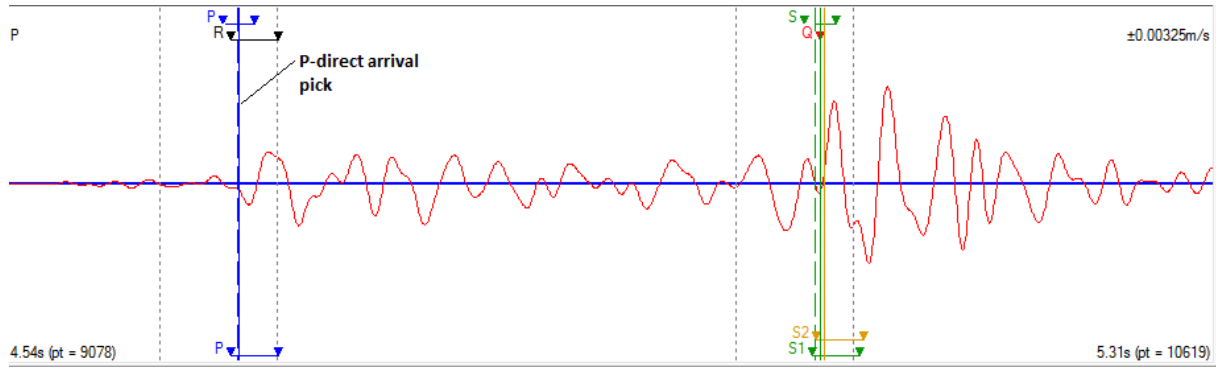


Figure 13 Shows a the direct arrival pick made on the event 22/03/14 15:10:08 made on the P component of the 6th geophone on the Zeerijp well.

Figures 13-16 highlight the use of the source dip angle in the identification of the direct arrival using the event 22/03/13 15:10:08 on the 6th geophone of the Zeerijp well. From this receiver, the source is positioned almost 75 degrees east of north, at a dip angle pointing 5 degrees upwards from the horizontal. The source vector has a linearity of 76%, indicating that a large proportion of the p wave energy is aligned in the direction of this source vector. Figure 13 shows the direct P-wave identified on the seismogram; the figures below show the azimuths and dip of the source vector. The dip of the source vector points almost perpendicular to the vertical.

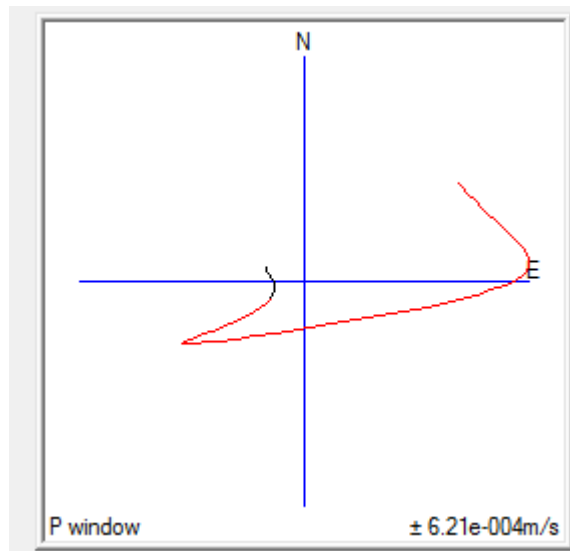


Figure 15 shows the azimuth of the p wave for pick given in Figure 13. The image shows the source angle on the north-east plane

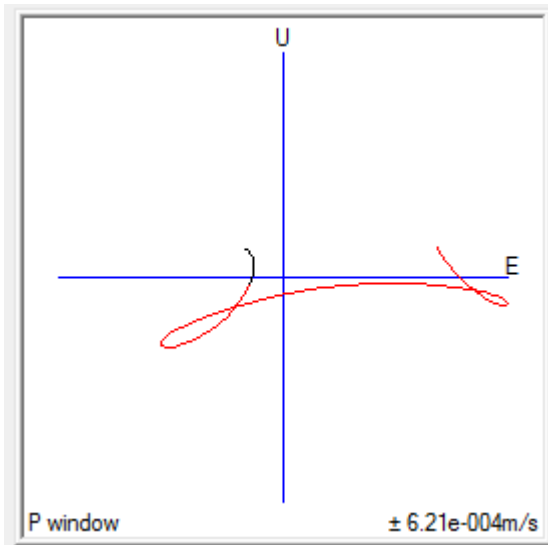


Figure 14 the dip angle for the p wave for the pick made in Figure 13. The image shows the source angle on the up-east plane.

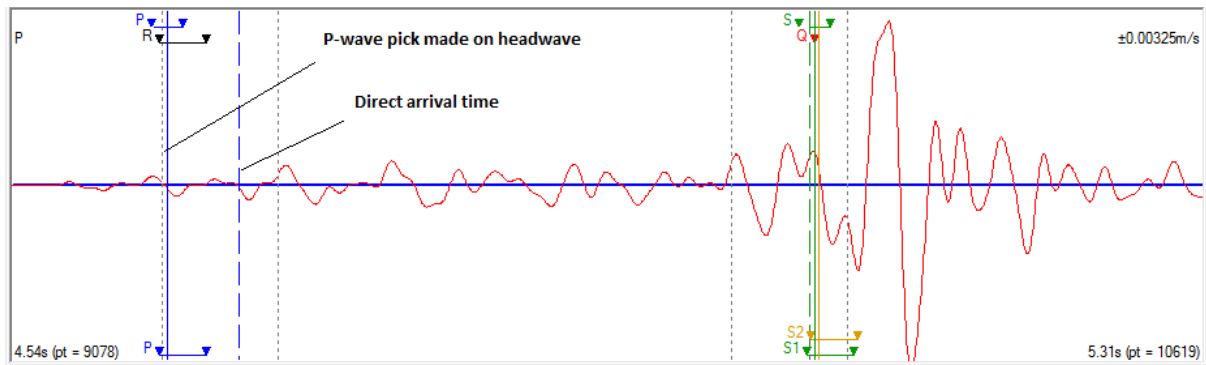


Figure 16 shows a P-Wave pick made on the headwaves on the event 22/03/14 15:10:08 on the 6th geophone of the Zeerijp well.

Conversely if the arrival time pick is made on the headwaves preceding this direct arrival, the source angle changes. As the headwaves are propagating off the Anhydrite layer, the source vector points almost directly upwards at an angle of 76 degrees from a plane parallel to depth of the receiver. This propagation angle helps distinguish the direct wave from the headwaves. The headwaves however also have a relatively high degree of linearity; for the pick made in figure 16 a linearity of 86% was recorded as the rays consistently propagate from the same direction.

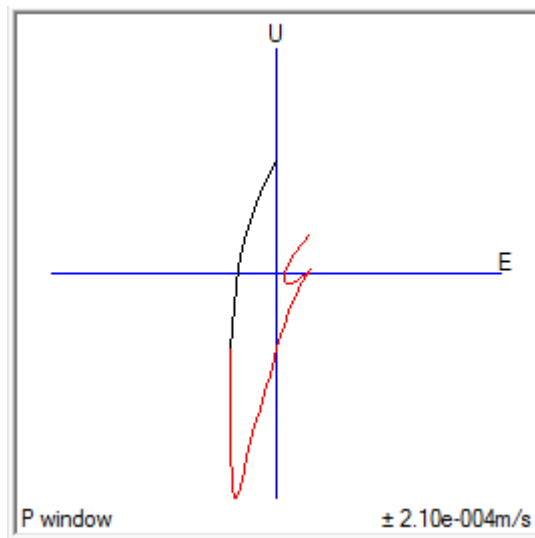


Figure 17 shows the dip of the source vector on the headwaves pick made in Figure 16 pointing towards the vertical. The image shows the source angle on the East-Up plane.

6.4.1. Linearity

The linearity can be used to distinguish direct waves from later arrivals. The linearity gives a quantitative measure of the noise in the signal along the direction of P and S wave motion and is also determined from the Montalbette and Kanasewich algorithm referred to in 3.3.

Arrivals originating from scattered waves, reflections and mode conversions would exhibit inconsistent particle motion. Elliptical motion would be observed on the hodogram images. Figure 18 shows a P pick made on the same event after the direct arrival; Figure 19 demonstrates the P wave particle motion at this point in time. Elliptical wave motion can be observed at this point in time and a linearity of only 28% could be seen along the source to receiver direction line. It was predicted from finite difference modelling that P-S conversions, reflections and interference waves would follow this direct arrival. Further scattering effects would also be

expected from unknown variations in the subsurface velocity. Consequently there is no consistent direction of P wave motion that would indicate the direction from source to receiver.



Figure 18 shows a P-pick made after the direct arrival to highlight the effect on the wave linearity.

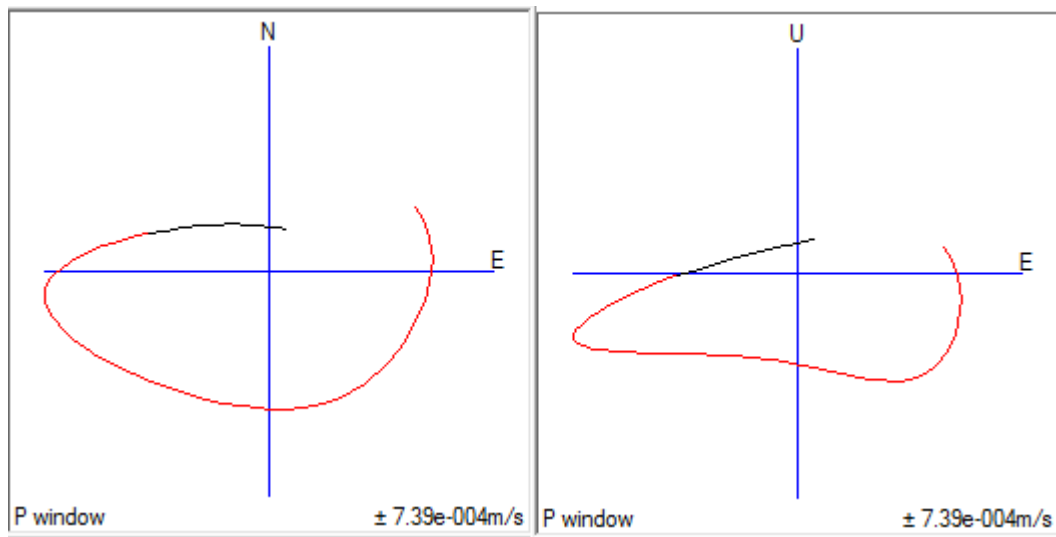


Figure 19 shows the effect on the p wave motion of the particles in terms of north-east plane and the vertical-east plane at the time located in Figure 18.

The source-receiver azimuth observed from both wells was also used to observe the approximate location of the event, as the event should lie in the direction of p-wave motion as determined from the receiver. The intersection point of these two ray azimuths seen from each receiver array should theoretically correspond to the actual event location (within the margin of error in the angular uncertainty). This information was used as part of the iterative picking process to check that the results were consistent.

6.4.2. *Waveform polarisation*

The level of polarisation of the waveform can also provide an additional aid in the identification of direct arrivals in the waveform. A direct P wave should have a high level of polarisation along the source azimuth whilst S waves should have particle motion orthogonal to the P source vector direction. Conversely, mode conversions, reflections and scattered waves should have lower levels of polarisation. Figure 20 shows how the polarisation of the wave was used to distinguish the direct P arrival from the headwaves; Figure 21 shows how it was used to separate the direct S arrival from the P-S conversions preceding the arrival. Clear peaks in the amplitude can be seen

at the point in time of the direct arrivals. A seismogram with a simple waveform was shown to demonstrate this effect clearly.

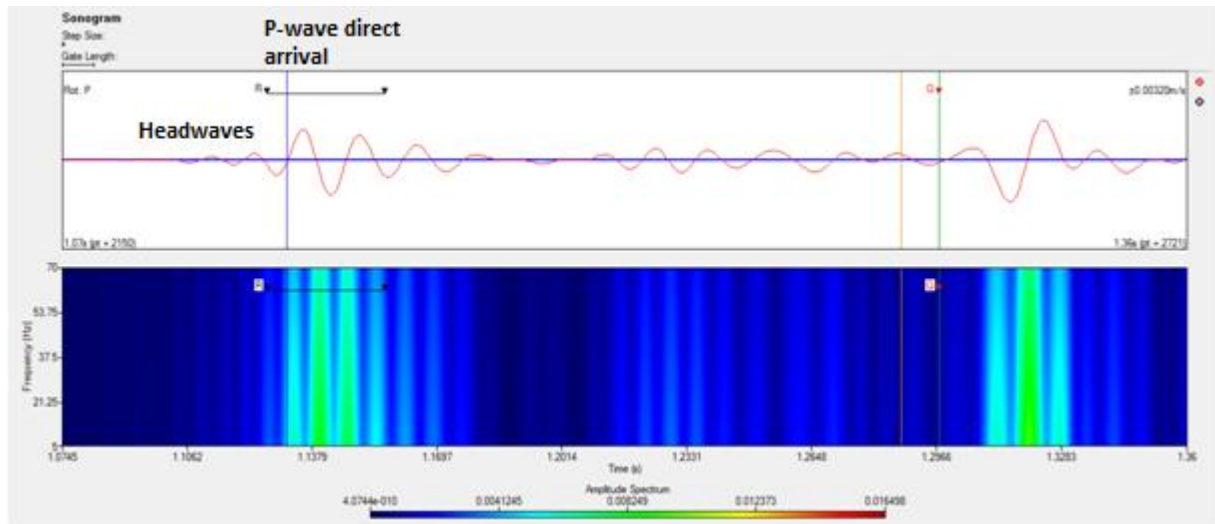


Figure 20 shows how the polarisation of the waveform was used to judge direct P arrival time. Image shows the response from the rotated P component of the 7th geophone of the Zeerijp well on the event 21/03/14 11:28:25.

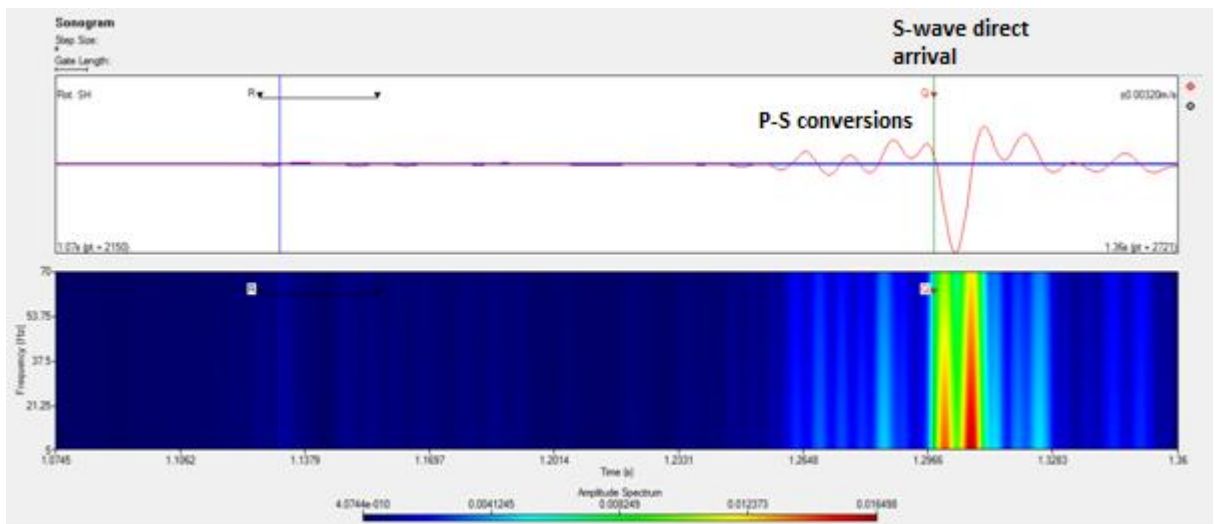


Figure 21 shows how the polarisation of the waveform was used to judge direct S arrival time. Image shows the response from the rotated S_H component of the 7th geophone of the Zeerijp well on the event 21/03/14 11:28:25.

7. Results

In total 25 of the 32 events were located inside the reservoir as Figure 23 highlights; five of these events were located inside the Anhydrite and 2 in the Carboniferous. All the events were located within 100m of the reservoir. The events had a mean depth of 2921m corresponding to the approximate depth of the centre of the reservoir.

The following images show the results produced using the grid search method of event location. A full breakdown of the events and their locations and errors can be seen in A1.1. As the size of the errors in the event location are large, error bars are not shown on these images to avoid hiding spatially close results. The mean residual distance error for the data quoted in the appendix A1.1 table of results was 83m.

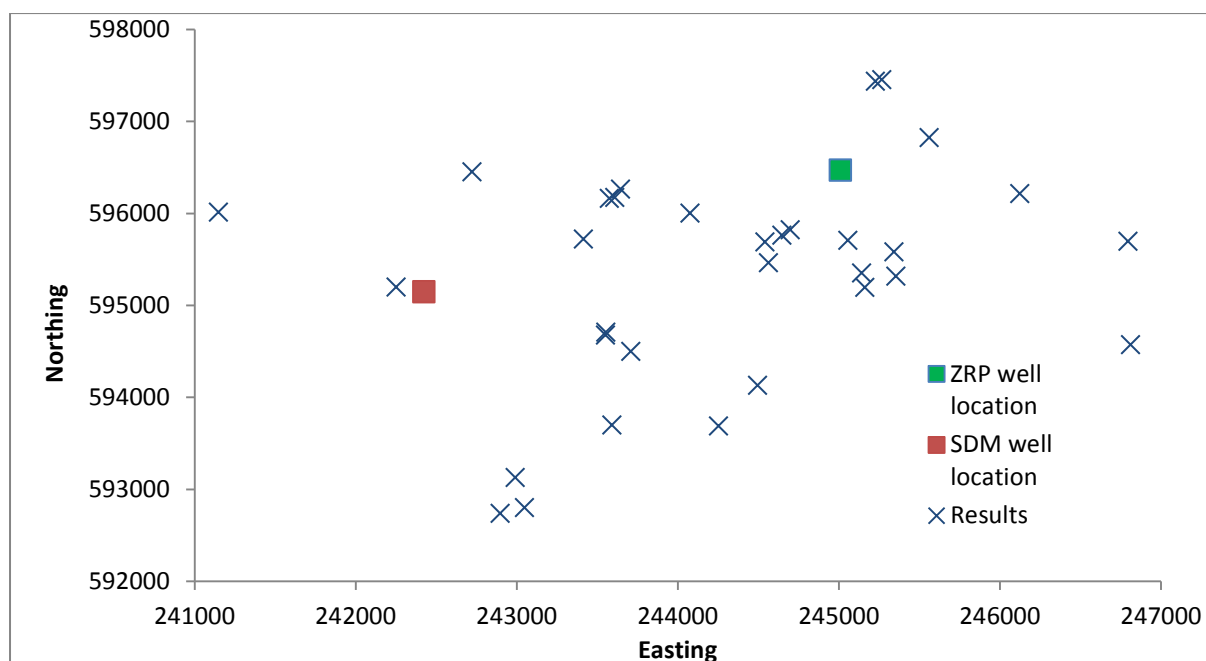


Figure 22 shows the northing and easting components of the event epicentres located in this project.

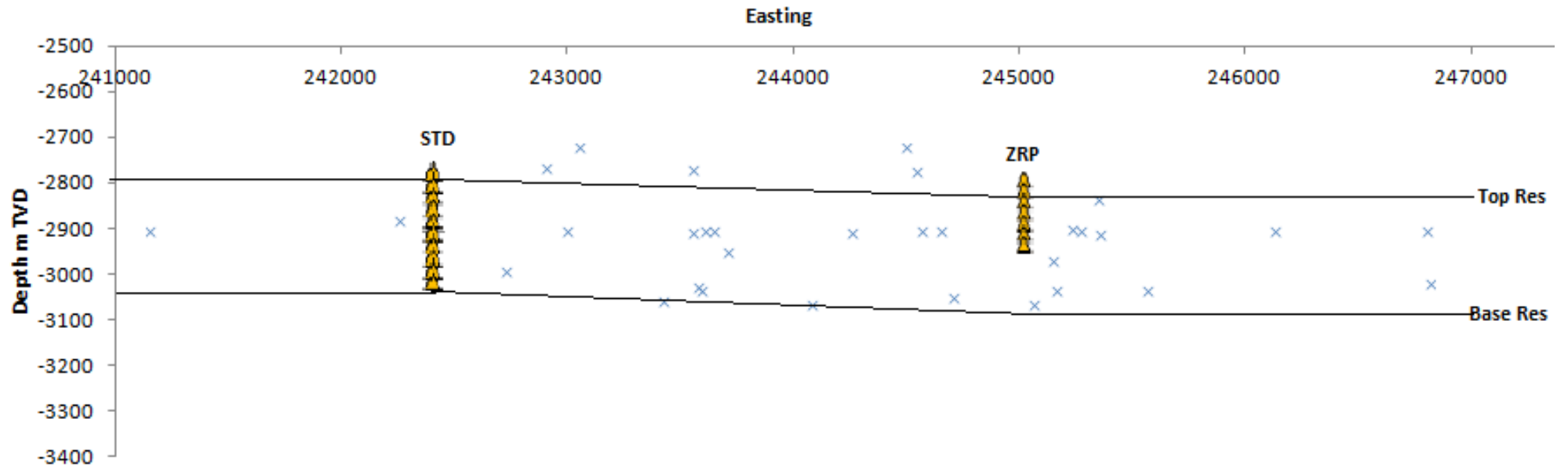


Figure 23 shows the locations of the seismic events in terms of easting and true vertical depth below sea level. The top and base of the reservoir is shown in addition to the location of the Stedum (STD) and Zeerijp well (ZRP).

<i>Magnitudes initial results</i>	<i>Depth (m)</i>
Mean	4252
Upper bound	4921
Lower bound	3583

Table 3 shows the mean depth estimates by Magnitude in the dataset of 32 events used in this project. Upper and low bounds are base on one standard deviation from the mean.

<i>Shell revised estimates</i>	<i>Depth (m)</i>
Mean	2921
Upper bound	3020
Lower bound	2822

Table 4 shows the revised estimates of the event true vertical depths of 32 events showing the upper and lower bounds of the depth based on 1 standard deviation from mean

8. Discussion on results

8.1. Overview

The results of this project appeared to support the hypothesis that the events were occurring in and around the Rotliegend reservoir. The majority of events occurred inside the reservoir; there were several events that occurred both in the lower Zechstein and the upper Carboniferous layer. As these occurred close to the boundary of the reservoir interface, it is impossible to determine whether the event occurred inside the reservoir based on the uncertainty in the knowledge of the layer depths at these locations. All the events processed produced locations at depths close enough to the reservoir to support the expectation that the seismicity was occurring due to reservoir compaction.

A great deal of difficulty was encountered in interpreting the P and S direct wave arrivals in the seismograms. The P wave arrival was often low amplitude and was significantly affected by noise generated by headwaves, reflections and mode conversions.

8.2. Result accuracy

8.2.1. Uncertainty estimates

The events located had uncertainties with a range and standard deviation of 83 ± 33 m which appears to be low given that the rays propagated over distances of several kilometres to the receiver arrays. However, these uncertainties correspond to the event locations 'fit' to the model and not to the true subsurface and hence can be considered a minimum bound in the location accuracy.

One drawback of the grid search algorithm used was that it could only give a spherical error surface. The distance uncertainties quoted hence refer to the length on the radius in a sphere of uncertainty surrounding the event. It was predicted that the greatest location inaccuracy would be the depth of the event, due to the inconsistency of the dip azimuth (see 8.4). The error surface would also be elongated in the direction perpendicular to the ray vector; this would depend on the orientation of the event with the respect to the two observation wells.

In section 6.3.2 it was highlighted that patterns of arrivals (P and S move-out and separation) were very characteristic of the layer the event was located in due to the high velocity contrasts between layers: A1.5 shows an example of this effect. This ensured the uncertainty in P and S arrival time picking was substantially less than the arrival time difference in P and S separation for an event located in another geological layer. A confident conclusion could be made regarding the origin layer of the seismic event. This appears to help constrain the depth of the event. However, it was also noted that it was very difficult to locate the depth of an event inside a geological layer. Move-out discrimination for events located inside the reservoir was very poor; this often appeared to be less than the uncertainty in the arrival time picking.

In A1.8 an estimate of the uncertainty was made by locating an event using arrival time picks on both arrays to see the error in the location to an event that was known relatively accurately. This event was located less than 230 m from the furthest receiver in the Stedum well. The event location was determined to have a location error of 10 m; the event also was located at an epicentre distance 19 m from Magnitudes value, and at a depth 49 m from Magnitudes value. Arrival time picks were then made on the Zeerijp well array seismograms. The grid search algorithm then determined the estimated event location using the arrival time inversion using

both arrays. This event location algorithm determined this position to be located at an epicentre distance of 26 m from this reference value and at a depth located 11m below. The epicentre distance was small compared to the total distance from the Zeerijp well array of 3026m.

This test appeared to demonstrate the importance of the source-receiver distance in determining the accuracy of the event. As long as an event was located close to a receiver, the location could be determined with a low residual error.

8.2.2. Limitations of velocity model

There were obvious limitations of using the 1D layered velocity model used in ray-tracing. Firstly, the changes in velocity across the reservoir could not be accounted for. The model split the reservoir into two layers averaging the velocity for these zones. The sonic logs however showed a smoothly varying velocity across the reservoir. Furthermore, lateral variations in the velocity model could not be accounted for. The greatest issue with the velocity model was that it could not account for the change in interface heights as shown in the seismic section in Figure 2. Most notably the height of the Anhydrite at the Stedum well was 57m higher than the Zeerijp well and a graben of a maximum Anhydrite depth of roughly 80m below that used in the velocity model also may have significantly affected the ray-tracing. The velocity from the reservoir to the carboniferous was smoothly varying and the velocity model averaged these velocities, consequently this effect was reduced at the reservoir-carboniferous interface.

The velocity model used in the event location in InSite required constant velocity layers and a velocity gradient could not be established. Consequently, an average velocity value obtained from the sonic logs was used to build the velocity model. This model was suitable for the Rotliegend-Anhydrite interface, where an abrupt 2km/s velocity change was observed over a short distance of 3m at both the Stedum and Zeerijp wells at this interface of these layers. However, it could not effectively model the velocity gradient in the Rotliegend and the more gradual velocity transition between the Rotliegend and Carboniferous. Hence discretising the velocity into blocks oversimplified the true velocity structure of the subsurface.

There also appeared to be a large cluster of events located just beneath the Anhydrite-Rotliegend interface; it is interesting that the 'best fit' location of these events was in the outer bounds of the geological layer in the velocity model. This could of course imply that the seismicity is expected at a greater extent at the layer interfaces. However, it appears more likely that this is due to the limitation of using a one dimensional velocity model. The waveforms showed clear characteristics in its P and S arrivals of originating from a certain geological layer due to the layer velocity. However, as the layer interfaces are not constant in depth, an event may have occurred in a set geological layer at a depth, which is modelled as outside the bounds of the layer in the velocity model. Consequently, a best fit location is found inside the model layer at its boundary. For example, event 22/03/14 15:16:15 was estimated to have occurred at a depth of 2901m; a large number of events were determined to have roughly this same depth. In the velocity model, the upper and lower parts of the reservoir are split into a low and high velocity interface respectively. This particular event depth corresponds to the higher velocity bottom segment of the reservoir. However, this depth also positions this event at the upper boundary of this velocity layer. It may be possible that this event occurred in the upper reservoir propagating at a velocity more consistent with that of the lower reservoir, however, based on the velocity model, this propagation path is not accounted for. Hence, the event is positioned in the lower segment as the ray-path through this layer is more consistent with the P and S arrival times due to its modelled velocity.

The choice in using the Tian ray-tracing method functioning on a 1D model was a balance of accuracy and time efficiency. A possible extension of this project would be building a 3D velocity model of the subsurface to account for the difference in interface heights.

8.3. Use of grid search method

The grid search algorithm provided the benefit that it provided a fast convergence to locate the event. A search over a volume could be performed: this had the advantage over the Geiger algorithm, which was highly dependent on the starting location for the iteration, which could lead to the algorithm identifying a local rather than a global minimum.

8.4. Analysis of relative location methods

An attempt was made to determine the locations of the event using the relative location method. However, the main issue with this method was the requirement that the reference source point was known accurately and that the distance between the event and the reference point was less than 10% of the total source-receiver distance (Mendecki, Aswegen, & Mountfort, 1999). The precision with which the location of the event could be determined depended on the distance to the closest receiver array. The arrivals that were most accurately determined (based on their location residual error) were positioned close to one of the receiver wells; consequently, the source-receiver distance was too short to satisfy this 10% criterion stipulated. There were also no distance events determined that produced a residual error low enough to be considered accurate enough to use as a reference event. This ruled out the possibility of using the relative location method in the dataset examined.

8.5. Azimuth & dip angle

It was observed in the data that the azimuthal angles varied by roughly 15 degrees in the data. As expected reflections and mode conversions had little effect on the ray azimuth. However, the dip angle of the events varied dramatically. The dip angles in the upper three geophones of both wells were considered unreliable: the source vector had a very low linearity and the dip appeared highly variant. This indicated that reflections and mode conversions were still affecting the source angle of the direct waves.

Both the waveform polarisation and linearity had proved useful in determining the S direct arrivals from the mode conversions. Scattered or reflected energy tended to have a weak polarisation compared to direct wave energy. The dip angle also proved effective at distinguishing the direct P-wave from the headwaves in the lower geophones. The source vector, linearity and polarisation may be possible parameters to focus on for the development of an auto-picking procedure, as it became clear that picking on first break P and S wave energy proved problematic.

8.6. Evidence of Faults

Examining the epicentres of the events on Figure 22, it appears that a number of events align in the north-westerly direction, in line with the direction of known faulting in the Groningen field. However, the error in the event location is too large to conclude that an event matched to a particular fault. Furthermore, it would be expected that there would be a far larger number of smaller faults that are sub-seismic in scale; movement on these undetected faults could potentially trigger earthquakes of a magnitude seen in this dataset. Therefore, no definitive conclusions could be made in this project regarding assigning seismic events to reactivated faults.

8.7. Discussion on Magnitude's work

Magnitudes ray tracing approach relied on the identification of the first energy arrival and the S wave. Due to the higher velocity Anhydrite and Carboniferous layers above and beneath the reservoir respectively, headwaves were the first arrivals observed in the seismograms. Raytracing algorithms using headwaves were considered in this project as an arrival pick that could have been made instead of the direct P arrival. This would have avoided the difficulty in determining the direct arrival from the preceding headwaves. However, headwaves are far weaker in amplitude than direct arrivals, especially at far offsets, making their detection difficult. Furthermore, it was concluded by Zimmer that the depth accuracy in particular is very poor for events identified by the arrival times of headwaves (Zimmer, 2010). Headwaves approach the receiver array at very similar dip angles, which decreases the effective aperture of the array. This may explain Magnitudes anomalous depth results.

Furthermore, it appears that P-S conversions may have been incorrectly picked as the direct S-wave arrival. A1.3.1 shows example interpreted seismograms by Magnitude showing a clear mismatch between the picked S and computed S arrival highlighting their difficulty in determining S-wave arrivals.

The results from the finite difference modelling was used to interpret the P to S mode conversions based on their move-out in this study. This was used to distinguish the direct S and converted S arrivals. The interpretations of the seismograms seen in Magnitude's example events can also be found in A1.3.

8.8. Future work & and result implications

The anomalous results produced by Magnitude, an experienced microseismic service company, had highlighted the difficulty in locating seismic events in Groningen field. It indicated that for this project, a more interpretive method of the arrival time picking needed to be developed in order for the seismic events to be located accurately. The interpretation methods used in this project have been time-consuming to implement; for a large amount of events to be processed, an automated system would need to be developed to avoid the heavy personnel costs in locating arrivals on the seismograms.

The difficulty in using automatic-processing methods for determining event locations was also highlighted in this project. The high velocity contrasts between the Anhydrite and the reservoir has been responsible for the complex seismograms recorded at the receiver arrays, leading to the difficulty in determining arrivals. As the P and S wave arrivals are preceded by relatively high amplitude headwaves and P-S conversions respectively, this rules out the possibility of auto-picking on first breaks.

However, there may be some scope for an automatic system to be developed based on developing an algorithm that will automate the interpretation methods used in this project. Use of the waveform linearity and polarisation proved useful in determining direct arrival times. An algorithm could be developed to estimate arrival times based on these parameters reaching a threshold value. A form of forward modelling process may also prove effective to match peaks on to expected arrival times produced using forward modelling.

This project in a sense occupies a middle ground between frac monitoring and standard earthquake seismology. Monitoring wells for hydraulic fracturing tend to be placed at a far closer proximity to the injector well for accurate fracture location. Consequently events will be located far less than 1Km from a receiver enabling them to be determined more accurately. Standard

earthquake monitoring methods using surface geophones locate events at a much greater magnitude and distance; however, the level of precision in location is unsuitable for use in this project. The Dutch regulator KNMI's monitoring of the Groningen field using surface arrays produced locations with depth uncertainties of several kilometres, justifying the need for the reservoir level monitoring arrays that have produced the data in this study (NAM, November 2013). Two further reservoir level monitoring wells have been proposed by NAM to be drilled from the Zeerijp well location to monitor the seismic activity in the field. These are set to replace the use of the Stedum-1 and Zeerijp-1 wells for passive seismic monitoring. A further two hundred near surface (<200m depth) monitoring wells will also be drilled.

Another microseismic service company ESG was contracted to provide location estimates of five of the events processed in this report. They will examine the dataset to both locate the events and determine the feasibility for the events to be auto-processed. Discussions are also in progress for the regulator KNMI to process the data from the reservoir level arrays.

Shell is currently looking into using full waveform inversion to process the data from this field. As this project has highlighted, using direct arrivals to locate events has proved difficult due to the nature of the field. It appears that full waveform inversion would be more suitable for this particular field as it removes the uncertainty in picking the direct arrivals. The event estimate locations determined in this work will act as 'seed points' for the inversion process in the full waveform inversion.

If the results of the full waveform inversion match the results obtained in this study, it would provide further confirmation of this projects conclusion that the seismic events are occurring close to reservoir level in the Groningen field.

9. Conclusion

This study has produced re-estimates of the locations of the induced earthquakes for 32 events recorded by the reservoir level Stedum-1 and Zeerijp-1 monitoring well arrays in the Groningen gas field. It was concluded that the events were occurring in and around the Rotliegend reservoir with a mean event depth of 2921m, corresponding to the approximate depth of the reservoir centre around the area of the observation wells. This re-estimated the locations of the events estimated by a service contractor on this dataset. This study used arrival time inversion methods to locate the events using Tian's method of ray tracing and a grid search location algorithm. Due to the complexity of the seismograms observed, forward modelling and the analysis of the source vector, linearity and polarisation of the waveforms were required to estimate the P and S direct arrival times, for the arrival time inversion algorithm. Whilst the mean residual distance error of the events was 83m, it was determined that the uncertainty bounds were far larger than the residual; however, the waveform characteristics (move-out and separation) help to distinguish with confidence the geological layer the event originated from. This study also highlighted the difficulty in implementing an accurate automated P and S arrival picking procedure, and suggested that full waveform inversion may provide more accurate results compared to direct arrival inversion methods.

10. References

- Applied seismology Consultants. (2014). *InSite user manual v3.2 Technical appendix*. InSite.
- Brace, W. F., & Byerlee, J. D. (n.d.). Stick-Slip as a Mechanism for Earthquakes. *Science, New Series, Vol. 153, No. 3739. (Aug. 26, 1966), pp. 990-992.*
- C.Hanks, T., & Kanamori, H. (1979). A moment magnitude scale. *Journal of geophysical research* , 84 (B5).
- Dost, B., & Haak, H. (2007). *Natural and Induced Seismicity, In Geology of the Netherlands*. Amsterdam, Royal Netherlands Academy of Arts and Sciences, ISBN 978-90-6984-481-7, p223-239.
- Dost, B., Goutbeek, F., Eck, T. v., & Kraaijpoel, D. (2010). *Monitoring induced seismicity in the North of the Netherlands: status report 2010*. Royal Netherlands Meteorological institute of ministry of infrastructure and the environment.
- Eck, T. v., Goutbeek, F., Haak, H., & Dorst, B. (2004). *Seismic hazard due to small shallow induced earthquakes*. De Bilt: KNMI.
- Geiger, L. (1912). Probability method for the determination of earthquake epicenters from the arrival time only . *Bull.St.Louise.University* , 8(1), 56-71.
- Gibowicz, S. J., & Kijko, A. (1994). *An introduction to mining seismology*. Warsaw, Poland: Academic Press, Institute of Geophysics, Polish academy of sciences.
- Grechka, V., & Yasevich, S. (2013). Inversion of microseismic data for triclinic velocity models. *European Association of Geoscientists and Engineers, Geophysical Prospecting* , 61, 1159–1170.
- Grotsch, J. G. S. (2011). *The Groningen Gas Field: Fifty years of exploration and gas production from a permian dryland reservoir*. NAM.
- Gutenberg, B., & Richter, C. F. (1949). *Seismicity of the Earth and associated phenomena*. Princeton, New Jersey: Princeton University Press, Seismological Laboratory California Institute of Technology.
- Hanyga, A. (1991). Implicit curve tracing and point-to-curve ray tracing. *Seismological observ Univeristy of Bergen, Norway* .
- Havskov, J. (2002). *Earthquake location*. Univeristy of Bergen, Department of Earth Science.
- Houtgast, G. (1991). *Catalogus Aardbevingen in Nederland*. . Royal Netherlands Meteorological Institute (De Bilt), ISBN: 90-369-2002-7: 166 pp.
- Igel, H., Mora, P., & Rioulet, B. (1995). Anisotropic wave propagation through finite-difference grid. *Geophysics, Vol. 60, NO. 4* , 1203-1216.
- Ketelaar, V. B. (2009). *Satellite Radar Interferometry , Subsidence Due to Hydrocarbon Production in the Netherlands, Volume 14, 2009, pp 7-26* . Springer Netherlands.
- Kraaijpoel, D., & Dost, B. (2013). *the August 16, 2012 earthquake near Huizinge (Groningen)*. De Bilt: KNMI.
- Lee, W., & Stewart, S. (1981). *Principles and applications of microearthquake networks*. California: Academic press, Office of earthquake studies, U.S geological survey.
- McGarr, A. (1976). Seismic moments and volume changes. *Journal of geophysical research* , 81 (8).
- Mendecki, A. J., Aswegen, G. V., & Mountfort, P. (1999). *A handbook on rock engineering practise for tabular hard rock mines*. Cape town: published by Creda Communications on behalf of the Safety in Mines research advisory committee to the department of minerals and energy of south Africa.
- Mendecki, A. (1997). *Seismic monitoring in Mines*. London: Chapman and Hall.
- Ministry of Economic affairs. (2013). *Reassessment of the prabability of higher magnitude earthquakes in the Groningen gas field*. State supervision of mines.

Montalbette, J. F., & Kanasewich, E. R. (1970). Enhancement of teleseismic body phases with a polarisation filter. *Geophys. J. R. astr. Soc. (1970)* , 21, 119-129.

NAM. (November 2013). *Technical Addendum to the Winningsplan Groningen 2013 subsidence, Induced Earthquakes and seismic hazard analysis in the Groningen Field*. Nederlandse Aardolie Maatschappij.

Seismic tools specifications. (2014). Retrieved from Sercel:

http://www.sercel.com/products/Lists/ProductSpecification/Downhole_Seismic%20tools_specifications_Sercel.pdf

Stauble, A., & Milius, G. (1970). *Geology of the Groningen Gas Field, Neatherlands*. American association of petroleum geologists.

Tian, Y. T., & Chen, X.-f. (2005). *A rapid and accurate two-point ray tracing method in horizontally layered velocity model*. Beijing China: Department of Geophysics, Peking University,.

Vidale, J. (1988). Finite difference calculation of traveltimes. *Bulletin of the Seismological Society of America* , Vol. 78, No. 6, pp. 2062-2076.

Vidale, J. (1990). Finite-difference calculation of traveltimes in three dimentions. *Geophysics* , Vol.55, NO. 5 May 1990;P. 521-526, 8 FIGS.

Vinje, V., Iversen, E., & Gjoystdal, H. (1993). Traveltime and amplitude estimation using wavefront construction. *Geophysics* , Vol 58, NO. 8 (August 1993); P. 1157-1166,16 Figs.

Waldhauser, F., & Ellsworth, W. L. (2000). A double-difference earthquake location algorithm: method and application to the northern hayward fault california. *Bulletin of the Seismological society of America* , 90, 1353-1368.

Zimmer, U. (2010). *Localization of microseismic events using headwaves and direct waves*. Denver: Society of exploration geophysicists, Pinnacle a Halliburton service.

APPENDIX

A1.1. Table of Results

The table below shows the processed results produced. Traces are identified by date and time of recording. True vertical depths of events are referenced to sea level. Origin time is given to 2 decimal places. Errors, derived from residuals, are shown for time, distance and source vectors. Blank cells in table where location algorithm failed to obtain estimates.

Trace identity		Location (m)			Origin time	Magnitude ²	Residual errors		
Date	Trace time	Northing	Easting	Depth (TVD)			Time (s)	Distance (m)	angle (deg)
23-11-2013	1:08:35	597434	245228	2900					
30-11-2014	19:29:01	597452	245268	2901	19:29:05,14	0	0.0427	125	17.7
1-12-2013	9:21:03	593686	244254	2905	9:21:06,76	-1.09	0.0297	85.4	27.5
15-12-2013	6:48:25	596448	242723	2993	6:48:26,31	-1.16	0.0406	114.6	17.3
15-12-2014	7:39:55	593125	242991	2901	07:39:57,97	0.32	0.0506	136.1	19.7
17-12-2013	21:37:55	595694	246797	2901	21:37:56,19	0.85	0.058	150.4	25.6
21-3-2014	8:23:48	596002	244077	3063	8:23:49,64	-1.48	0.0364	96.3	32.9
21-3-2014	11:28:28	595818	244700	3050	11:28:28,96	-0.48	0.0381	134.4	34.7
22-3-2014	15:10:08	595718	243416	3057				36.7	13.4
22-3-2014	17:16:15	596171	243609	2901	17:16:19,10	-0.74	0.0161	45	25.4
23-3-2014	2:23:55	594498	243709	2950	2:23:56,64	-0.3	0.0184	51.1	
23-3-2014	19:56:05	594127	244497	2720		0.04	0.0115	76	44.7
24-3-2014	23:38:39	595688	244543	2772	23:38:43,22			80.5	13.2
25-3-2014	13:20:58	596159	243577	3026	13:21:00,27	-0.08	0.0155	50.5	25.9
1-4-2014	20:08:56	595759	244647	2901	20:09:11,87	-0.34	0.0361	103.7	36.6
1-4-2014	14:13:06	596262	243646	2903	14:13:09,92	-0.65	0.0229	66.2	20.2
1-4-2014	18:35:13	594571	246812	3018	18:35:16,93	0.96	0.0374	92.9	20.9
6-4-2014	14:47:15	595315	245356	2911	14:47:18,96	-0.93	0.0315	97.6	22.9
9-4-2014	20:04:15	595198	242252	2878	20:04:21,43	-0.97	0.0099	26.4	3.35
10-4-2014	20:56:00	596011	241148	2902	20:56:04,07	-0.09	0.0138	42.9	23.4
11-4-2014	20:48:31	596214	246125	2904	20:48:33,08	0.94	0.0207	66.8	37.7
12-4-2014	5:36:04	595580	245343	2834	5:36:07,83	-0.38	0.037	94.5	11.7
12-4-2014	12:56:10	595193	245163	3032	12:56:13,92	-0.62	0.0287	86.2	23.9
15-04-14	21:43:24	594675	243553	2906	21:43:24,67	-0.63	0.0188	53.1	2.22
17-4-2014	20:21:01	592799	243050	2720	20:21:05,06	1.06	0.024	58.9	32.7
17-4-2014	1:46:35	594705	243554	2770	1:46:39,14	-0.03	0.0209	57.1	31.1
20-04-14	8:36:00	596820	245563	3033	08:36:3,06	1.26	0.0406	117.4	32.9
20-4-2014	11:20:14	592736	242899	2766	11:20:21,71	-0.22	0.021	44.8	39.2
22-4-2014	13:13:14	595706	245058	3065	13:13:20,62	0.46	0.0349	94.3	38.1
3-5-2014	20:39:06	595462	244565	2902	20:40:03,01	-1.08	0.0464	132	31
6-5-2014	3:23:58	593698	243592	3032	3:24:01,71	-0.39	0.0234	63.7	32.5
6-5-2014	11:32:01	595348	245143	2970	11:32:01,37		0.0312	84.6	28.6

² After initial release of this report, event magnitudes were amended to account for 52v/m/s sensitivity of geophones: magnitudes quoted here have been reduced by 1.14 ($=2(\log_{10}52)/3$) compared with the values originally given.

A1.2. Geophone information and orientations

A1.2.1. Check shots

Check shots were performed during the first phase of recording on 27/11/2013. In the second phase, after the replacement of the geophone arrays new check shots were performed on the 25/03/2014. Eight check shots were performed during the first period of recording, and 5 check shots were used to check the orientations during the second phase of recording. Geophone orientations were obtained by Magnitude, and were quality checked for accuracy. The geophone hodograms were checked for consistent ray azimuths down the array. To determine the accuracy, the locations of the known shot points were compared to the locations obtained by the location algorithm.

A1.2.2. Orientation coordinates & Geophone information

The geophones recorded data in a left-handed co-ordinate system whilst the InSite software uses a right handed system. The geophone orientations were provided in the form of a North-East (θ) and up bearings (Φ). InSite required the data to be entered in a North, East and down orientation, and was transformed using the following spherical co-ordinate transformation:

$$North = \cos\theta\sin\Phi$$

$$East = \sin\theta\sin\Phi$$

$$Down = -\cos\Phi$$

Initially dramatic variations between the ray azimuths were observed down the geophone arrays in each well. Consequently, the location algorithm was unable to find a stable solution and locations estimated by each well had large variations. A minus 1 was then applied to the east (Y) component of the geophone to transform the locations to a right handed co-ordinate system..

Table 5 and Table 6 show the geophone orientations and specifications for the two periods of recoding in this study.

Table 5 Geophone orientations for Phase 1 events between 21/11/14 to 23/12/14

Number	Casing Label	Sensor Label	North	East	Down	On	Type	Axis number	Casing Number	Gain	Sensitivity	Vmax	Low freq	High freq	Orientation_N	Orientation_E	Orientation_D	Motion	P Station correction	S Station correction	Owner Array	Array Instrument number	Array channel number
1	S001	SD001	242433.3	595117.5	2751	1	0	0	1	52	52	10	1	250	0.49174	-0.82818	0.26892	1	0	0	SDMa	1	1
2	S001	SD001	242433.3	595117.5	2751	1	0	1	1	52	52	10	1	250	-0.86317	-0.5044	0.02269	-1	0	0	SDMa	1	2
3	S001	SD001	242433.3	595117.5	2751	1	0	2	1	52	52	10	1	250	0.1165	-0.24424	-0.96269	1	0	0	SDMa	1	3
4	S002	SD002	242430.3	595124.1	2780.1	1	0	0	2	52	52	10	1	250	-0.74115	-0.66733	0.07324	1	0	0	SDMa	2	4
5	S002	SD002	242430.3	595124.1	2780.1	1	0	1	2	52	52	10	1	250	-0.66425	0.71232	-0.22665	-1	0	0	SDMa	2	5
6	S002	SD002	242430.3	595124.1	2780.1	1	0	2	2	52	52	10	1	250	0.10005	-0.21654	-0.97113	1	0	0	SDMa	2	6
7	S003	SD003	242427.3	595129.8	2809.5	1	0	0	3	52	52	10	1	250	0.95021	-0.27966	0.13744	1	0	0	SDMa	3	7
8	S003	SD003	242427.3	595129.8	2809.5	1	0	1	3	52	52	10	1	250	-0.29873	-0.94171	0.15471	-1	0	0	SDMa	3	8
9	S003	SD003	242427.3	595129.8	2809.5	1	0	2	3	52	52	10	1	250	0.08721	-0.18874	-0.97815	1	0	0	SDMa	3	9
10	S004	SD004	242425.9	595135.1	2838.9	1	0	0	4	52	52	10	1	250	0.73012	-0.66436	0.15988	1	0	0	SDMa	4	10
11	S004	SD004	242425.9	595135.1	2838.9	1	0	1	4	52	52	10	1	250	-0.68151	-0.72573	0.09411	-1	0	0	SDMa	4	11
12	S004	SD004	242425.9	595135.1	2838.9	1	0	2	4	52	52	10	1	250	0.05273	-0.17802	-0.98261	1	0	0	SDMa	4	12
13	S005	SD005	242424.6	595139.7	2868.6	1	0	0	5	52	52	10	1	250	0.62273	-0.76901	0.14436	1	0	0	SDMa	5	13
14	S005	SD005	242424.6	595139.7	2868.6	1	0	1	5	52	52	10	1	250	-0.78115	-0.62135	0.06105	-1	0	0	SDMa	5	14
15	S005	SD005	242424.6	595139.7	2868.6	1	0	2	5	52	52	10	1	250	0.04181	-0.15075	-0.98769	1	0	0	SDMa	5	15
16	S006	SD006	242424.1	595144.1	2898.2	1	0	0	6	52	52	10	1	250	0.88229	-0.46321	0.08368	1	0	0	SDMa	6	16
17	S006	SD006	242424.1	595144.1	2898.2	1	0	1	6	52	52	10	1	250	-0.47065	-0.8741	0.12014	-1	0	0	SDMa	6	17
18	S006	SD006	242424.1	595144.1	2898.2	1	0	2	6	52	52	10	1	250	0.01755	-0.14502	-0.98927	1	0	0	SDMa	6	18
19	S007	SD007	242423.2	595148	2928	1	0	0	7	52	52	10	1	250	-0.80783	-0.58693	0.05408	1	0	0	SDMa	7	19
20	S007	SD007	242423.2	595148	2928	1	0	1	7	52	52	10	1	250	-0.58912	0.79906	-0.12014	-1	0	0	SDMa	7	20
21	S007	SD007	242423.2	595148	2928	1	0	2	7	52	52	10	1	250	0.0284	-0.12917	-0.99122	1	0	0	SDMa	7	21
22	S008	SD008	242422.3	595151.5	2957.7	1	0	0	8	52	52	10	1	250	0.8983	-0.43232	0.07846	1	0	0	SDMa	8	22
23	S008	SD008	242422.3	595151.5	2957.7	1	0	1	8	52	52	10	1	250	-0.43813	-0.89433	0.09063	-1	0	0	SDMa	8	23
24	S008	SD008	242422.3	595151.5	2957.7	1	0	2	8	52	52	10	1	250	0.03065	-0.11437	-0.99297	1	0	0	SDMa	8	24

25	S009	SD009	242421.4	595154.7	2987.6	1	0	0	9	52	52	10	1	250	0.95141	-0.30181	0.06105	1	0	0	SDMa	9	25
26	S009	SD009	242421.4	595154.7	2987.6	1	0	1	9	52	52	10	1	250	-0.30604	-0.94753	0.09237	-1	0	0	SDMa	9	26
27	S009	SD009	242421.4	595154.7	2987.6	1	0	2	9	52	52	10	1	250	0.02979	-0.10741	-0.99377	1	0	0	SDMa	9	27
28	S010	SD010	242420.6	595157.6	3017.4	1	0	0	10	52	52	10	1	250	0.33596	0.9383	-0.08194	1	0	0	SDMa	10	28
29	S010	SD010	242420.6	595157.6	3017.4	1	0	1	10	52	52	10	1	250	0.94108	-0.33325	0.05756	-1	0	0	SDMa	10	29
30	S010	SD010	242420.6	595157.6	3017.4	1	0	2	10	52	52	10	1	250	0.02654	-0.09571	-0.99506	1	0	0	SDMa	10	30
31	S011	ZR011	245012	596465.3	2781.2	1	0	0	11	52	52	10	1	250	-0.34931	-0.93428	0.0715	1	0	0	ZRPa	1	1
32	S011	ZR011	245012	596465.3	2781.2	1	0	1	11	52	52	10	1	250	-0.93685	0.34655	-0.04711	-1	0	0	ZRPa	1	2
33	S011	ZR011	245012	596465.3	2781.2	1	0	2	11	52	52	10	1	250	0.0249	-0.08352	-0.99619	1	0	0	ZRPa	1	3
34	S012	ZR012	245011.3	596467.5	2811.2	1	0	0	12	52	52	10	1	250	0.19539	-0.97785	0.07498	1	0	0	ZRPa	2	4
35	S012	ZR012	245011.3	596467.5	2811.2	1	0	1	12	52	52	10	1	250	-0.98025	-0.19765	-0.00698	-1	0	0	ZRPa	2	5
36	S012	ZR012	245011.3	596467.5	2811.2	1	0	2	12	52	52	10	1	250	0.0218	-0.07174	-0.99719	1	0	0	ZRPa	2	6
37	S013	ZR013	245010.7	596469.3	2841.1	1	0	0	13	52	52	10	1	250	-0.99358	-0.11145	-0.0192	1	0	0	ZRPa	3	7
38	S013	ZR013	245010.7	596469.3	2841.1	1	0	1	13	52	52	10	1	250	-0.11125	0.99181	-0.06279	-1	0	0	ZRPa	3	8
39	S013	ZR013	245010.7	596469.3	2841.1	1	0	2	13	52	52	10	1	250	0.02256	-0.06232	-0.9978	1	0	0	ZRPa	3	9
40	S014	ZR014	245009.9	596471.1	2871	1	0	0	14	52	52	10	1	250	0.49291	-0.86768	0.06453	1	0	0	ZRPa	4	10
41	S014	ZR014	245009.9	596471.1	2871	1	0	1	14	52	52	10	1	250	-0.87031	-0.4924	0.01047	-1	0	0	ZRPa	4	11
42	S014	ZR014	245009.9	596471.1	2871	1	0	2	14	52	52	10	1	250	0.02493	-0.0614	-0.9978	1	0	0	ZRPa	4	12
43	S015	ZR015	245009.1	596472.9	2901	1	0	0	15	52	52	10	1	250	-0.90742	0.41737	-0.04885	1	0	0	ZRPa	5	13
44	S015	ZR015	245009.1	596472.9	2901	1	0	1	15	52	52	10	1	250	0.42053	0.90596	-0.04885	-1	0	0	ZRPa	5	14
45	S015	ZR015	245009.1	596472.9	2901	1	0	2	15	52	52	10	1	250	0.02614	-0.06279	-0.99768	1	0	0	ZRPa	5	15
46	S016	ZR016	245008.9	596474.9	2930.9	1	0	0	16	52	52	10	1	250	0.99974	0.02269	0.00349	1	0	0	ZRPa	6	16
47	S016	ZR016	245008.9	596474.9	2930.9	1	0	1	16	52	52	10	1	250	0.02264	-0.99766	0.06453	-1	0	0	ZRPa	6	17
48	S016	ZR016	245008.9	596474.9	2930.9	1	0	2	16	52	52	10	1	250	0.00551	-0.0643	-0.99792	1	0	0	ZRPa	6	18
49	S017	ZR017	245008.5	596476.8	2960.8	1	0	0	17	52	52	10	1	250	-0.1956	-0.97889	0.05931	1	0	0	ZRPa	7	19
50	S017	ZR017	245008.5	596476.8	2960.8	1	0	1	17	52	52	10	1	250	-0.98062	0.19417	-0.02618	-1	0	0	ZRPa	7	20
51	S017	ZR017	245008.5	596476.8	2960.8	1	0	2	17	52	52	10	1	250	0.01506	-0.06275	-0.99792	1	0	0	ZRPa	7	21

Table 6 Geophone orientations for events in the second phase of recording from 19/03/14 to 10/05/14

Number	Casing Label	Sensor Label	North	East	Down	On	Type	Axis number	Casing Number	Gain	Sensitivity	Vmax	Low freq	High freq	Orientation_N	Orientation_E	Orientation_D	Motion	P Station correction	S Station correction	Owner Array	Array Instrument number	Array channel number
1	s001	SD001	5951 17.1	2424 33.6	2749. 1	1	0	0	1	52	52	10	1	250	0.29269	-0.91712	0.2706	1	0	0	SDMa	1	1
2	s001	SD001	5951 17.1	2424 33.6	2749. 1	1	0	1	1	52	52	10	1	250	-0.94885	-0.3138	-0.0349	1	0	0	SDMa	1	2
3	s001	SD001	5951 17.1	2424 33.6	2749. 1	1	0	2	1	52	52	10	1	250	0.11722	-0.24576	-0.96222	1	0	0	SDMa	1	3
4	s002	SD002	5951 23.7	2424 30.5	2778. 2	1	0	0	2	52	52	10	1	250	-0.92448	-0.38104	-0.01222	1	0	0	SDMa	2	4
5	s002	SD002	5951 23.7	2424 30.5	2778. 2	1	0	1	2	52	52	10	1	250	-0.36678	0.89876	-0.24023	1	0	0	SDMa	2	5
6	s002	SD002	5951 23.7	2424 30.5	2778. 2	1	0	2	2	52	52	10	1	250	0.10152	-0.21772	-0.97072	1	0	0	SDMa	2	6
7	s003	SD003	5951 29.5	2424 27.8	2807. 5	1	0	0	3	52	52	10	1	250	-0.89176	-0.45242	0.00873	1	0	0	SDMa	3	7
8	s003	SD003	5951 29.5	2424 27.8	2807. 5	1	0	1	3	52	52	10	1	250	-0.44407	0.87154	-0.20791	1	0	0	SDMa	3	8
9	s003	SD003	5951 29.5	2424 27.8	2807. 5	1	0	2	3	52	52	10	1	250	0.08726	-0.19059	-0.97778	1	0	0	SDMa	3	9
10	s004	SD004	5951 34.8	2424 26	2837	1	0	0	4	52	52	10	1	250	-0.71054	-0.69824	0.08716	1	0	0	SDMa	4	10
11	s004	SD004	5951 34.8	2424 26	2837	1	0	1	4	52	52	10	1	250	-0.70085	0.69354	-0.16677	1	0	0	SDMa	4	11
12	s004	SD004	5951 34.8	2424 26	2837	1	0	2	4	52	52	10	1	250	0.05603	-0.17881	-0.98229	1	0	0	SDMa	4	12
13	s005	SD005	5951 39.4	2424 24.7	2866. 6	1	0	0	5	52	52	10	1	250	-0.9841	-0.17707	-0.01396	1	0	0	SDMa	5	13
14	s005	SD005	5951 39.4	2424 24.7	2866. 6	1	0	1	5	52	52	10	1	250	-0.17151	0.97268	-0.15643	1	0	0	SDMa	5	14
15	s005	SD005	5951 39.4	2424 24.7	2866. 6	1	0	2	5	52	52	10	1	250	0.04227	-0.15241	-0.98741	1	0	0	SDMa	5	15
16	s006	SD006	5951 43.8	2424 24.1	2896. 2	1	0	0	6	52	52	10	1	250	-0.99956	-0.02617	-0.01396	1	0	0	SDMa	6	16
17	s006	SD006	5951 43.8	2424 24.1	2896. 2	1	0	1	6	52	52	10	1	250	-0.02417	0.98898	-0.14608	1	0	0	SDMa	6	17
18	s006	SD006	5951 43.8	2424 24.1	2896. 2	1	0	2	6	52	52	10	1	250	0.01704	-0.14509	-0.98927	1	0	0	SDMa	6	18
19	s007	SD007	5951 47.8	2424 23.3	2926	1	0	0	7	52	52	10	1	250	0.32598	-0.93608	0.13226	1	0	0	SDMa	7	19
20	s007	SD007	5951 47.8	2424 23.3	2926	1	0	1	7	52	52	10	1	250	-0.94483	-0.32718	0.01571	1	0	0	SDMa	7	20
21	s007	SD007	5951 47.8	2424 23.3	2926	1	0	2	7	52	52	10	1	250	0.02854	-0.13091	-0.99098	1	0	0	SDMa	7	21
22	s008	SD008	5951 51.3	2424 22.4	2955. 8	1	0	0	8	52	52	10	1	250	-0.97635	0.20931	-0.05408	1	0	0	SDMa	8	22

23	S008	SD008	5951 51.3	2424 22.4	2955. 8	1	0	1	8	52	52	10	1	250	0.21352	0.97114	-0.10626	1	0	0	SDMa	8	23
24	S008	SD008	5951 51.3	2424 22.4	2955. 8	1	0	2	8	52	52	10	1	250	0.03069	-0.11615	-0.99276	1	0	0	SDMa	8	24
25	S009	SD009	5951 54.5	2424 21.5	2985. 6	1	0	0	9	52	52	10	1	250	0.50457	-0.85659	0.108	1	0	0	SDMa	9	25
26	S009	SD009	5951 54.5	2424 21.5	2985. 6	1	0	1	9	52	52	10	1	250	-0.86306	-0.50433	0.02792	1	0	0	SDMa	9	26
27	S009	SD009	5951 54.5	2424 21.5	2985. 6	1	0	2	9	52	52	10	1	250	0.02979	-0.10741	-0.99377	1	0	0	SDMa	9	27
28	S010	SD010	5951 57.5	2424 20.6	3015. 4	1	0	0	10	52	52	10	1	250	0.99946	-0.01745	0.02792	1	0	0	SDMa	10	28
29	S010	SD010	5951 57.5	2424 20.6	3015. 4	1	0	1	10	52	52	10	1	250	-0.01911	-0.99521	0.09585	1	0	0	SDMa	10	29
30	S010	SD010	5951 57.5	2424 20.6	3015. 4	1	0	2	10	52	52	10	1	250	0.02701	-0.09738	-0.99488	1	0	0	SDMa	10	30
31	S011	ZR011	5964 65.2	2450 12	2780. 3	1	0	0	11	52	52	10	1	250	0.9231	-0.38048	0.05582	1	0	0	ZRPa	1	1
32	S011	ZR011	5964 65.2	2450 12	2780. 3	1	0	1	11	52	52	10	1	250	-0.38501	-0.9204	0.06802	1	0	0	ZRPa	1	2
33	S011	ZR011	5964 65.2	2450 12	2780. 3	1	0	2	11	52	52	10	1	250	0.0249	-0.08352	-0.99619	1	0	0	ZRPa	1	3
34	S012	ZR012	5964 67.4	2450 11.4	2810. 3	1	0	0	12	52	52	10	1	250	-0.99352	0.10969	-0.02967	1	0	0	ZRPa	2	4
35	S012	ZR012	5964 67.4	2450 11.4	2810. 3	1	0	1	12	52	52	10	1	250	0.11121	0.99147	-0.06802	1	0	0	ZRPa	2	5
36	S012	ZR012	5964 67.4	2450 11.4	2810. 3	1	0	2	12	52	52	10	1	250	0.0218	-0.07174	-0.99719	1	0	0	ZRPa	2	6
37	S013	ZR013	5964 69.3	2450 10.7	2840. 2	1	0	0	13	52	52	10	1	250	0.087	0.99444	-0.05931	1	0	0	ZRPa	3	7
38	S013	ZR013	5964 69.3	2450 10.7	2840. 2	1	0	1	13	52	52	10	1	250	0.99596	-0.08538	0.02792	1	0	0	ZRPa	3	8
39	S013	ZR013	5964 69.3	2450 10.7	2840. 2	1	0	2	13	52	52	10	1	250	0.02256	-0.06232	-0.9978	1	0	0	ZRPa	3	9
40	S014	ZR014	5964 71.1	2450 09.9	2870. 1	1	0	0	14	52	52	10	1	250	0.9962	-0.0819	0.02967	1	0	0	ZRPa	4	10
41	S014	ZR014	5964 71.1	2450 09.9	2870. 1	1	0	1	14	52	52	10	1	250	-0.08353	-0.99474	0.05931	1	0	0	ZRPa	4	11
42	S014	ZR014	5964 71.1	2450 09.9	2870. 1	1	0	2	14	52	52	10	1	250	0.02429	-0.06166	-0.9978	1	0	0	ZRPa	4	12
43	S015	ZR015	5964 72.9	2450 09.1	2900. 1	1	0	0	15	52	52	10	1	250	0.99951	0.01745	0.02618	1	0	0	ZRPa	5	13
44	S015	ZR015	5964 72.9	2450 09.1	2900. 1	1	0	1	15	52	52	10	1	250	0.01568	-0.9979	0.06279	1	0	0	ZRPa	5	14
45	S015	ZR015	5964 72.9	2450 09.1	2900. 1	1	0	2	15	52	52	10	1	250	0.02788	-0.06204	-0.99768	1	0	0	ZRPa	5	15
46	S016	ZR016	5964 74.8	2450 08.9	2930	1	0	0	16	52	52	10	1	250	0.82667	0.56181	-0.03141	1	0	0	ZRPa	6	16
47	S016	ZR016	5964 74.8	2450 08.9	2930	1	0	1	16	52	52	10	1	250	0.56265	-0.82481	0.05582	1	0	0	ZRPa	6	17

48	S016	ZR016	5964 74.8	2450 08.9	2930	1	0	2	16	52	52	10	1	250	0.00551	-0.0643	-0.99792	1	0	0	ZRPa	6	18
49	S017	ZR017	5964 76.7	2450 08.5	2959. 9	1	0	0	17	52	52	10	1	250	-0.96031	0.27718	-0.03141	1	0	0	ZRPa	7	19
50	S017	ZR017	5964 76.7	2450 08.5	2959. 9	1	0	1	17	52	52	10	1	250	0.27856	0.9588	-0.05582	1	0	0	ZRPa	7	20
51	S017	ZR017	5964 76.7	2450 08.5	2959. 9	1	0	2	17	52	52	10	1	250	0.01463	-0.06285	-0.99792	1	0	0	ZRPa	7	21

A1.3. Analysis of Magnitude's Data

The location estimates of Magnitude for the events processed in this report are shown in Table 7. This section features both analysis of Magnitudes arrival time picking and their results.

Table 7 shows Magnitude's location estimations for the events located in the report.

Date	Trace time	Magnitude locations (m)		
		Northing	Easting	Depth
23-11-2013	1:08:35	597966	247283	4998
30-11-2014	19:29:01	597637	245880	3908
1-12-2013	9:21:03	593301	244539	4420
15-12-2013	6:48:25	596579	242440	5093
15-12-2014	7:39:55	592869	242393	5399
17-12-2013	21:37:55	596185	247956	4884
21-3-2014	8:23:48	595939	244102	3420
21-3-2014	11:28:28	595760	244700	3720
22-3-2014	15:10:08	595781	243380	4619
22-3-2014	17:16:15	596338	243640	4719
23-3-2014	2:23:55	593962	243781	4544
23-3-2014	19:56:05	594096	244100	4119
24-3-2014	23:38:39	595758	244675	3059
25-3-2014	13:20:58	596319	243600	4165
1-4-2014	20:08:56	595540	245219	3978
1-4-2014	14:13:06	596340	243700	4716
1-4-2014	18:35:13	593687	247351	5340
6-4-2014	14:47:15	594842	246140	4053
9-4-2014	20:04:15	595199	242260	2916
10-4-2014	20:56:00	596039	240462	4597
11-4-2014	20:48:31	596689	246202	3652
12-4-2014	5:36:04	596577	244941	4539
12-4-2014	12:56:10	594539	245532	4421
15-04-14	21:43:24	594675	243321	4679
17-4-2014	20:21:01	594098	243579	4619
17-4-2014	1:46:35	594605	243441	4368
20-04-14	8:36:00	596720	245340	3120
20-4-2014	11:20:14	593375	243120	4068
22-4-2014	13:13:14	595320	245460	3580
3-5-2014	20:39:06	595159	244992	3596
6-5-2014	3:23:58	593260	243600	3540
6-5-2014	11:32:01	596725	244740	5239

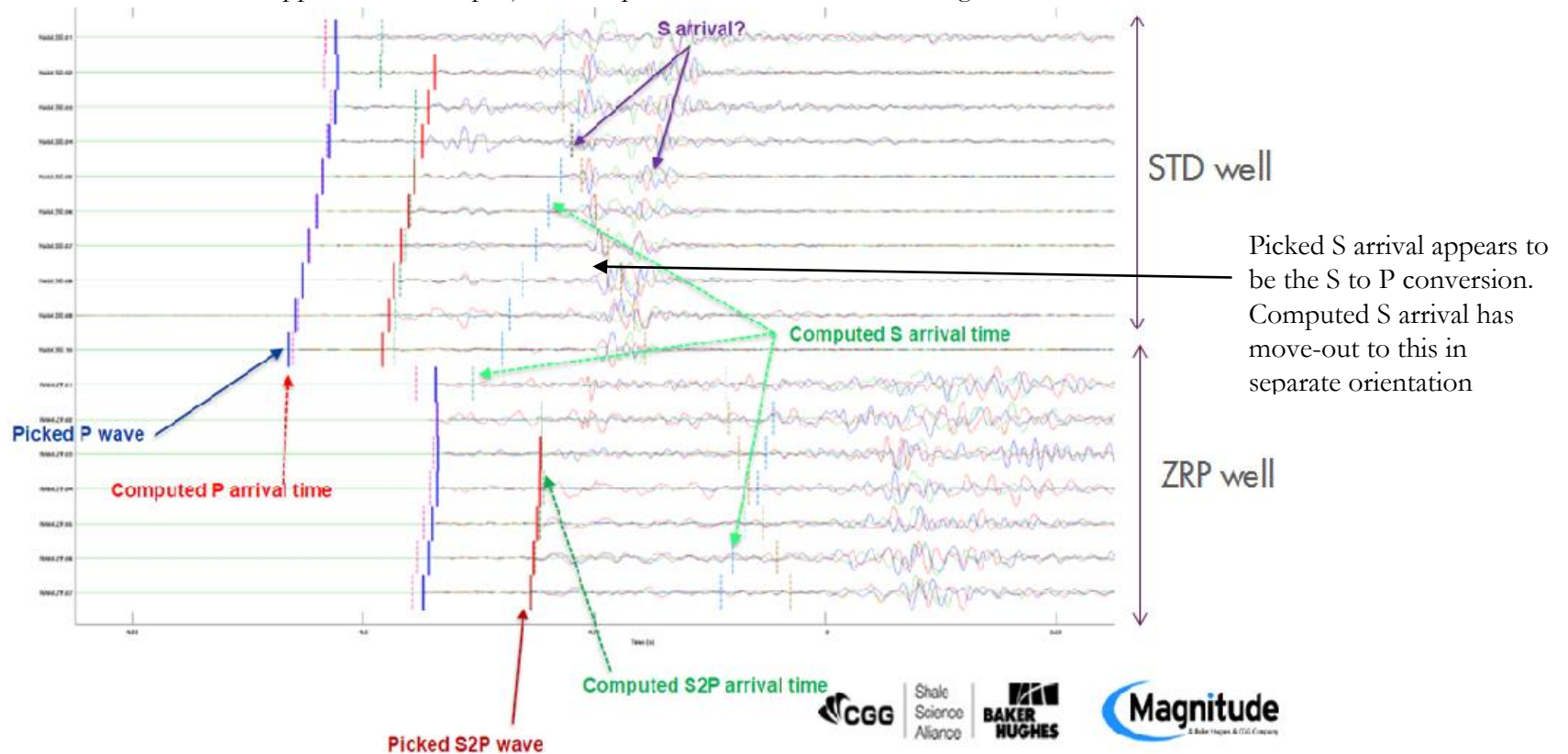
A1.3.1. Example interpreted seismograms

These images show example seismogram interpretations provided by the microseismic processing service company Magnitude. The three-component seismogram response from both the Stedum and Zeerijp well geophones arrays are shown. Magnitudes ray tracing software functioned on picking on the first break (in this case headwaves) and the S-wave direct arrival.

22/03/14 15:10:08

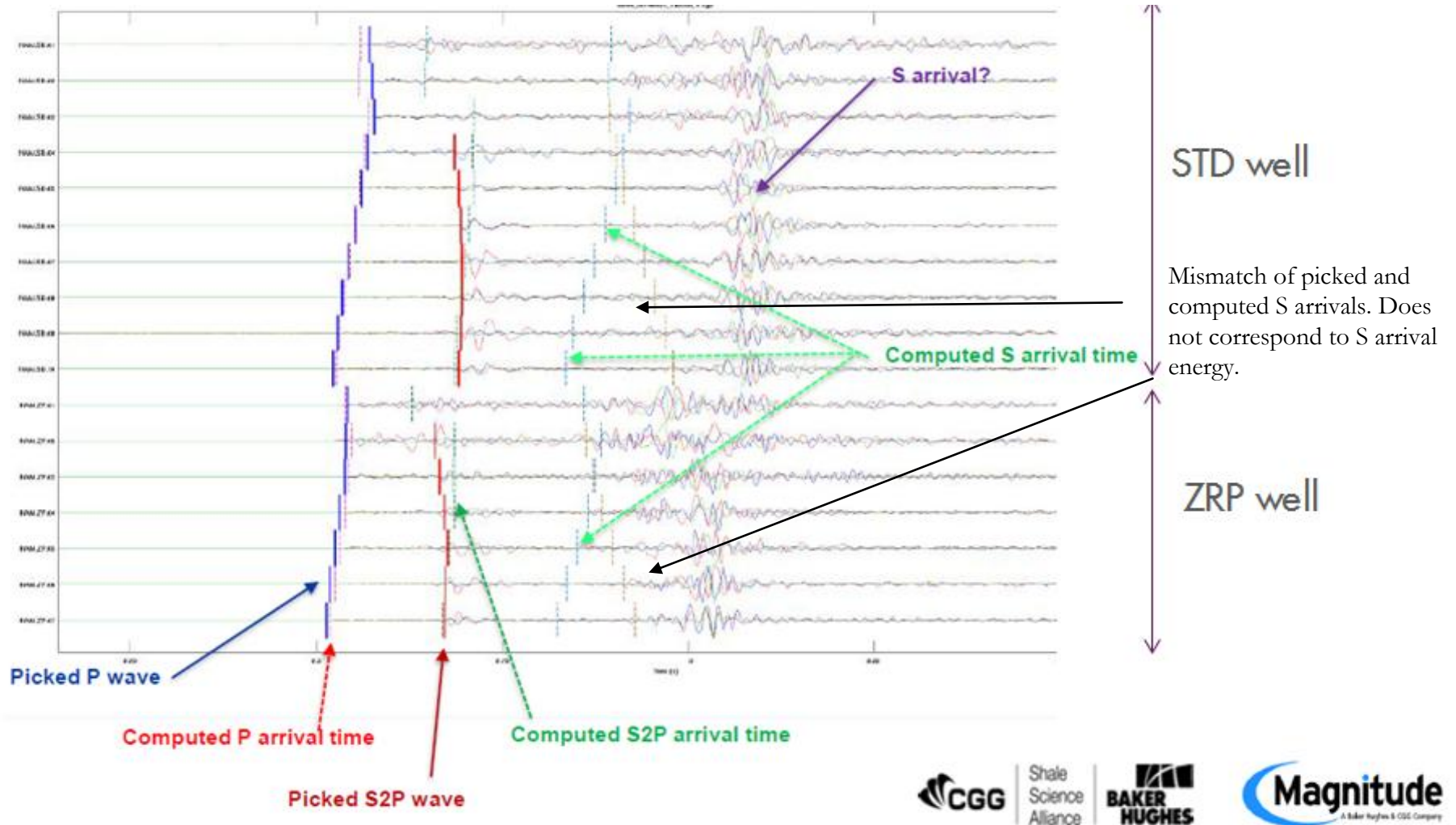
First it appears that Magnitude have wrongly identified the P-S conversion as the direct S arrival in their S arrival picking. The computed best fit S arrival has a move-out orientated in the opposite directed to the picked S arrival. The interpretation of the S-P conversions occurring at the base of the reservoir appears questionable. Given that Magnitude located the event at a depth of 4619m, it would be unlikely that there would only be a short time lag between the first arrival and the converted S wave, given the propagation distance required for the S wave to reach this layer interface for the mode conversion to occur. The finite difference modelling also did not indicate that an S to P conversion could occur at this point in time after the first arrival. See 22/03/14 15:10:08 in the appendix for this projects interpretation of this event seismogram.

A1.3.2.



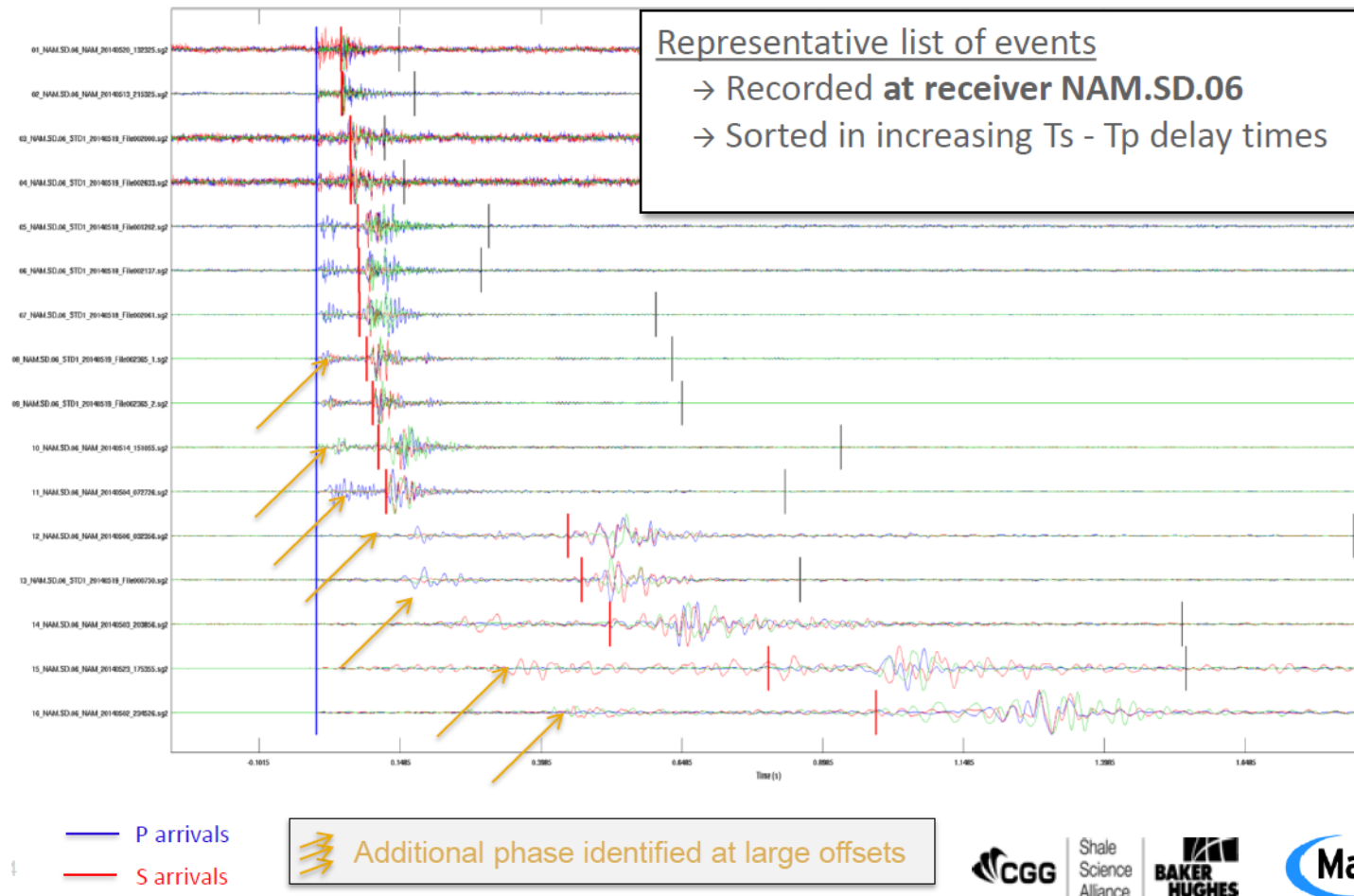
25/03/14 13:20:56

It is worth noting from this image that the move-out on the picked S and P arrivals do not appear to match. The picked S wave appears to correspond to the P-S conversion. The computed 'best fit' S wave arrival appears to match the same move-out slope of the P-wave arrival, however, this does not correspond to the arrival of S-wave energy. Again the interpretation of the S to P conversion also appears doubtful given the short time lag between the first P arrival and the S-P mode conversion given that this event was located by Magnitude at a depth of 4165m. The amplitude of this mode conversion also appears anomalously strong; this arrival was identified in this projects interpretation as the direct P arrival. See appendix A1.6.1 for full annotated seismogram interpretation.



A1.3.3. Effect of propagation distance on waveform

This image provided by the service company Magnitude shows the traces of several events recorded on geophone 6 of the Stedum well sorted by increase T_s - T_p times. This in effect shows how the waveform changes with increasing source receiver distance. Apart from the lower magnitude events with poorer signal to noise ratio, the events located at a short source-receiver spacing have fairly defined P arrivals, in which the first arrival that they have identified is the direct P wave. At larger source-receiver spacing's they have identified the head wave as the first arrival. The 'additional phase identified' appears to be a direct P wave, instead of a mode conversion. There appears to be significant noise preceding the s wave arrival; this could be a mixture of the P wave coda in additions to mode conversions and reflections. In the bottom two events at the larger source-receiver distance, it could be interpreted that the S arrival occurs at a later stage than that identified, as P-S conversions could have been incorrectly interpreted as a direct arrival.



A1.3.4. Magnitudes event depths

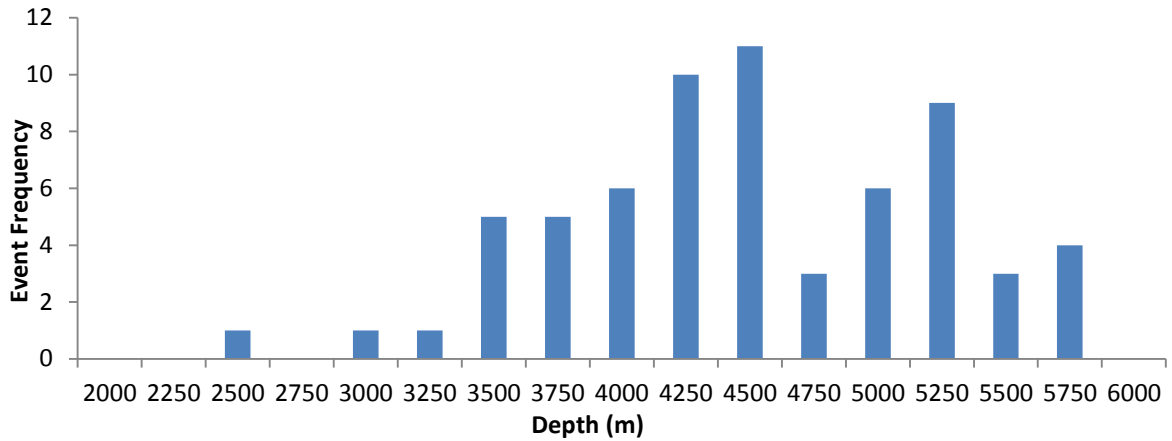


Figure 24: shows a histogram of the estimated event depths located by Magnitude with an estimated magnitude above 0.

A1.3.5. Gutenberg-Richter plot

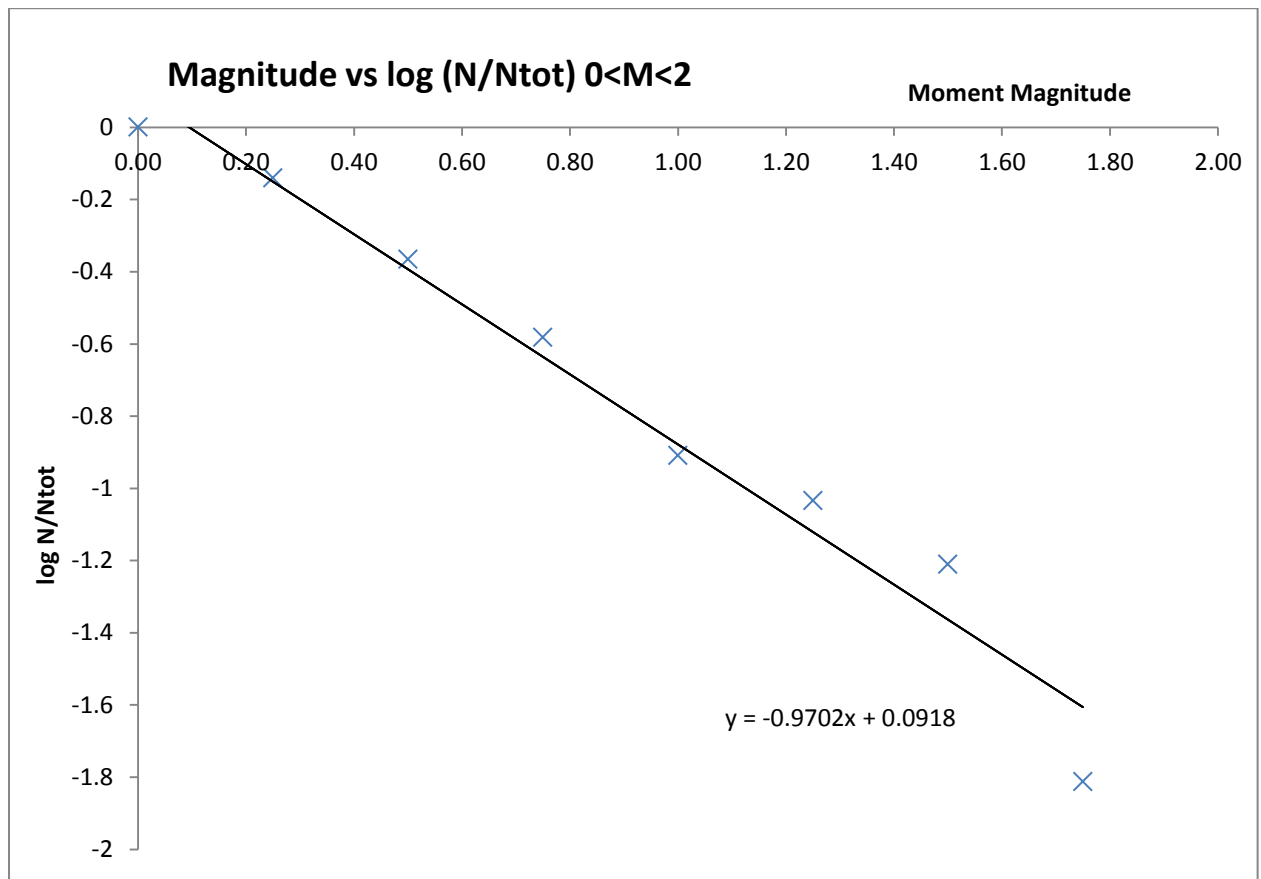
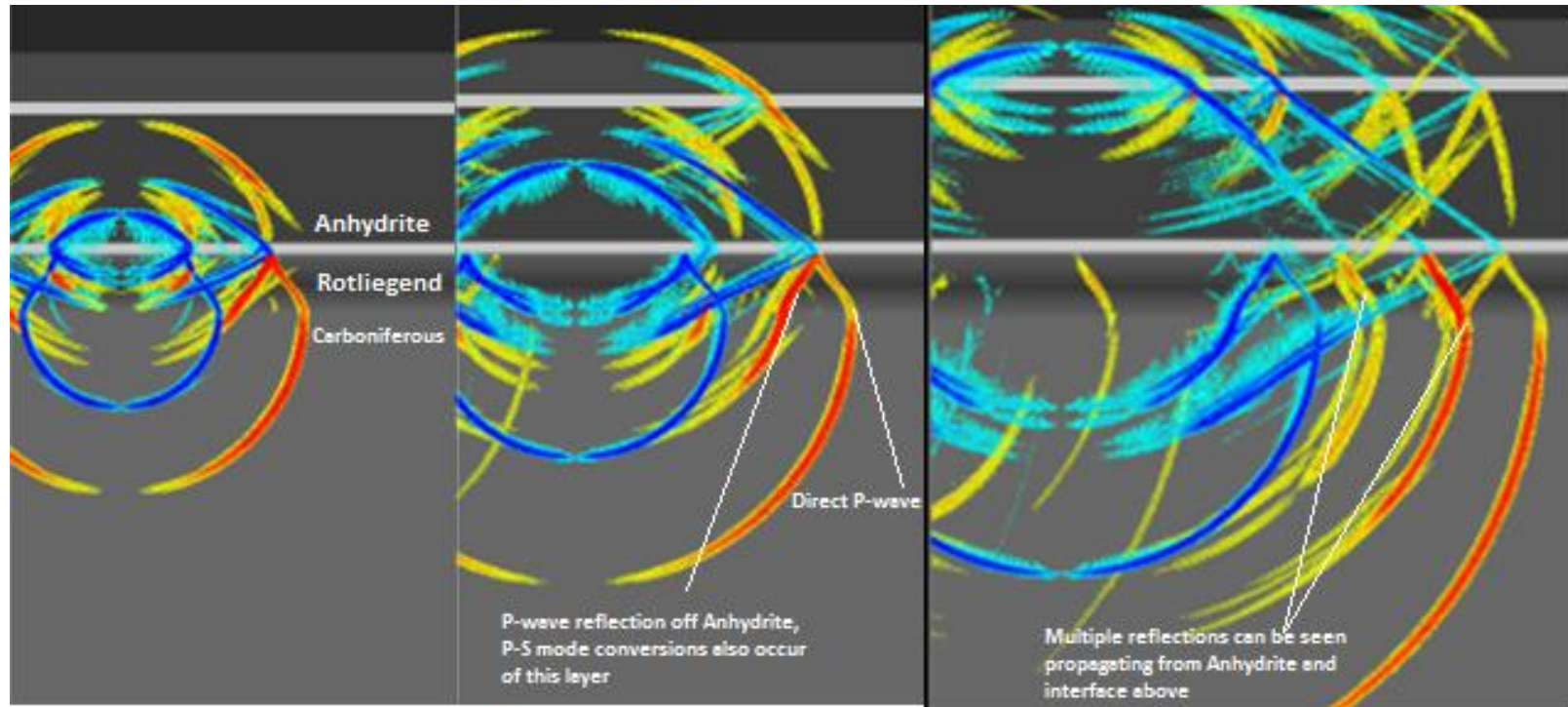


Figure 25 Image shows a Gutenberg-Richter plot of the events with a magnitude greater than 0. Magnitude was plotted against the logarithm of the fraction of the total events with a magnitude greater than this value. This produced a 'b' value of 0.97. This figure was produced using the moment magnitudes quoted by the service company Magnitude.

A1.4. Further finite difference modelling analysis

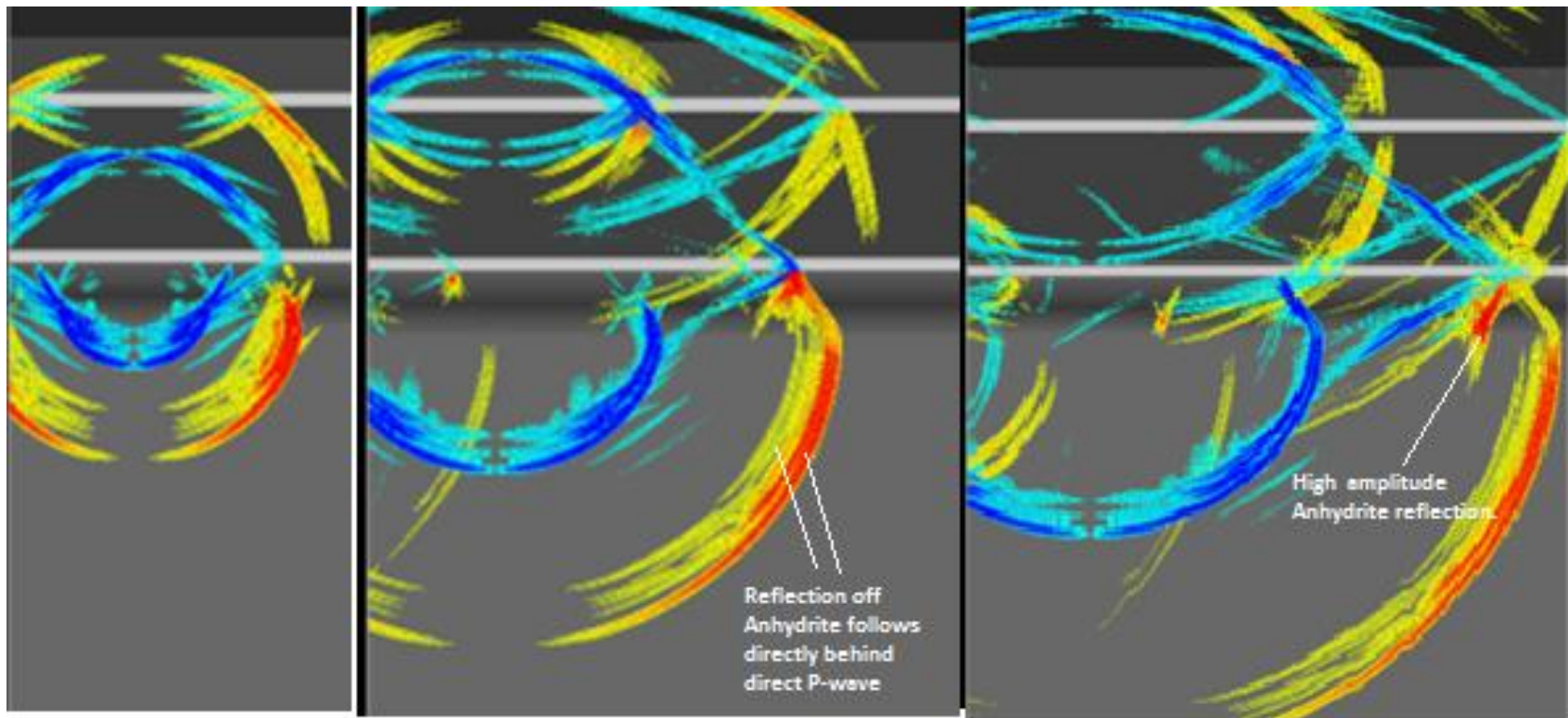
A1.4.1. Source at 3000m



An event was modelled at a depth of 3000m, which lies 30m above the reservoir- carboniferous interface and the character of the waveform observed appears to differ. At longer offsets three distinct P-arrivals can be observed. Following behind the direct arrival a high amplitude reflection appears off the Anhydrite-Rotliegend interface. The amplitude off this signal is higher than the direct arrival at the depth range of the reservoir, where the receiver array is stationed. A third lower amplitude P-wave reflection is observed off the Anhydrite-Zechstein interface. P-S conversion cuts across with move-out in a separate direction.

Event 22/03/14 13:10:12 (see event 22/03/14 13:10:12 in appendix for interpretation), located at a depth of 3057m by the location algorithm, appears to have a seismogram that matches this wave propagation predicted by the modelling at this depth. A defined reflection in the seismogram appears after the direct arrival, this also appears to have higher amplitude than the direct arrival.

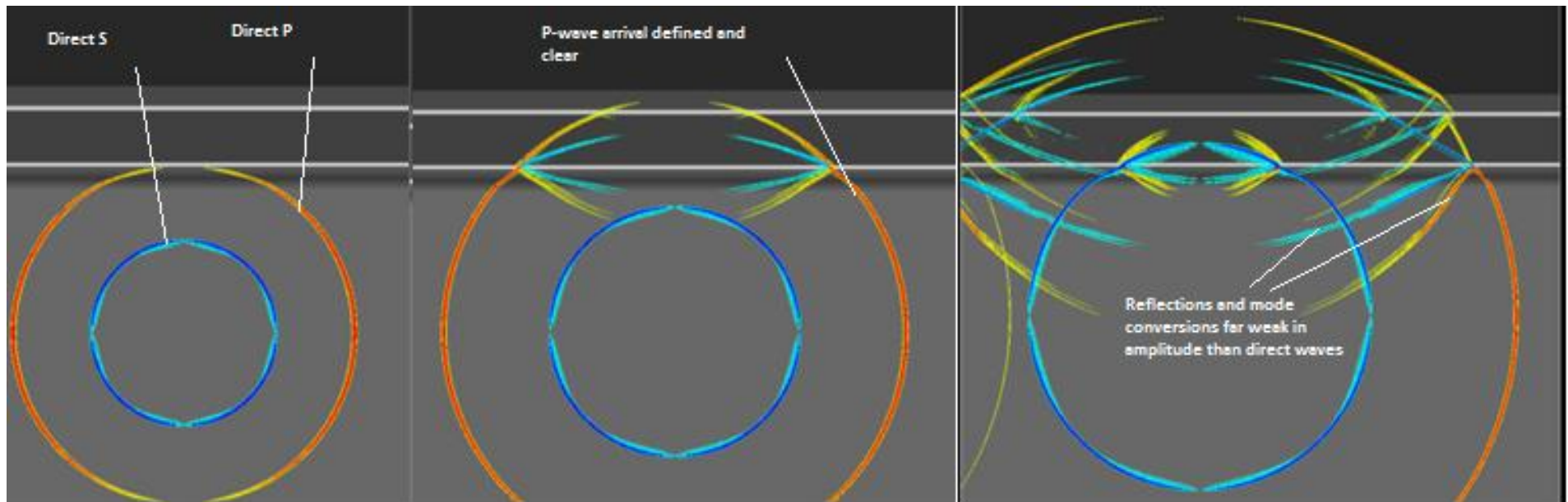
A1.4.2. Source at 2800m



These images show the propagation of the wave of an event placed in the reservoir 30m below the Anhydrite. The arrival reflected off the Anhydrite appears to be far higher in Amplitude than the direct P arrival. As the source is close the high velocity Anhydrite, the incident angle of the wave would result in the P wave being critically refracted down. Consequently, a large proportion of the seismic energy is reflected off the Anhydrite, giving it a higher amplitude than the direct arrival.

It is also interesting to note that the move-out of the wave may give the appearance that the event is coming from the base of the reservoir as the wave propagates at a higher velocity in the Carboniferous layer. This was however generally not observed to be the case for the traces with events located near the top of the reservoir.

A1.4.3. Source at 4600m



The following images show the modelled waveform propagation of an event occurring at 4600m, at the approximate mean depth of the events located by Magnitude which have a magnitude of above 0. As can be observed from the plots, simpler waveforms are expected to be observed than events occurring in the reservoir. A clear P and S separation is also expected in the seismograms. Some reflections and mode conversions are observed as the wave hits the Anhydrite interface. However, these appear to be lower in amplitude than the expected reflected waves seen for sources placed inside the reservoir. This is largely due to the incidence angle of the wave on the Anhydrite, as critical refraction may only occur at large offsets.

A1.5. Layer discrimination from waveform character

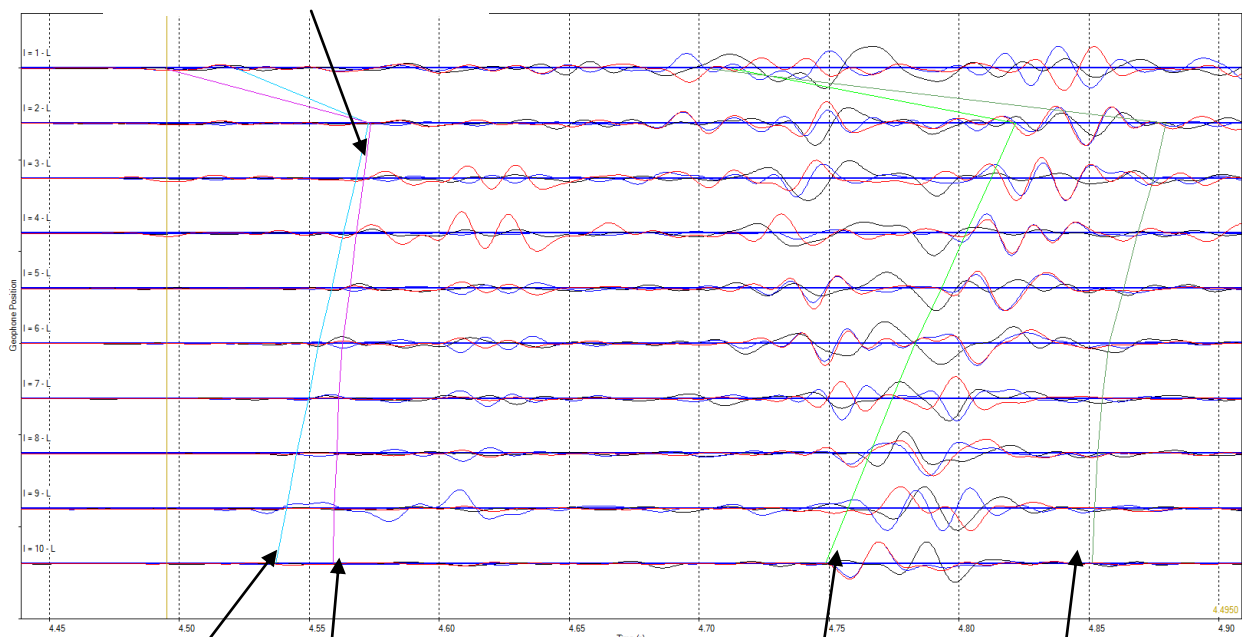
Event 22/03/14 15:10:08 waveform move-out analysis

This event highlights the difference in the move-out and P and S separation for an event placed above or below a layer interface. This illustrates how the pattern of arrivals provides a good discriminator for the origin layer of the event, however, depth in the layer itself is relatively imprecise. This shows the seismogram view of the event 22/03 at 15:10:08 seen from the Stedum well array. The epicentre location of the event was determined to be $N = 595718$, $E = 243416$, $D = 3057$ which is 27m below the carboniferous interface of 3030m and is one of the few events located outside of the reservoir.

The example below shows the effect of forward modelling the P and S direct arrivals based on a source with the same epicentre location, but with a depth of 3029m, which is in the reservoir 1m above the Rotliegend-Carboniferous interface. The dark purple and dark green lines show these theoretical move-out curves. The P and S best-fit lines (shown in light blue and light green respectively) based on the determined location using the grid-search algorithm, are also overlain on the seismogram for comparison. The program provides the forward modelled P-S separation curves but not the specific arrival times, (the curve is arbitrarily overlain over the best-fit curve on the p-arrival time for the second geophone for the best visual illustration).

As can be observed, the p and s arrival separation and move-out for a source placed inside the reservoir does not match the observed seismogram arrivals.

Best fit and forward
modeled curves overlain at
this point



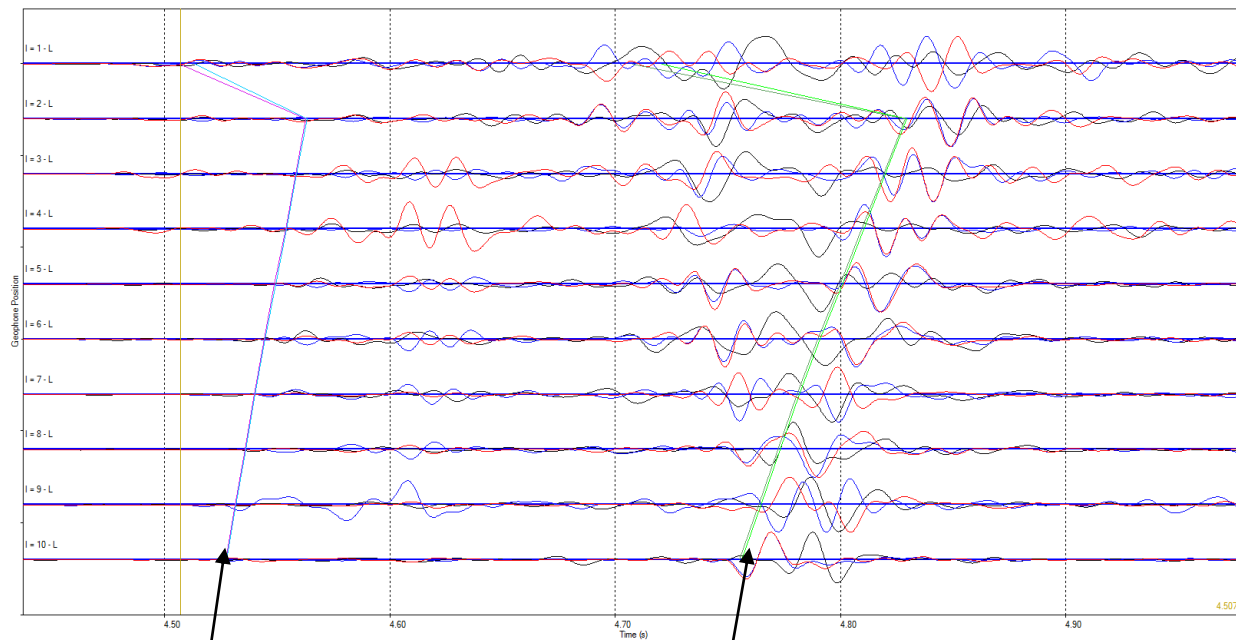
Best fit P-arrival

Theoretical arrival for event with same epicentral location but with depth in Reservoir at 3029m. Move-out curve does not fit P arrivals.

Best fit S-arrival

Theoretical S-arrival for depth of 3029m. P-S separation far too large for seismogram.

In this case the theoretical overlay is replaced by a source with again the same epicentre location, but with a depth of 3031m, 1m below the Rotliegend-Carboniferous interface. The best fit P and S arrival times based on the depth of 3057m determined by the location algorithm are also overlain on the seismogram. It is worth noting that these arrival times almost exactly coincide. Whilst changing the source location above or below the reservoir by 2m has a large effect on the arrival times (based on modelling the event as a point source), changing the event position by 27m inside the model layer had an almost indistinguishable effect on the P and S arrival times.



Forward modelled arrival time for event with same epicentre location but with depth of 3031m. Best fit curve for location algorithm generated P arrival times directly overlies this line almost exactly.

Forward modelled arrival time for event with same epicentre location but with depth of 3031m. Best fit curve for location algorithm generated S arrival times directly overlies this line almost exactly.

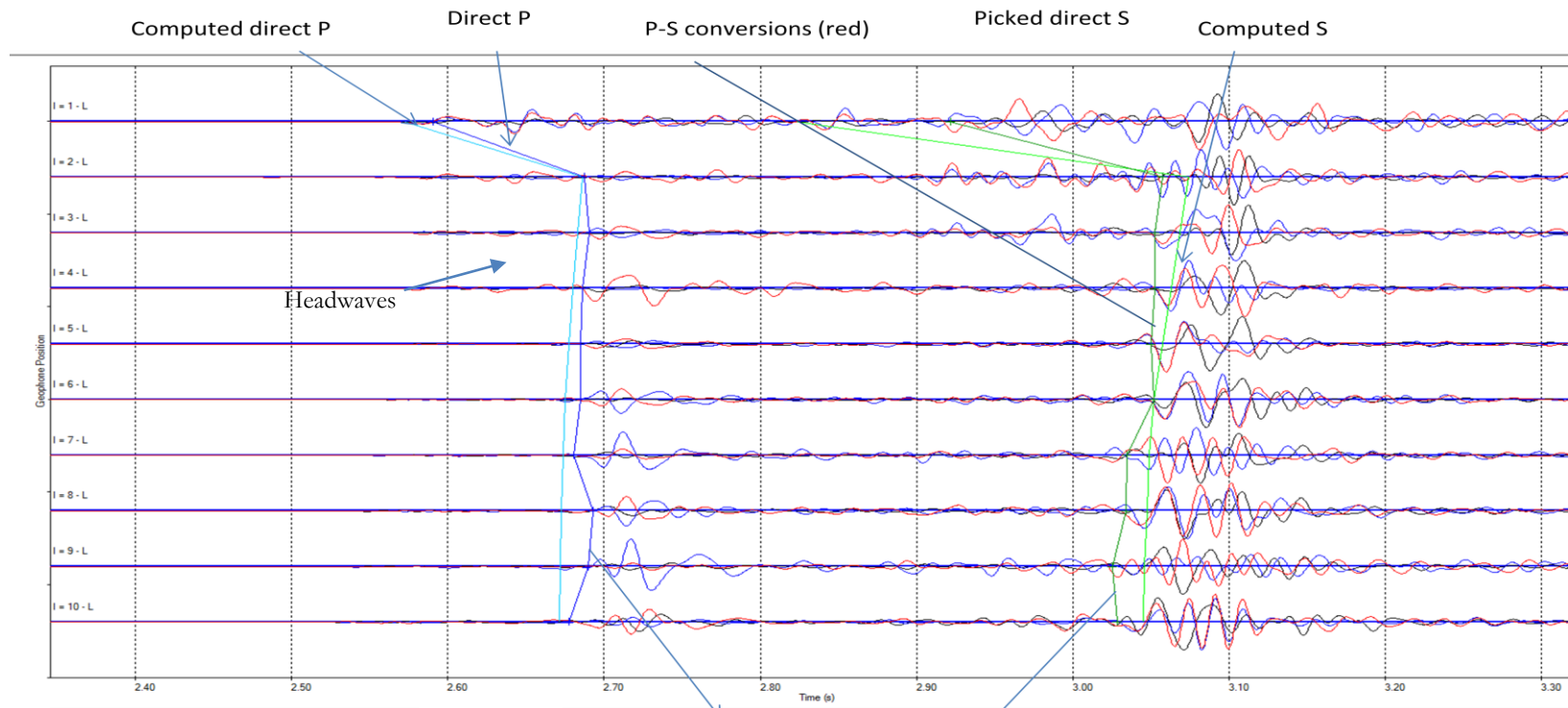
The same event again was forward modelled for an event position at 3357m, 300 m below the estimated source position; the difference in the arrival times produced from this was also marginal and well within the uncertainty of arrival picking by eye. From this, it can be concluded with relative confidence that the source position is likely to be in the Carboniferous. However, the true hypocenter location inside this layer is relatively uncertain as moderate changes in depth position result in relatively minor arrival time differences.

A1.6. Example trace interpretation

The following images show some example traces interpreted. The dark blue and light blue lines correspond to the picked and computed best fit P-wave direct arrivals, the Dark and light green lines correspond to the picked and computed best fit S-wave direct arrivals. The blue, red and black lines in the seismograms themselves correspond to the trace amplitude response of the x,y and z components of the geophones

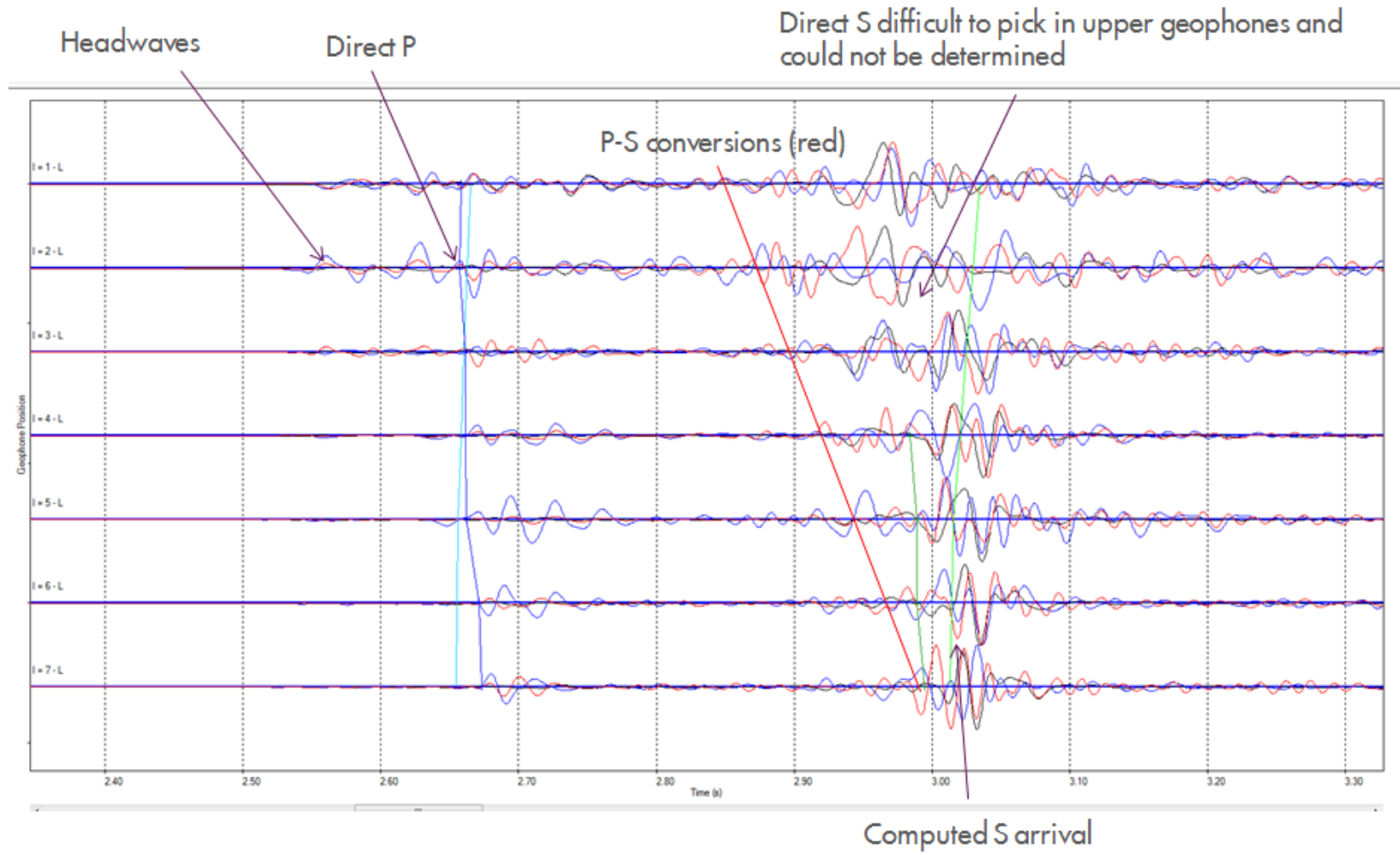
A1.6.1. Event 25/04/14 13:20:56

Stedum well



Move-out and P-S separation shows the event must have originated from the reservoir although depth in this layer is uncertain.

Zeerijp well



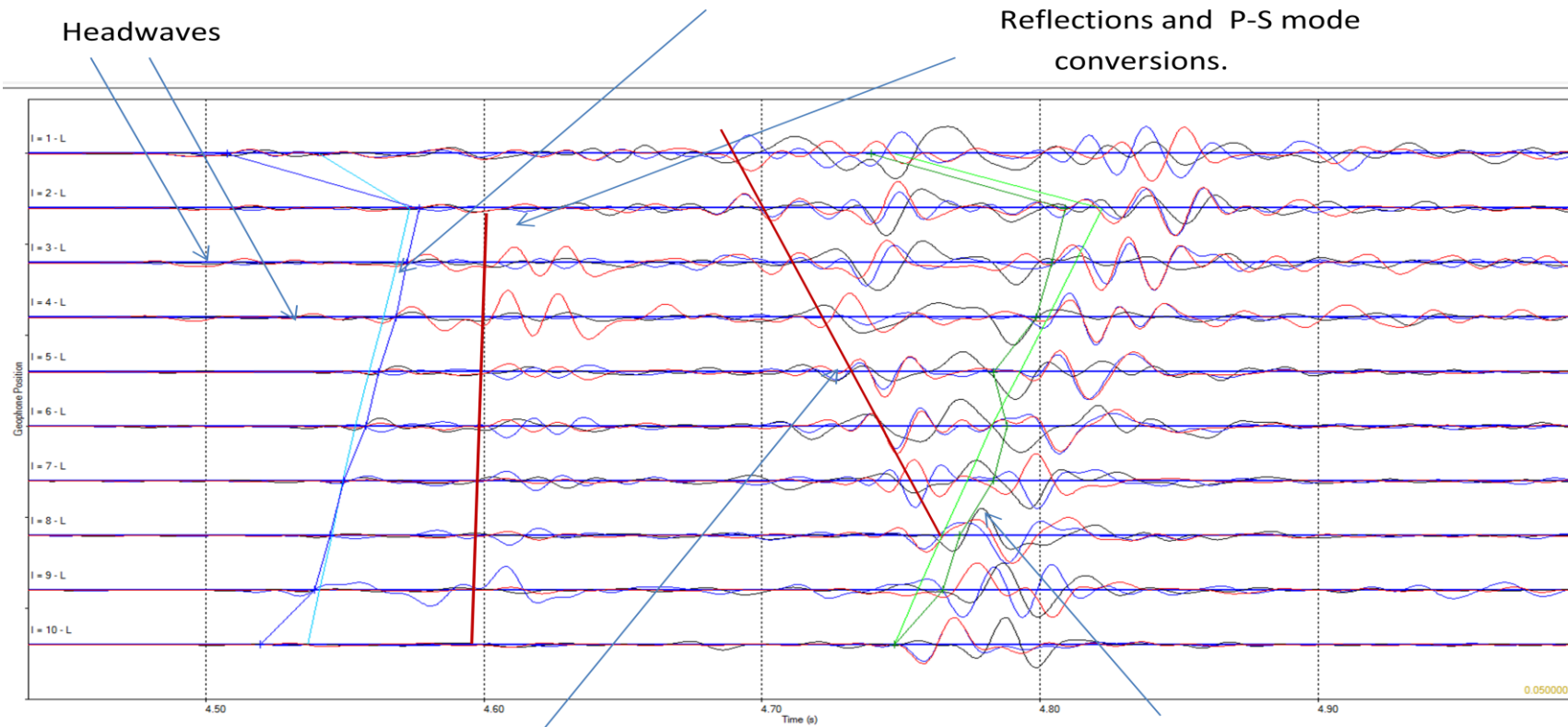
A1.6.2. Event 22/03/14

Stedum well

The red line indicates a possible arrival. However,

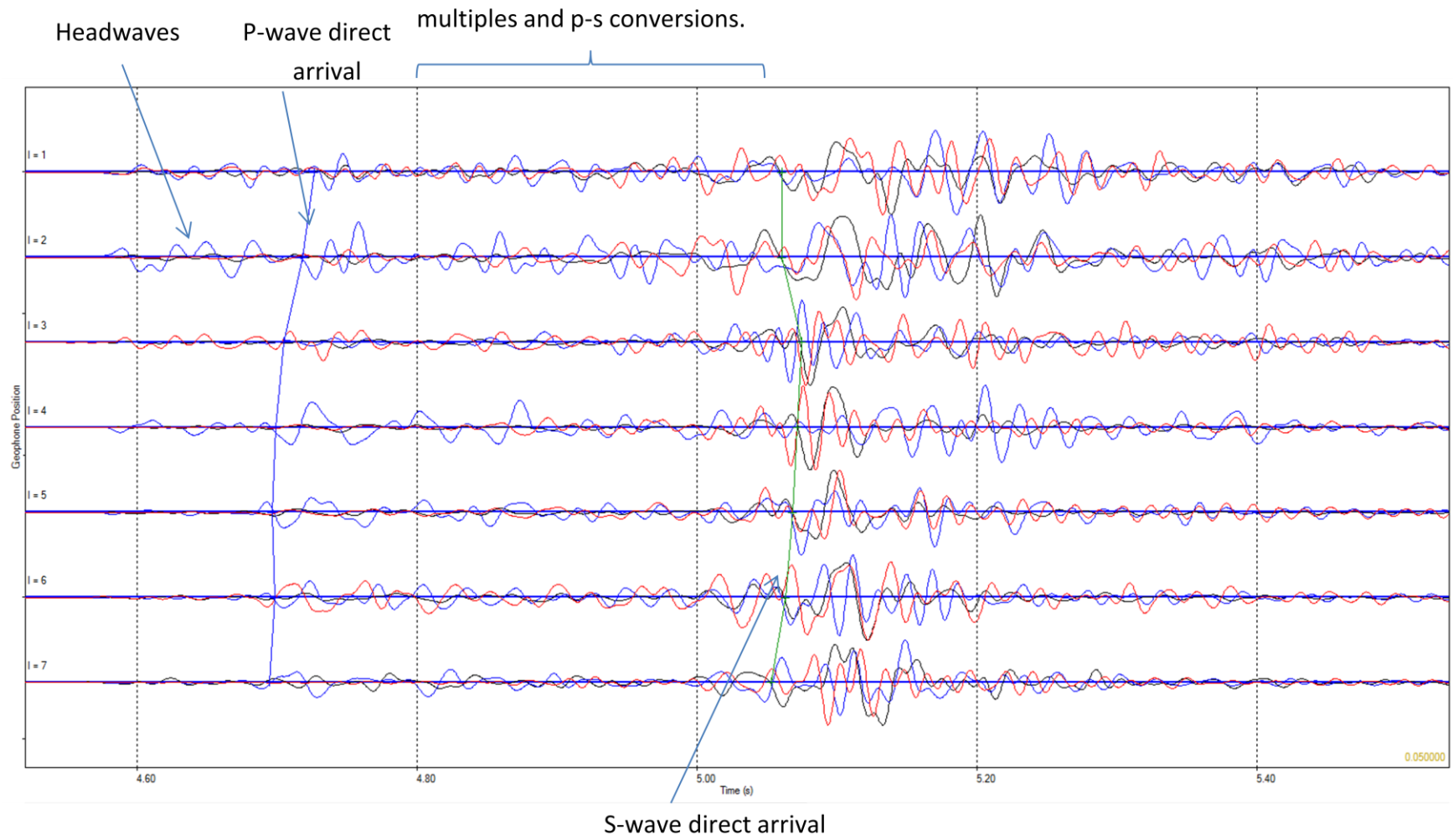
Picked Direct arrival

use of forward modelling indicated that this was not the case

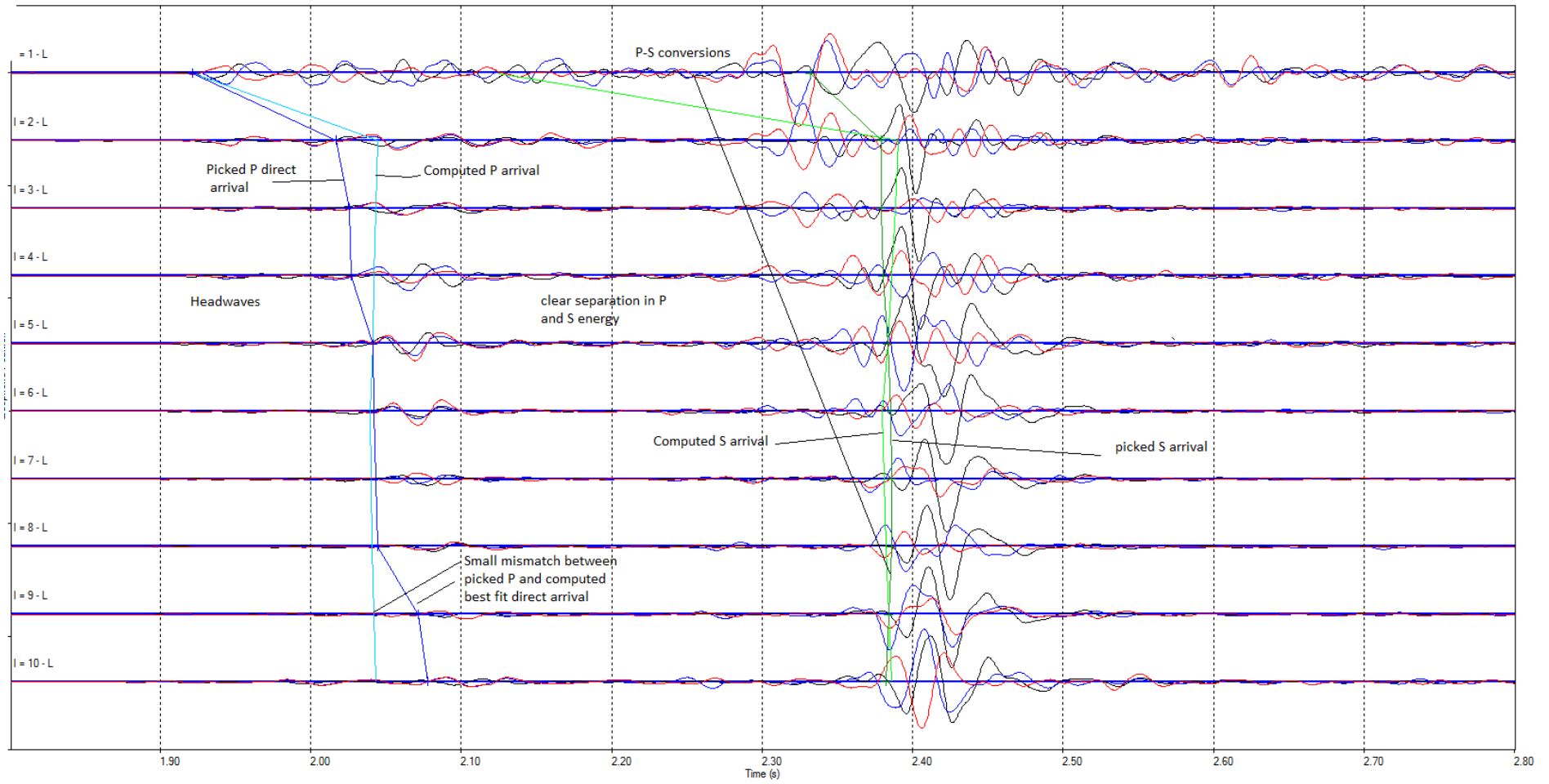


P-S conversions – can be identified from the moveout as direction is opposite to incoming p-wave and suggests reflection off Rotliegend-Anhydrite boundary

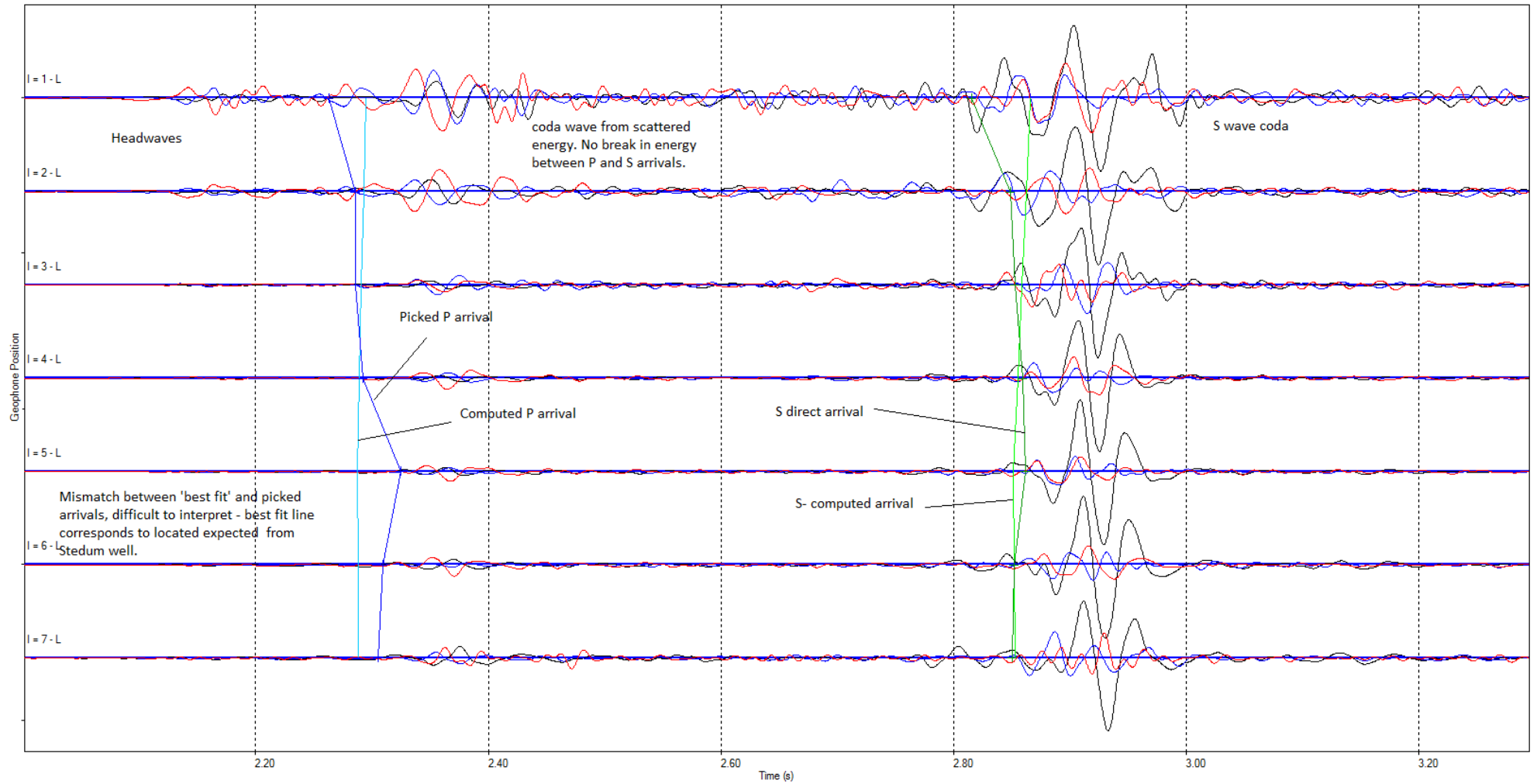
Zeerijp well



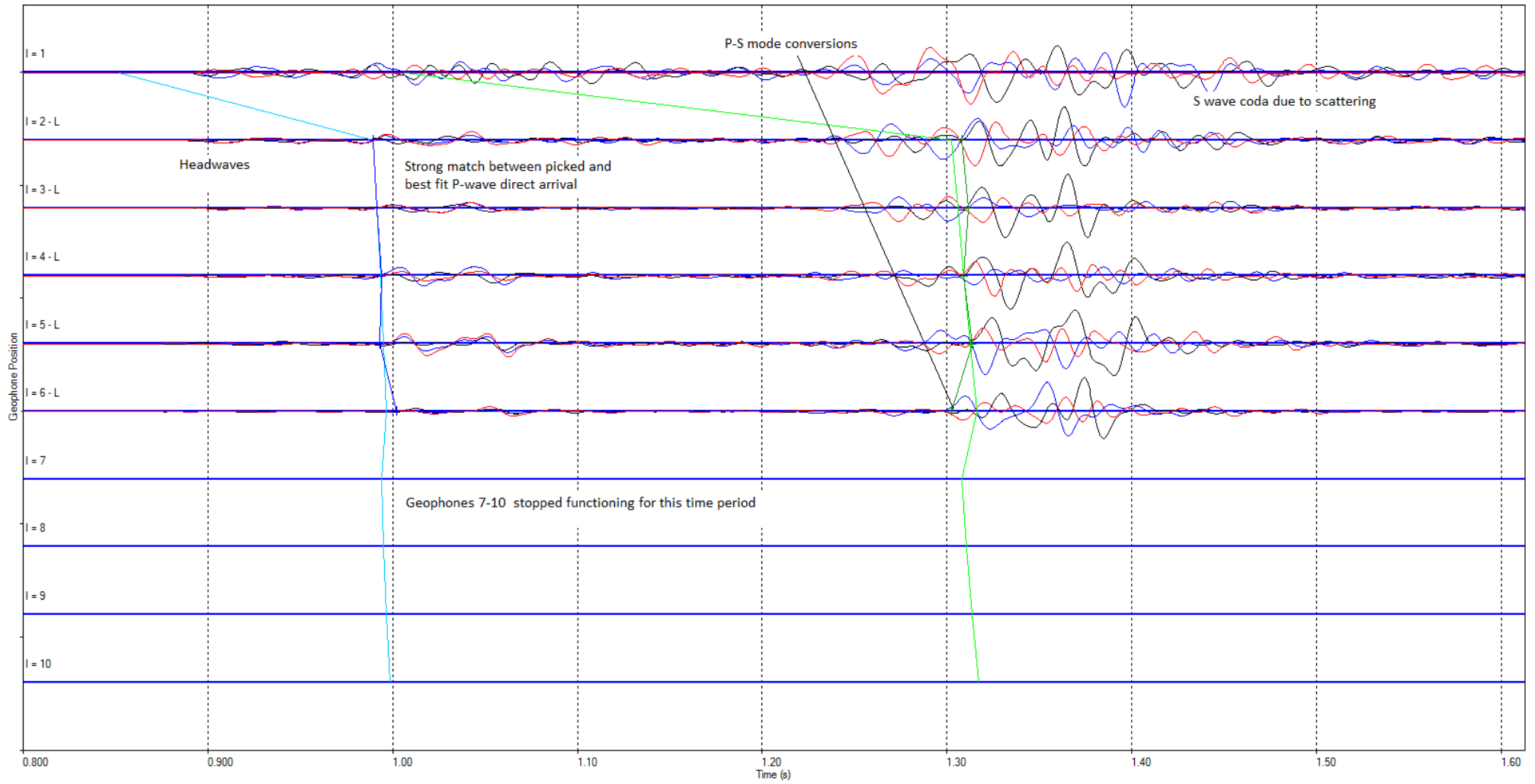
A1.6.3. Event 23/03/14 02:23:55 Stedum Well



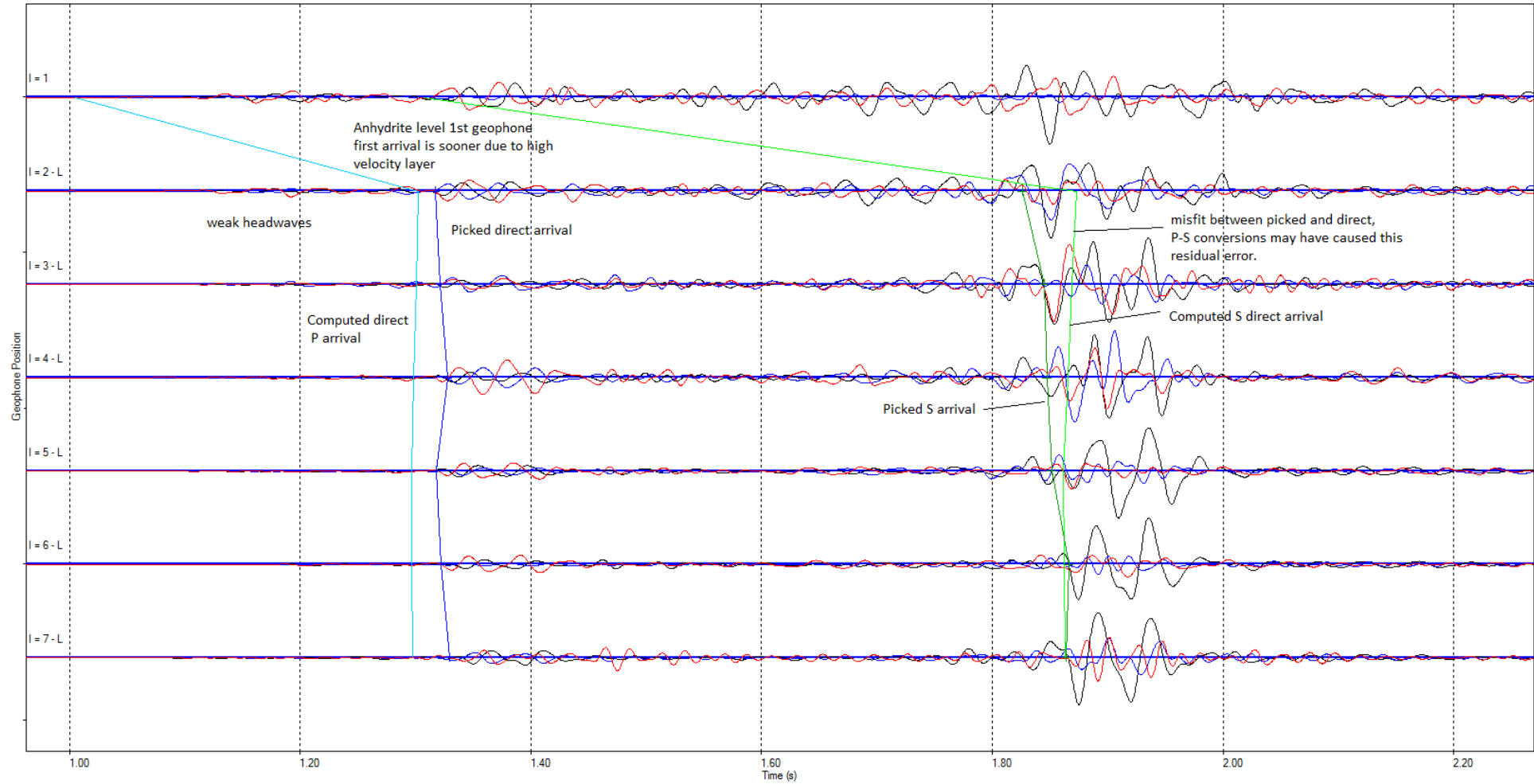
Event 23/03/14 02:23:55 Stedum Well



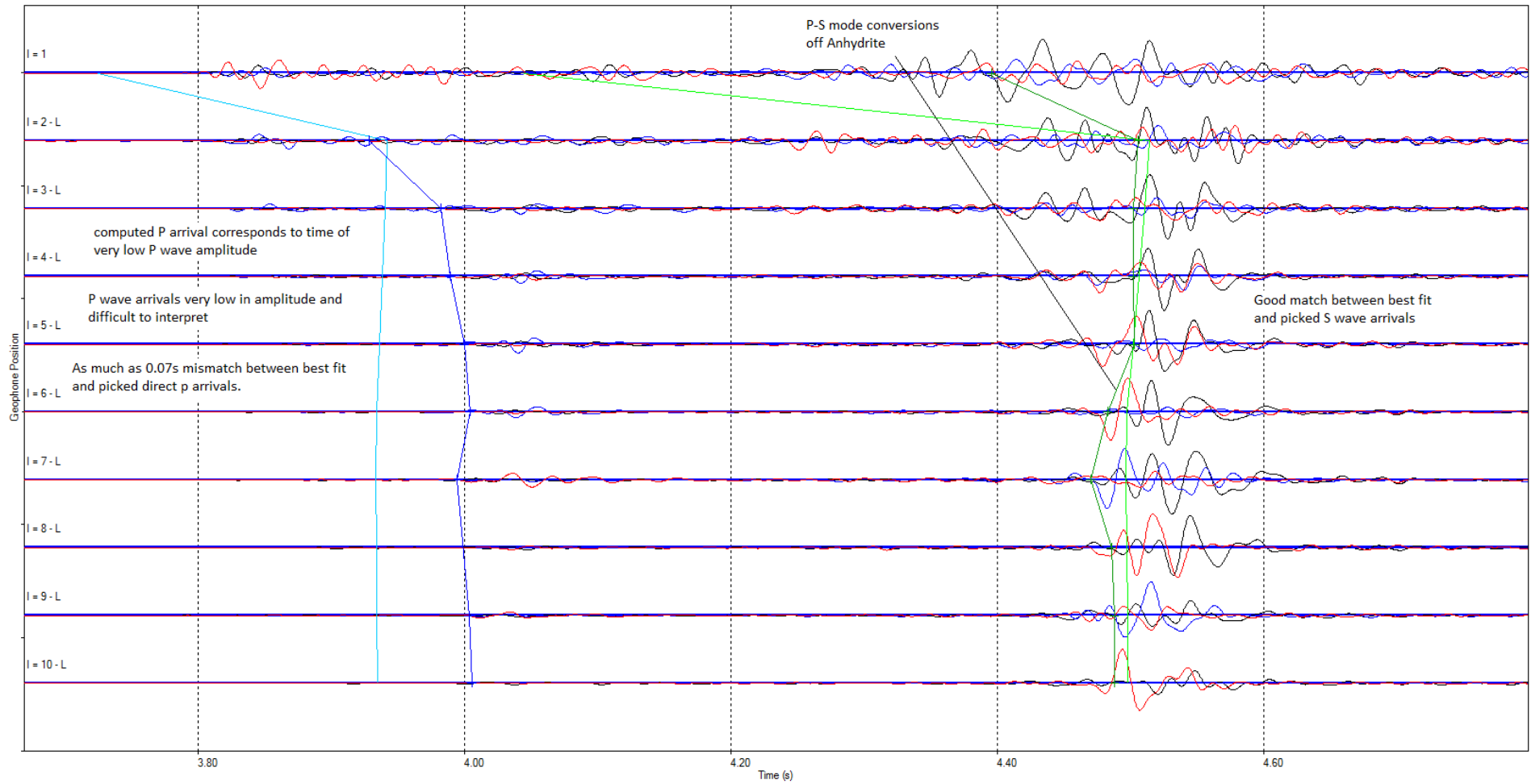
A1.6.4. Event 15/04/14 09:43:24 Stedum Well



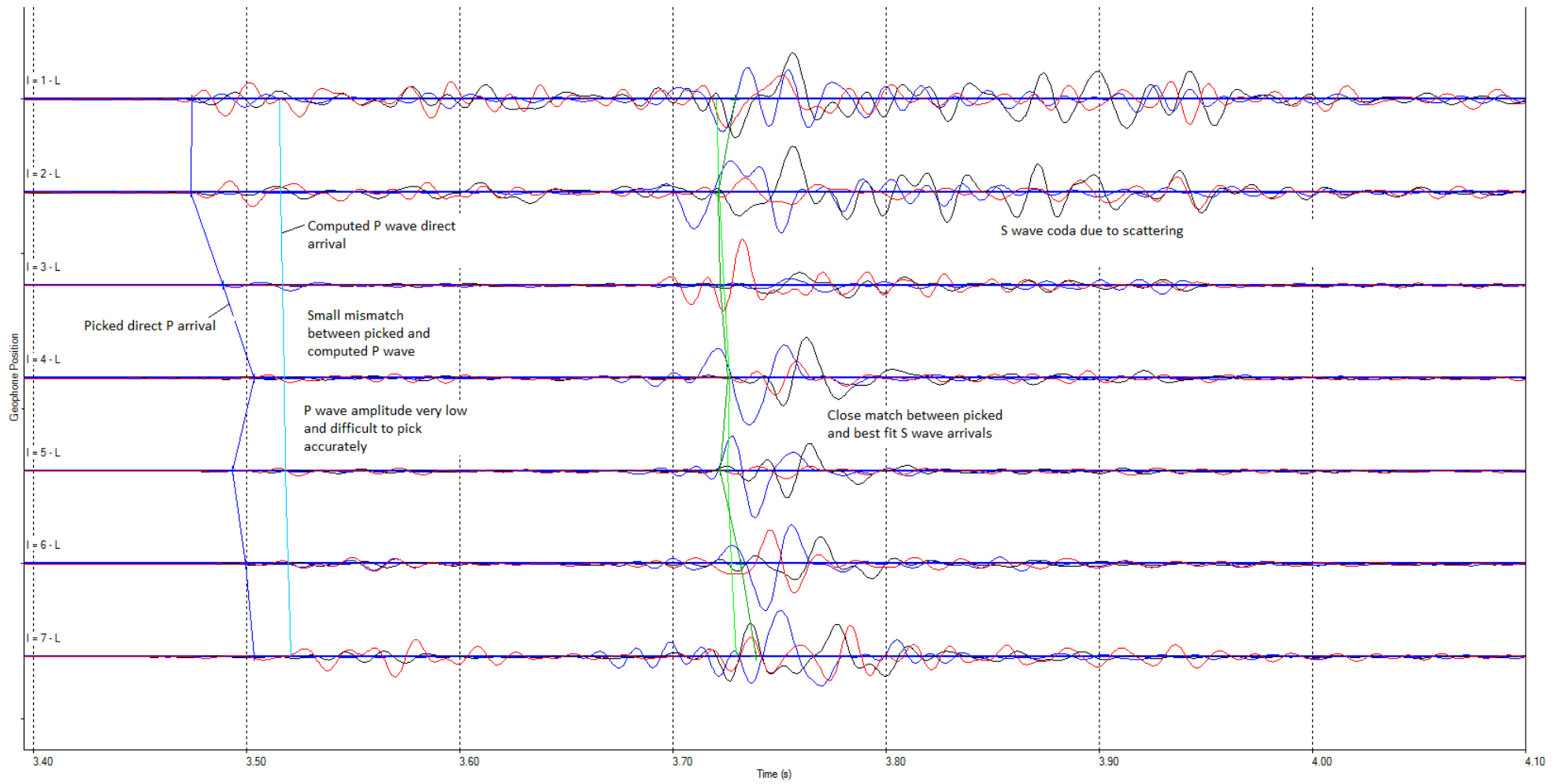
Event 15/04/14 09:43:24 Zeerijp Well



A1.6.5. Event 01/04/14 20:08:56 Stedum well



Event 01/04/14 20:08:56 Zeerijp well



A1.7. Velocity model

A1.7.1. Sonic logs

All depths shown in this report are based on the true vertical depth below sea level.

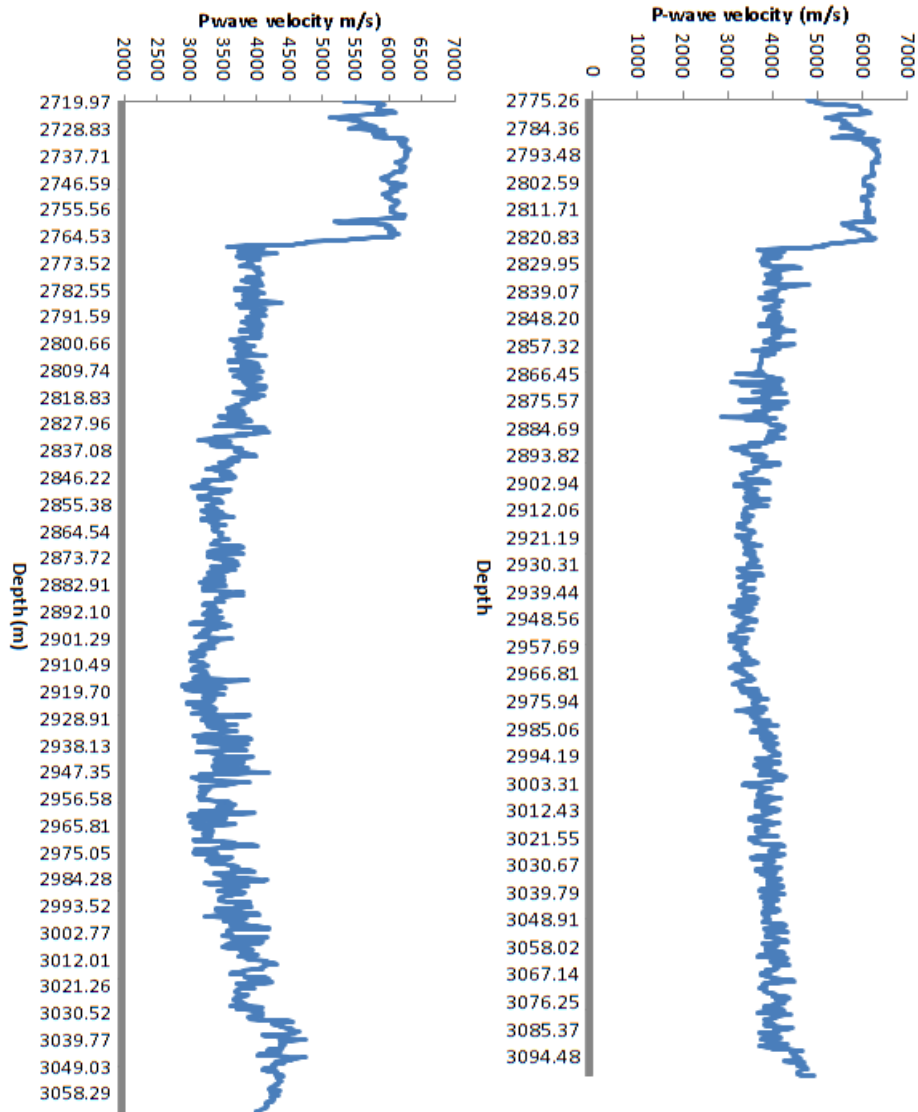


Figure 27 shows the abbreviated P wave sonic log from the Stedum-1 well array covering depths from the top of the Basal Anhydrite to the base of the well in the Carboniferous

Figure 26 shows the P wave sonic log from the Zeerijp-1 well array covering depths from the top of the Basal Anhydrite to the base of the well in the Carboniferous

A1.7.2. InSite

The event theoretical travel times and event locations are determined from the velocity model. It was assumed that the lateral variations in the velocity were not sufficient to significantly affect the travel times and furthermore ray tracing in a 3 dimensional heterogeneous medium would have significantly increased the computational difficulty in ray-tracing. A one dimensional model was produced that assumed constant velocity layers.

The P and S wave velocities were calculated using sonic data from both the Stedum and Zeerijp wells. The velocity model provided based the layer velocities on this data. As the model split the subsurface into constant velocities, the velocities over each block were formed from an average.

Table 8 shows the velocities used in each layer in the velocity model used in InSite. The velocities for this model were provided by NAM.

Depth_Top	Vp	Vs	vp2vs	Depth_Base
0	3200	1966	1.63	1880
1880	4540	2482	1.83	2100
2100	6000	3415	1.76	2150
2150	4480	2444	1.83	2720
2720	6000	3415	1.76	2769
2769	3585	1870	1.92	2900
2900	3705	1945	1.90	3030
3030	4260	2303	1.85	5000

A1.7.3. Finite difference modelling

The finite difference modelling algorithm allowed linearly increasing velocities to be used in a given layer. This allowed the decrease in velocity towards the centre of the reservoir to be modelled in the ray propagation. The figure below shows the velocities used in the finite difference modelling using a plane layered model.

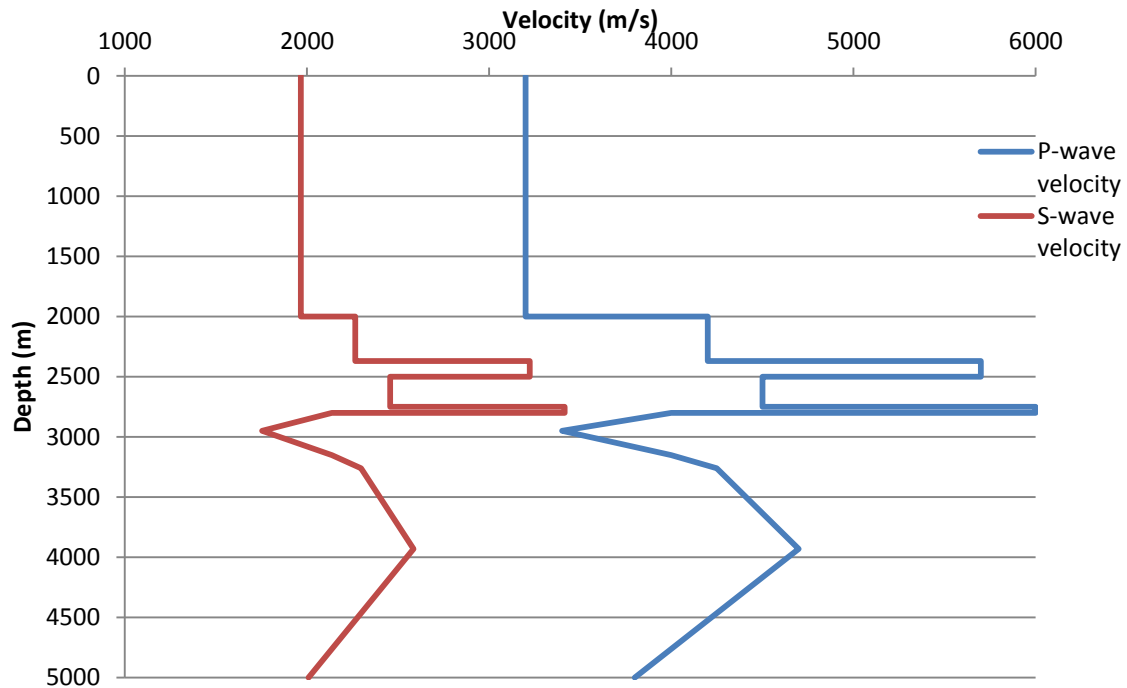
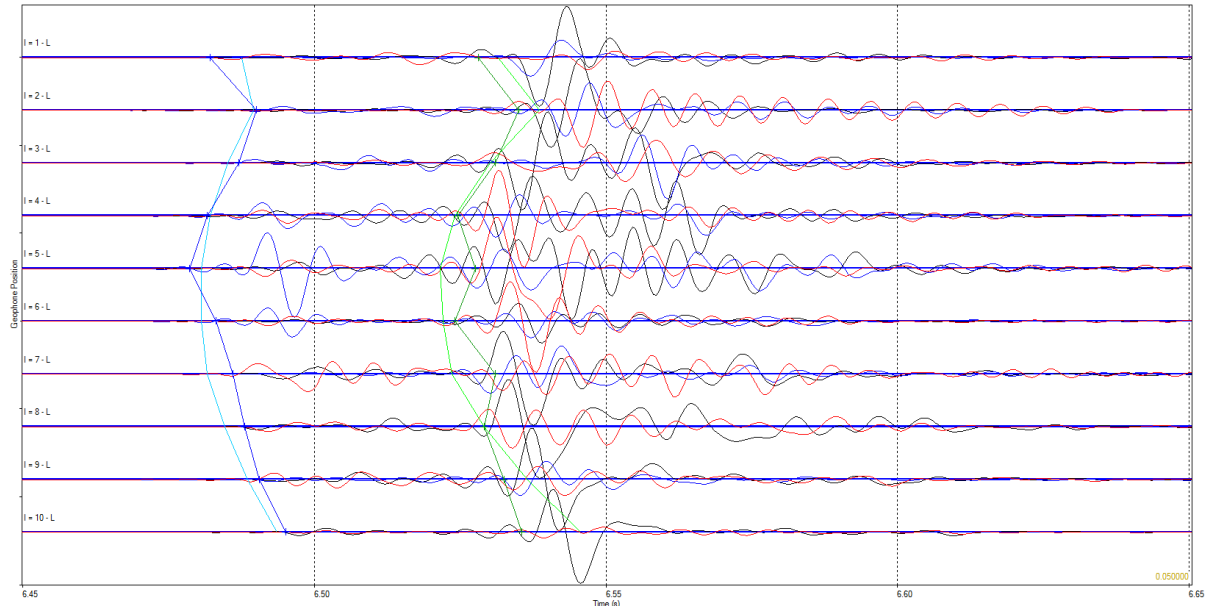


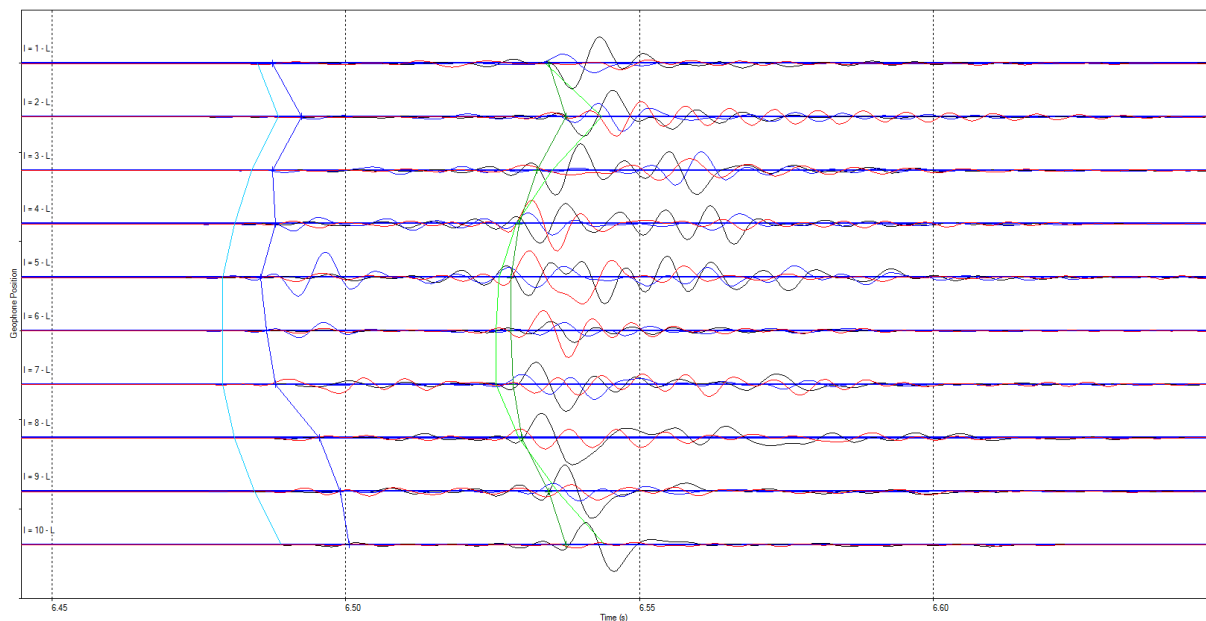
Figure 28 shows the velocities used in the finite difference modelling. A constant gradient was used in the velocity model.

A1.8. Analysis of event 09/04/14. Accuracy determination.

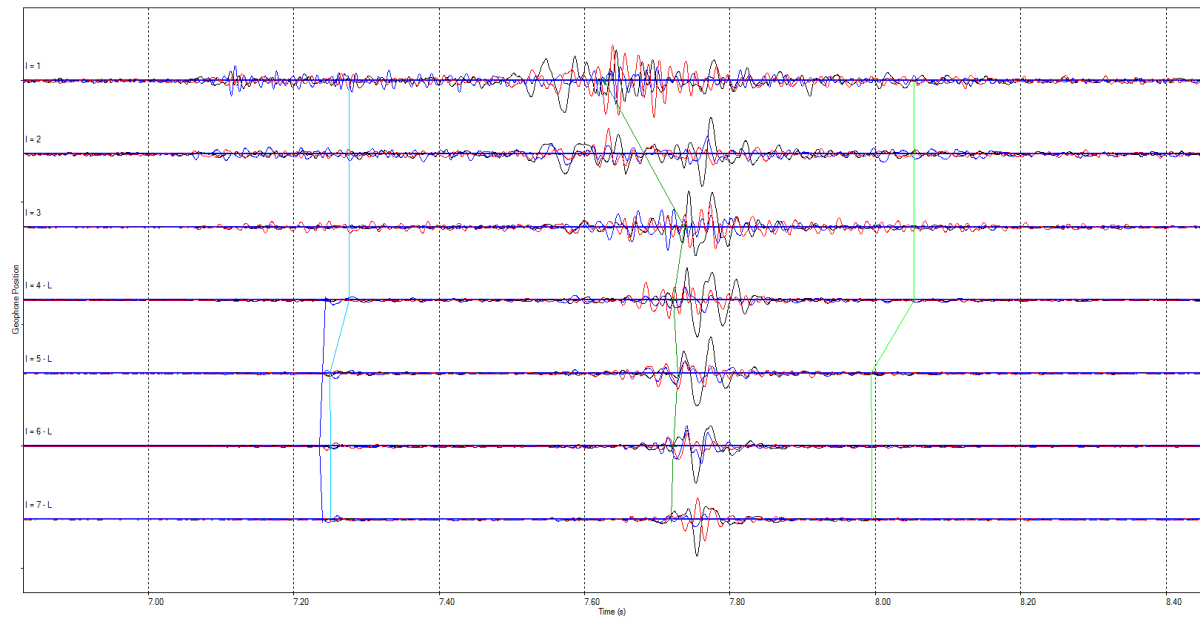
This event acted as a good quality check for the results. As the event was less than 300m from the furthest Stedum receiver it gave clear P and S arrivals with a defined move-out between receivers. The event was located from the Stedum well at an epicentre location 19m away from magnitudes value, and a hypocenter location 51m away. The figure below shows the direct arrival time P and S picks with the best fit line plotted.



The figure below shows the same seismogram with the 'best fit' determined by the arrival time picks of both the Stedum and Zeerijp wells. There is a clear misfit between the computed and picked arrival times.



The image below shows the seismograms from the Zeerijp well showing the P and S arrival times with computed using the arrival time P and S picks of both wells. The computed P arrivals appear to match the picked P arrivals with relatively accuracy. However, a large misfit can be seen between the computed and picked S wave arrivals.



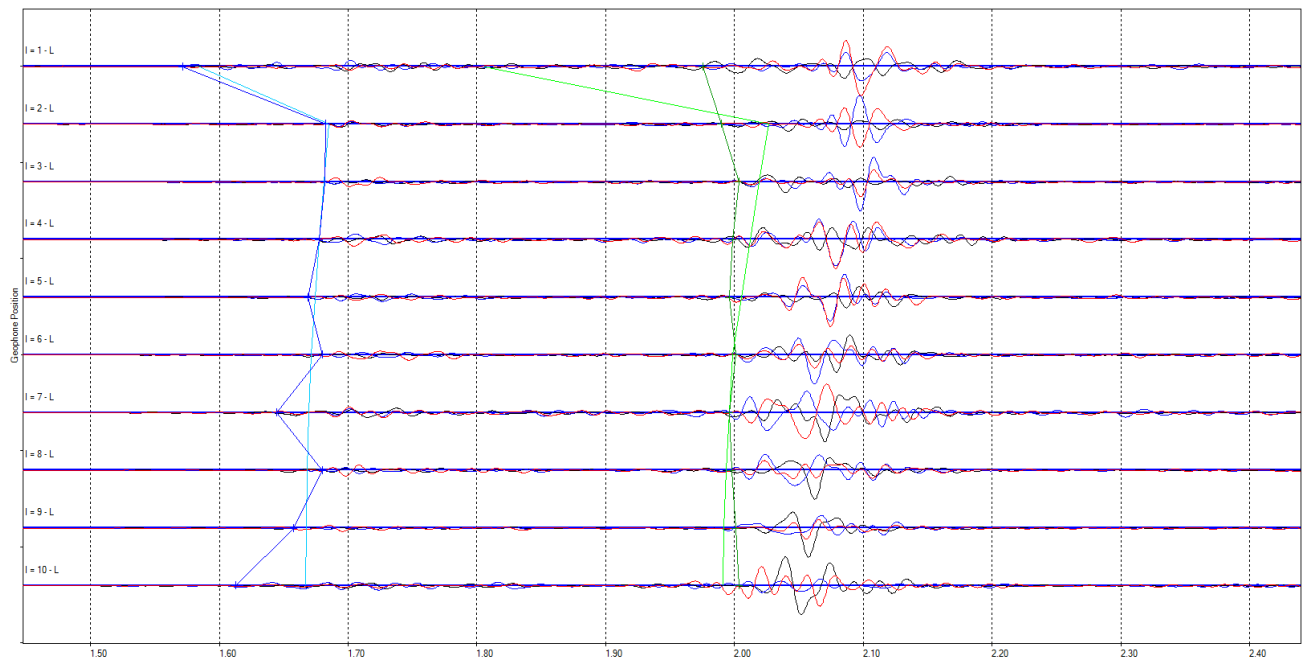
All the com located at same point except Stedum well, but both wells seem to correct large residual error on S wave possible effect of graben influencing velocities in upper 3 geophones.

A1.9. Trace Arrival time P and S picks

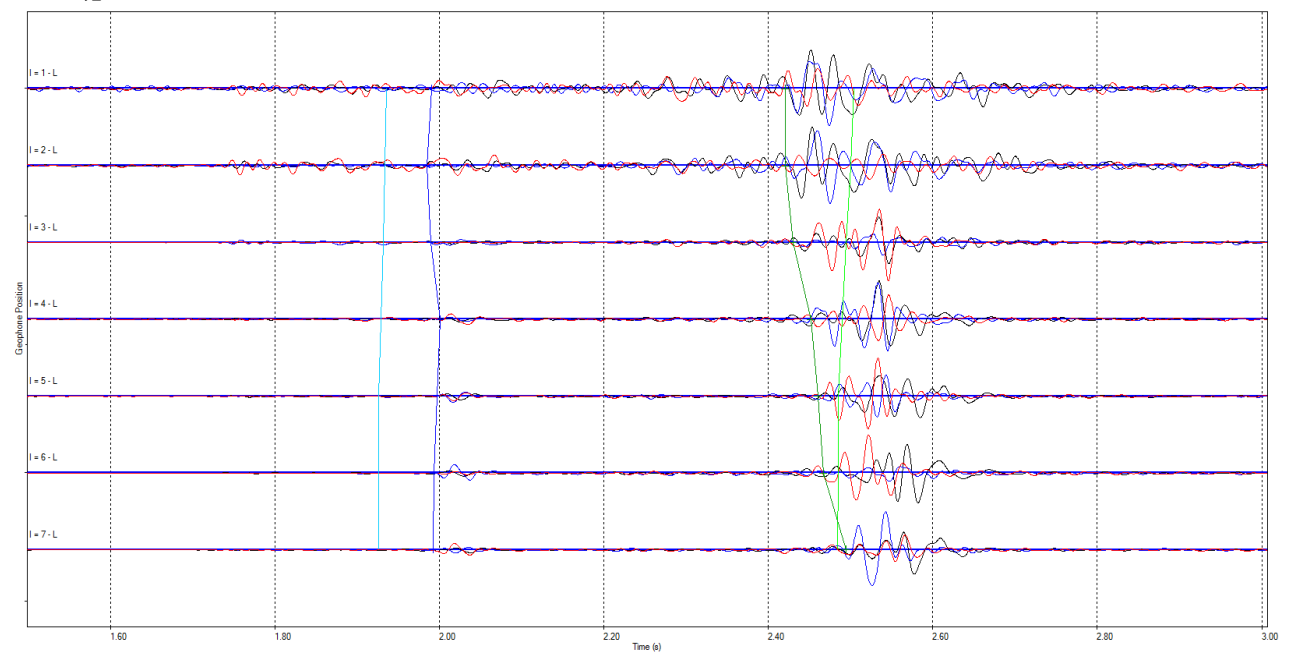
The following images show the seismograms for both the Stedum and Zeerijp receiver arrays at each located event. The three trace lines correspond to the x,y and z components of the geophone. The vertical axis shows the geophones numbered down the well, whilst the horizontal axis corresponds to the time in seconds from the beginning of the trace recording. The dark blue line down the array gives the picked direct P arrival, whilst the light blue line corresponds to the 'best fit' P direct arrival time based on the iterated arrival time produced by the location algorithm. The dark green lines correspond to the picked S arrival whilst the light green line corresponds to the best fit S arrival.

15/12/13 06:48:25

Stedum well

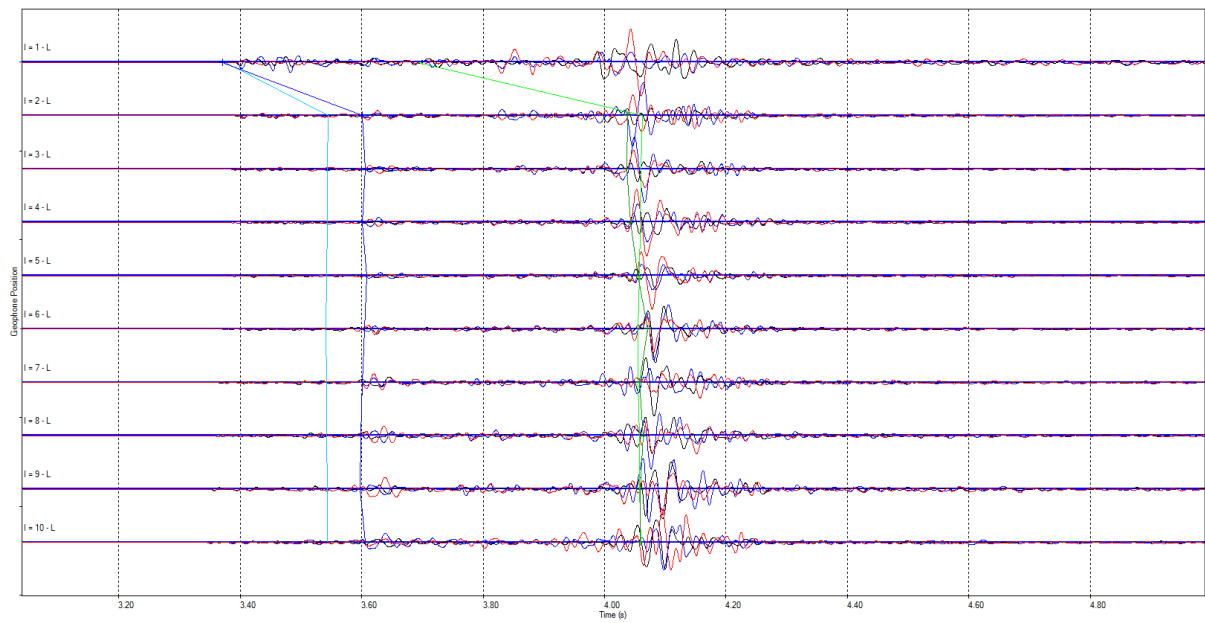


Zeerijp Well

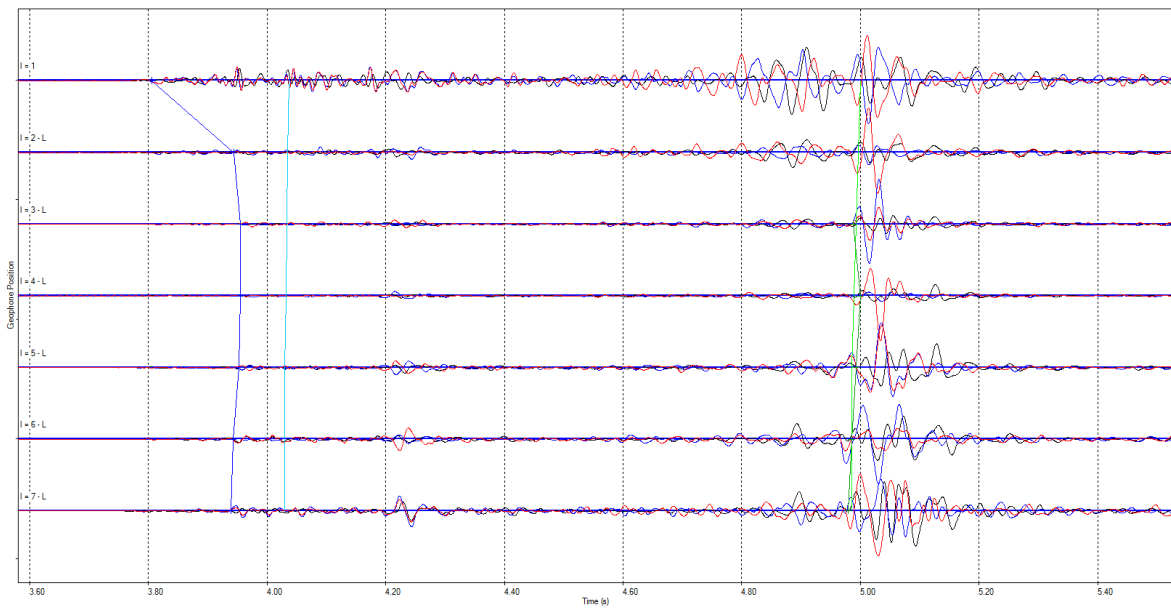


15/12/13 07:39:55

Stedum well

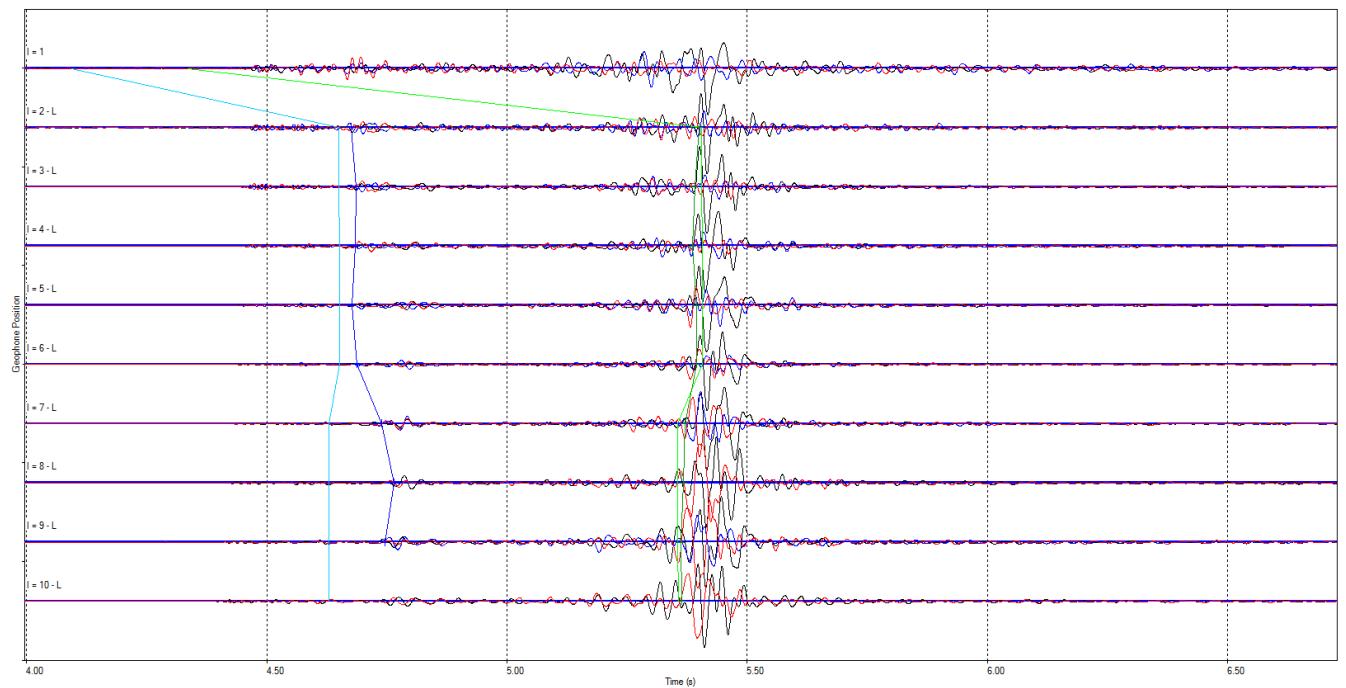


Zeerijp well

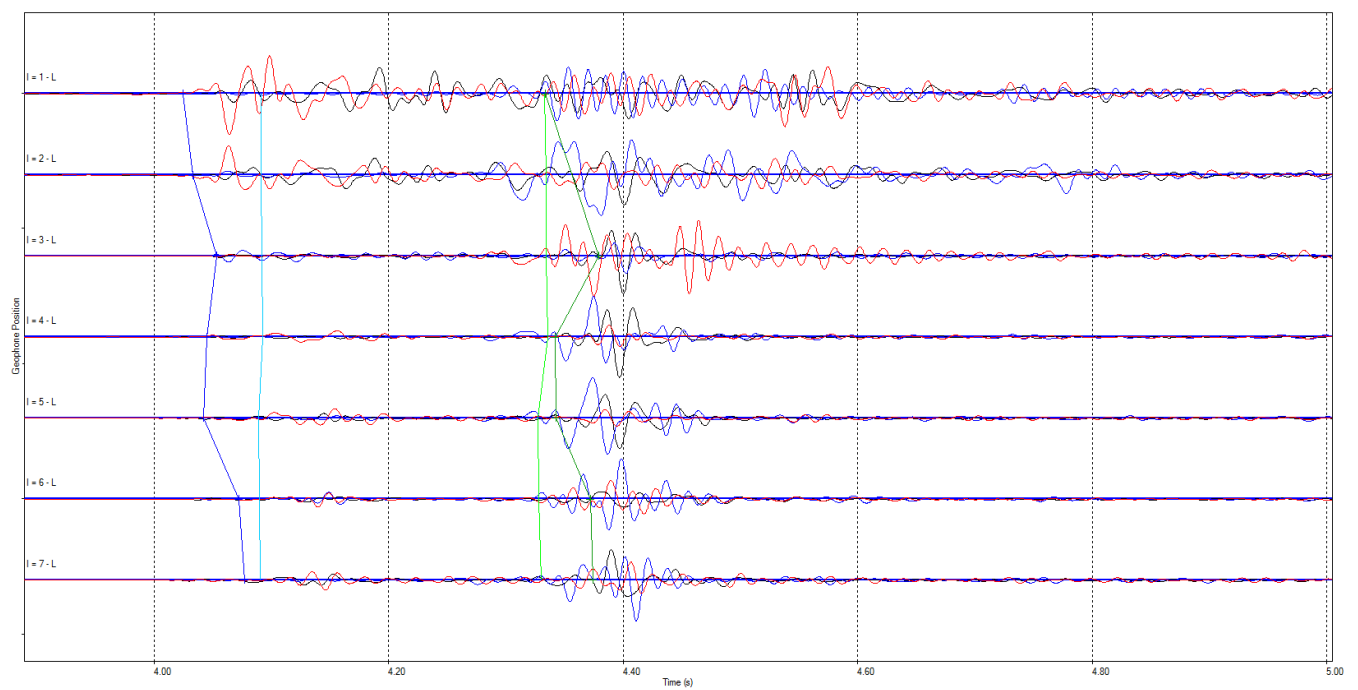


12/04/14 05:36:04

Stedum well



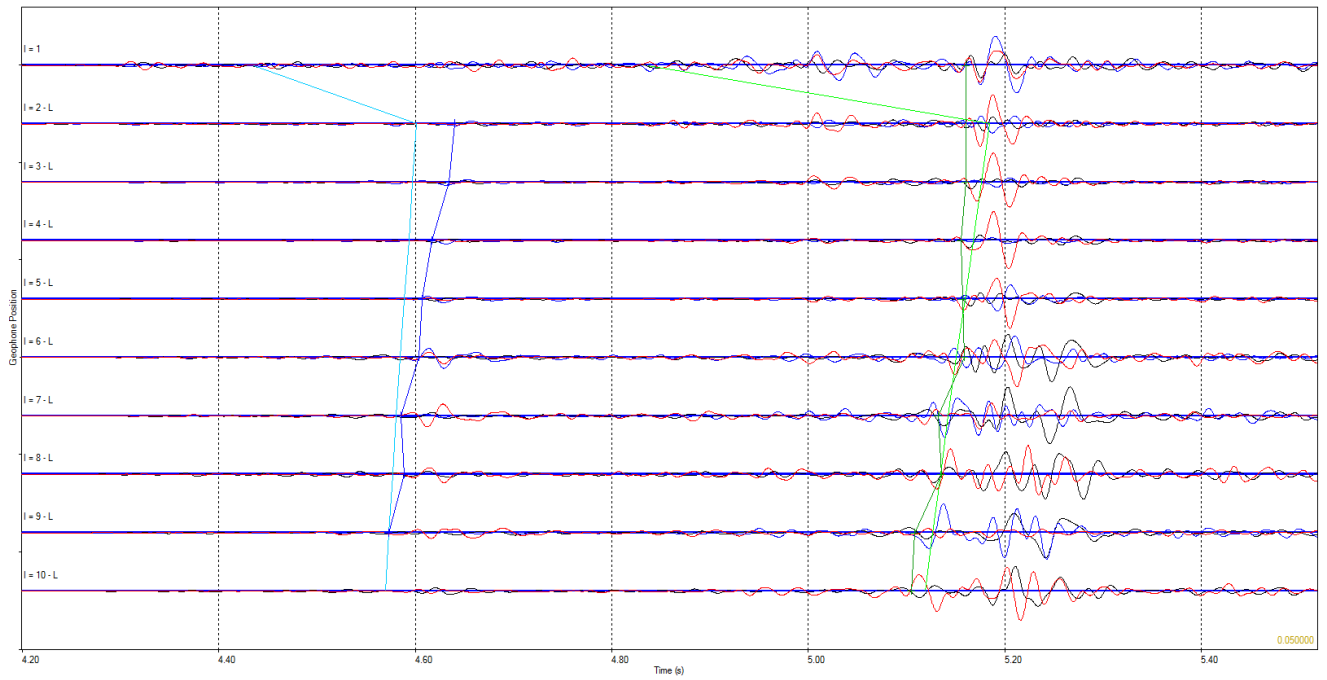
Zeerijp



12/04/14 12:56:10

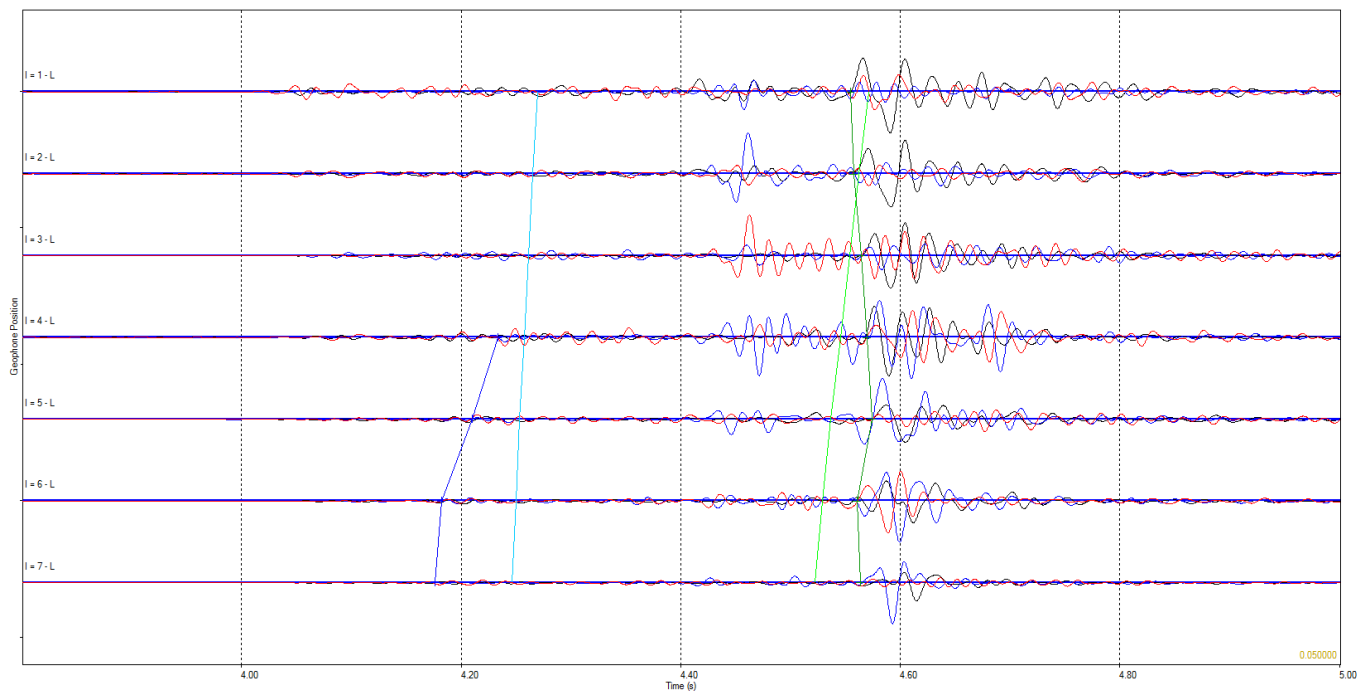
Stedum well

Good fit between computed and picked arrivals.



Zeerijp well

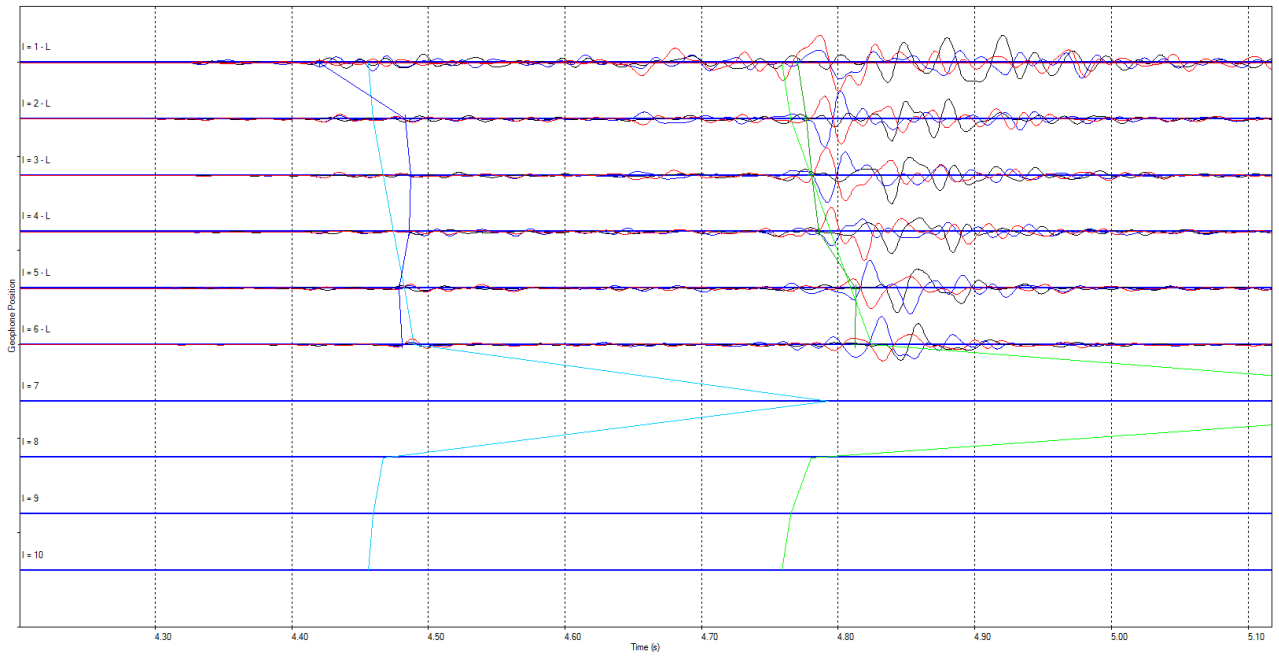
Poor fit between computed and picked arrivals due to poor signal to noise ratio at this receiver array.



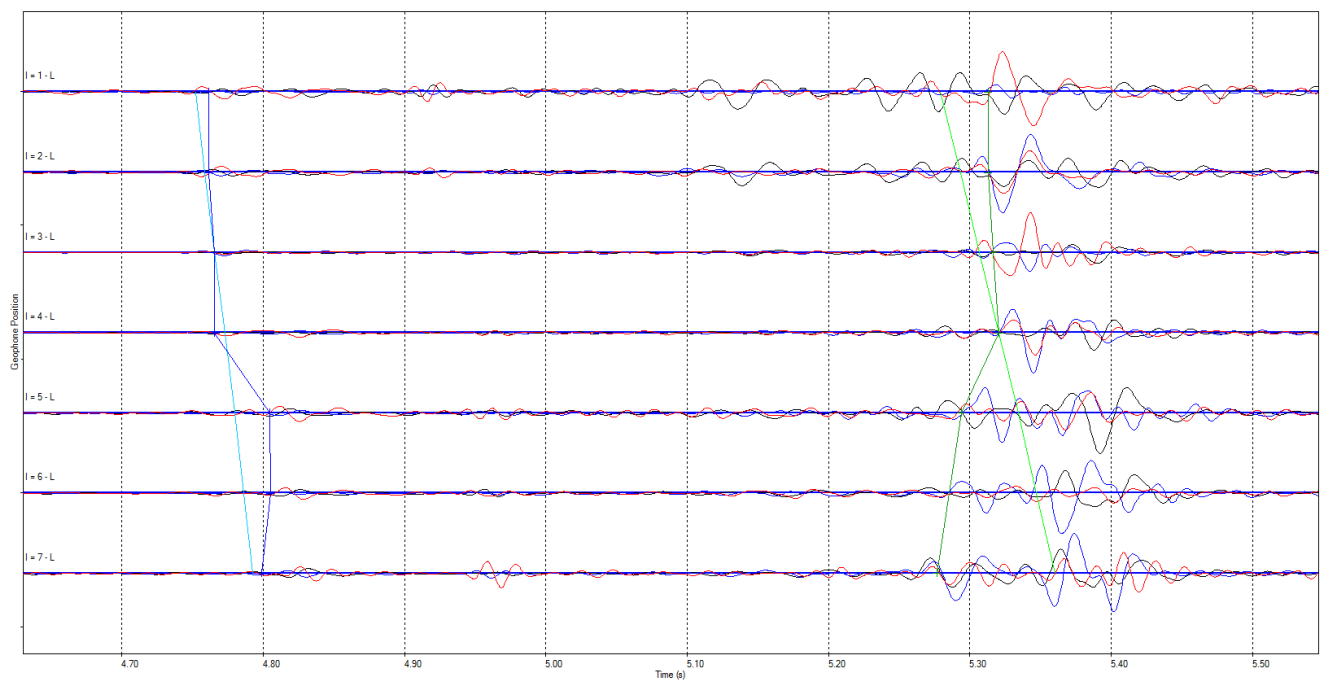
17/04/14 20:21:01

Stedum Well

Anomalous best fit result on geophone 7 due to program bug

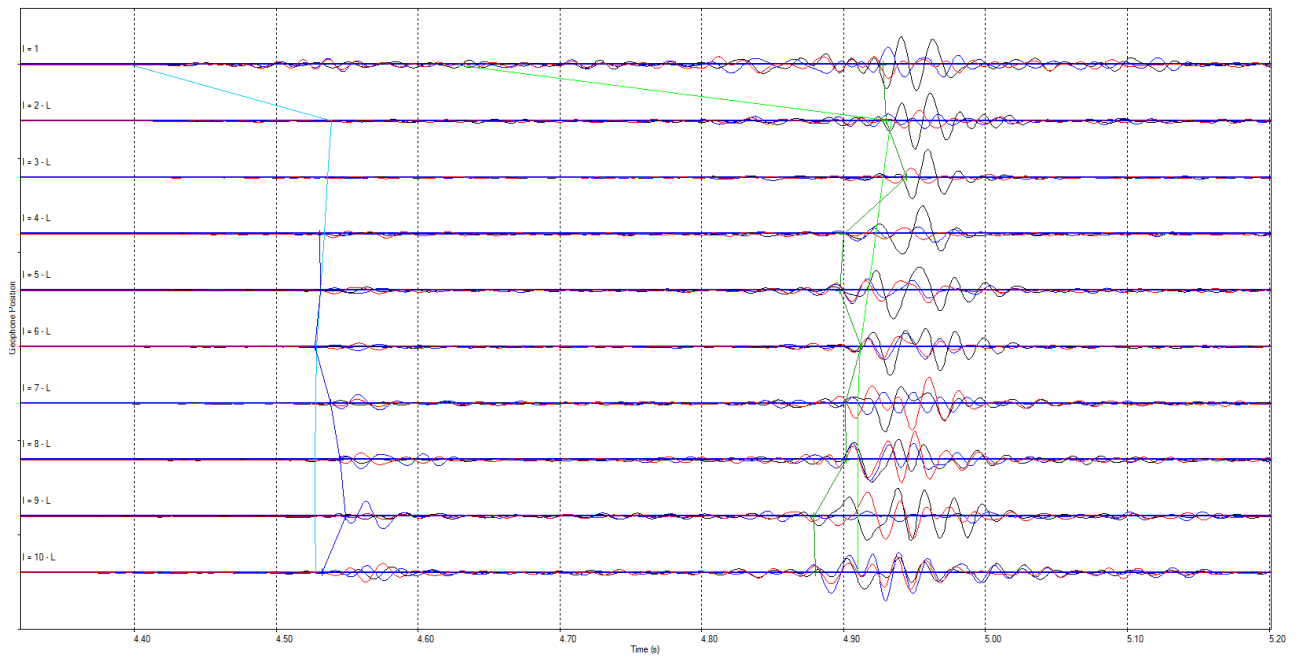


Zeerijp Well

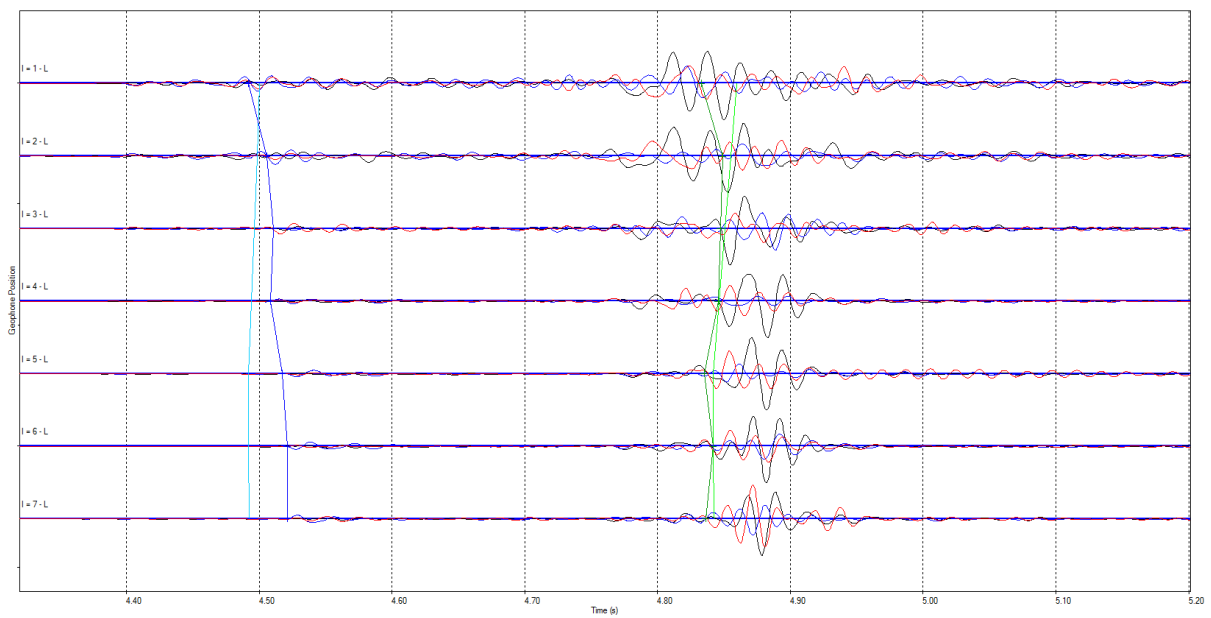


22/03/14 17:16:15

Stedum well



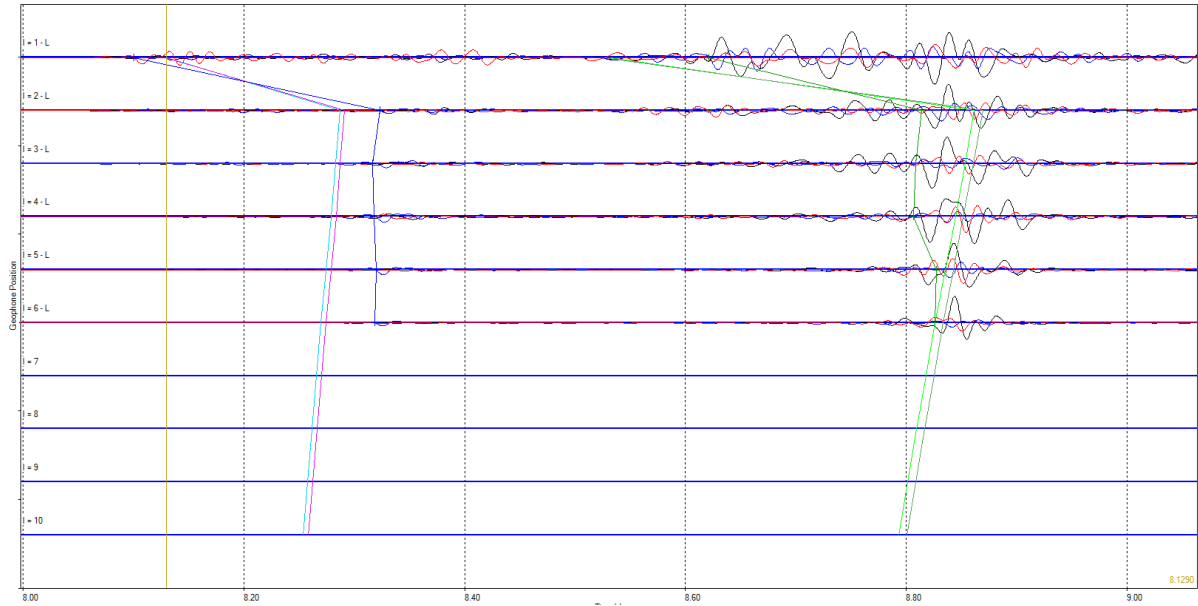
Zeerijp Well



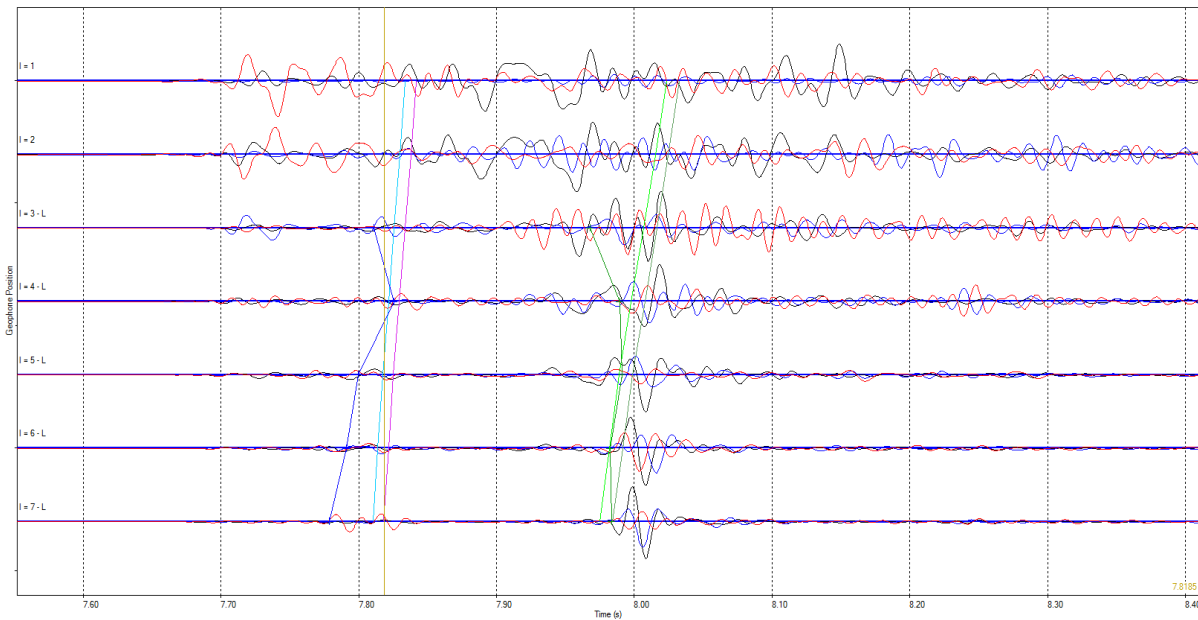
22/04/14 03:13:14

A difficult event to interpret. P and S separation appears to suggest the event must have originated from the Carboniferous layer. However, the picked move-out suggests the event originated from the reservoir. Consequently, this may point to a limitation of the velocity model.

Stedum Well



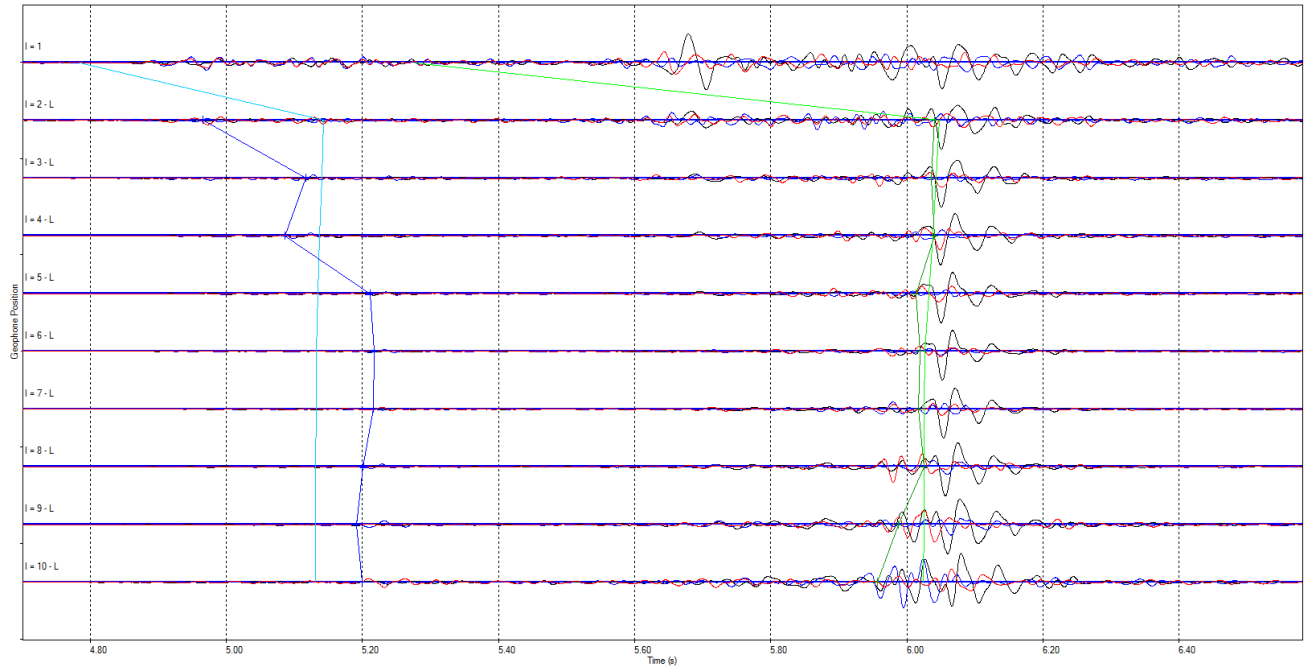
Zeerijp well



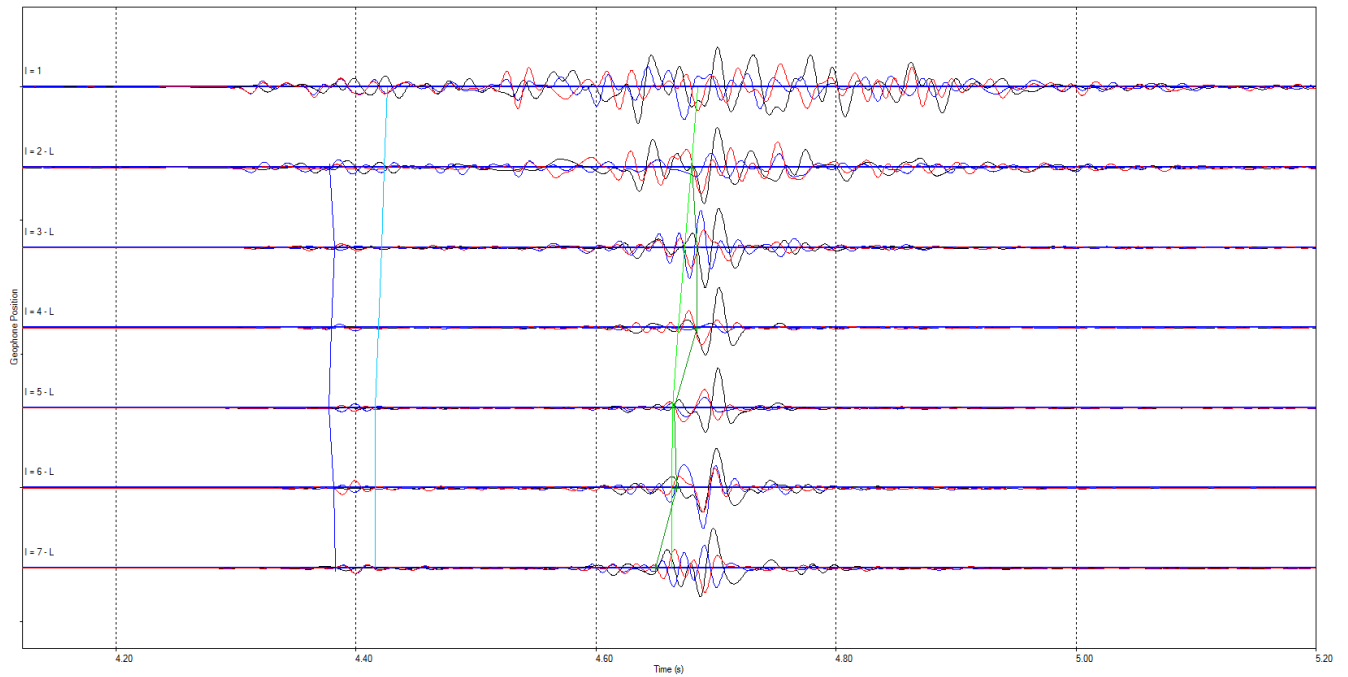
30/11/13 19:29:01

Stedum Well

A poor fit between picked and computed P arrival time can be seen. This was due to the difficulty in picking the low amplitude arrival. Both receiver arrays have good match on the direct S wave arrival time.

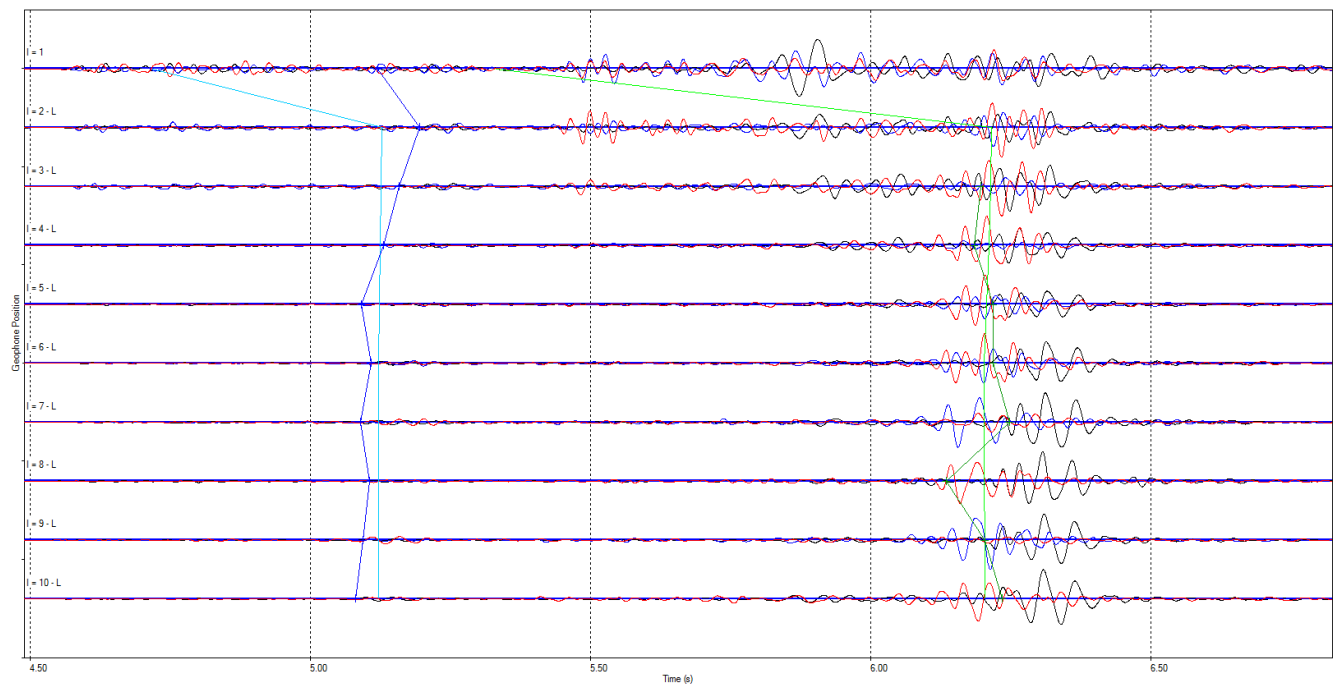


Zeerijp well



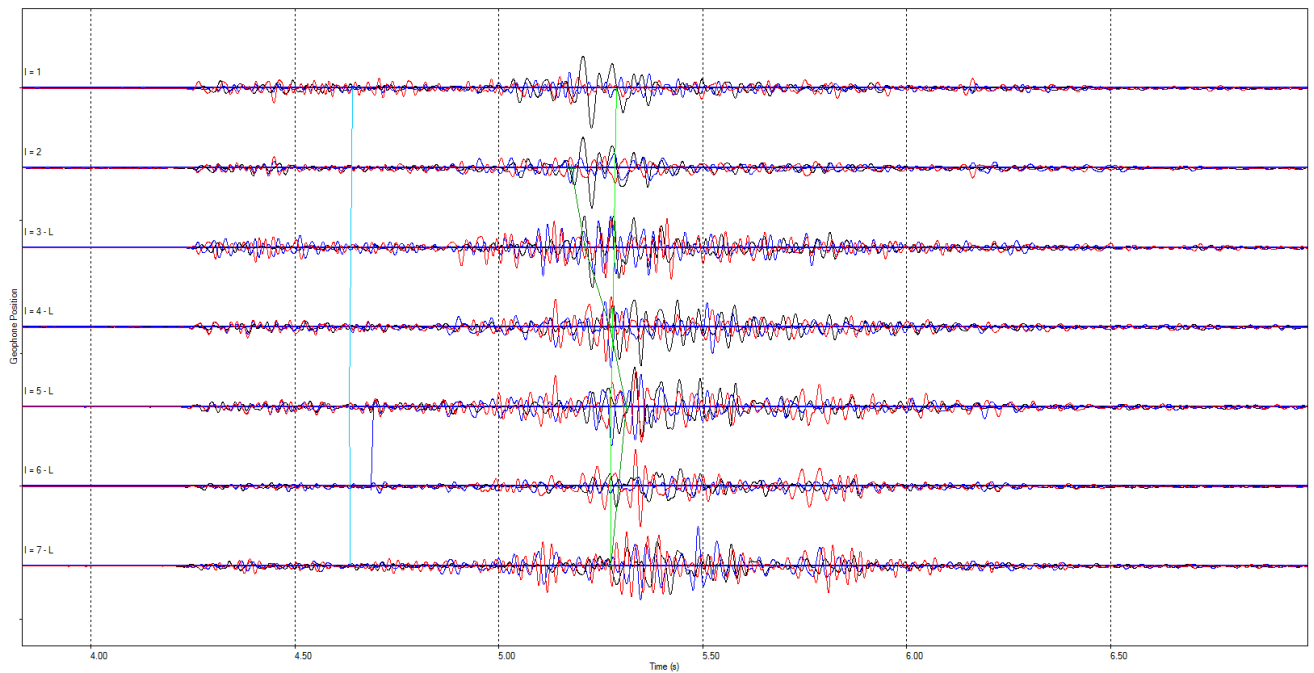
01/04/14 18:35:13

Stedum Well



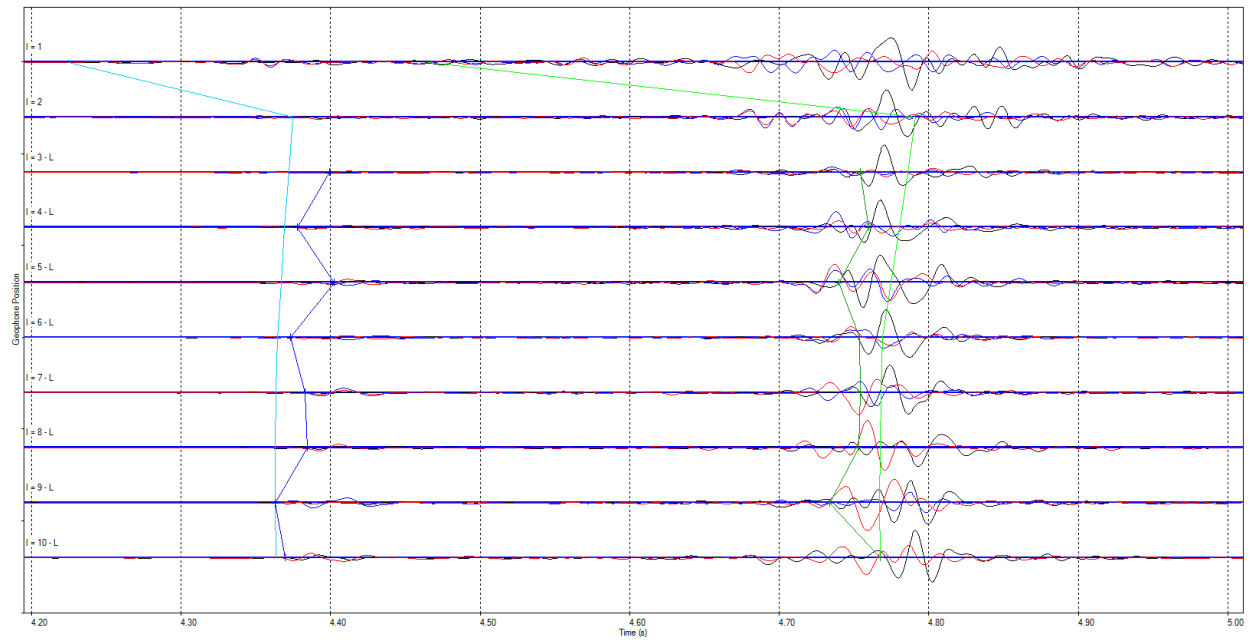
Zeerijp Well

Very difficult to interpret this arrays seismograms. P-wave arrival was very low in energy and could only be determined for geophones 5 and 6. The S-wave direct arrival time was identified from the increase in the level of the waveform polarisation at this time.

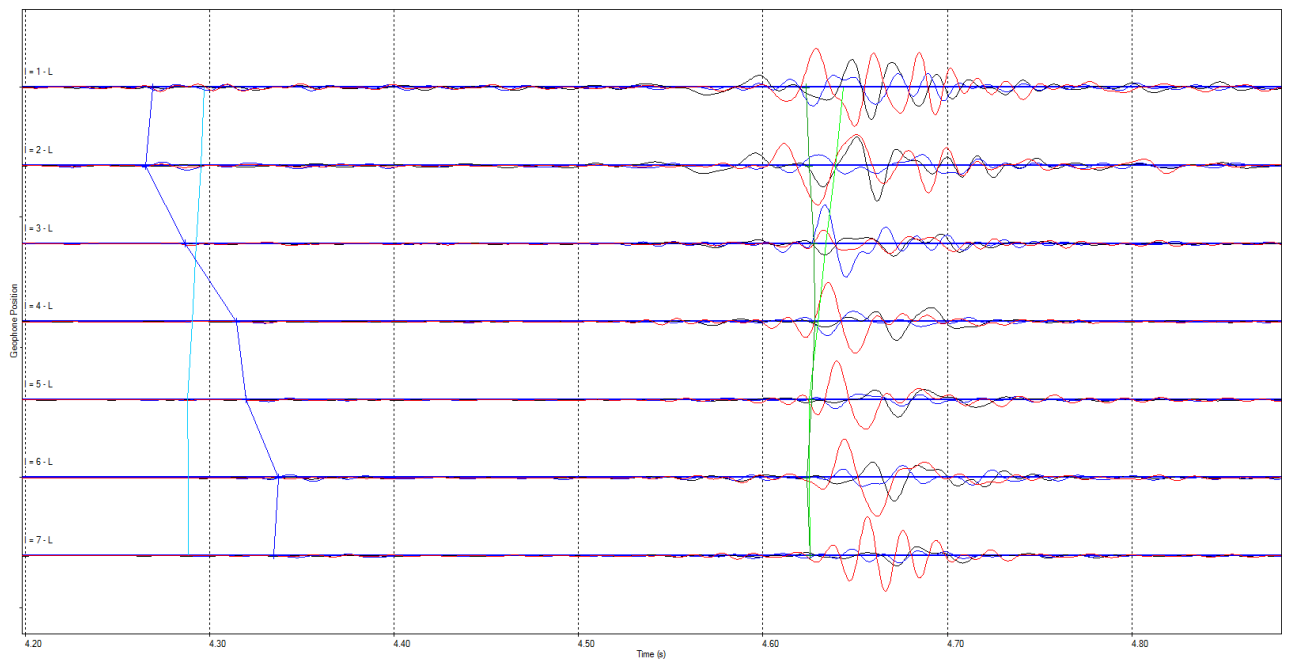


01/04/14 14:13:06

Stedum Well



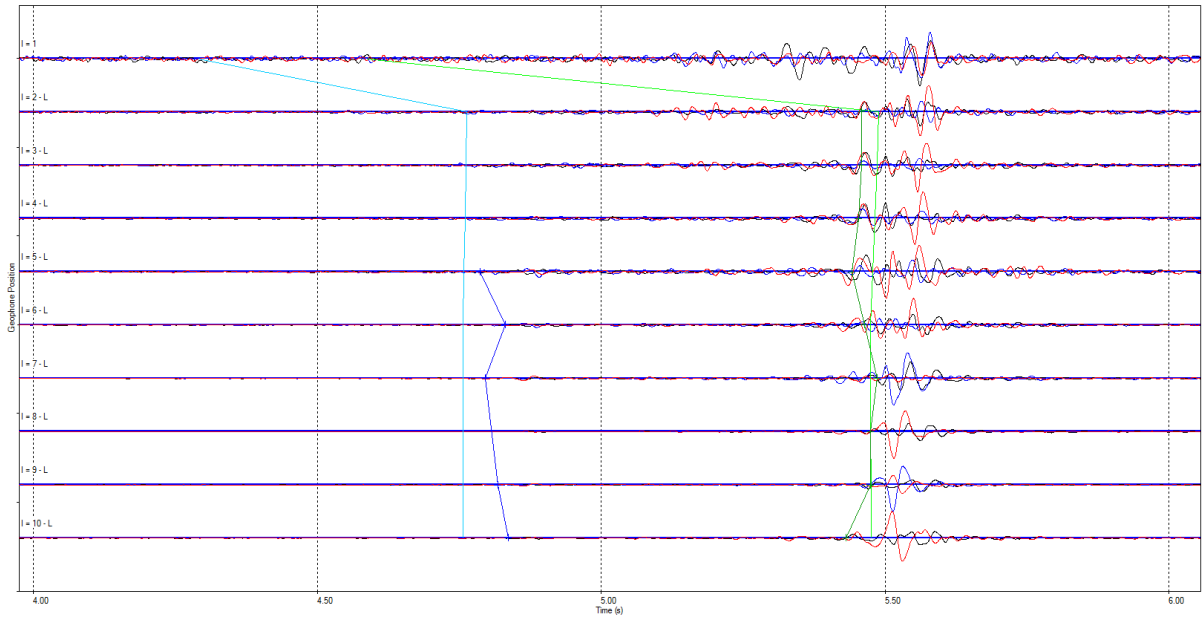
Zeerijp Well



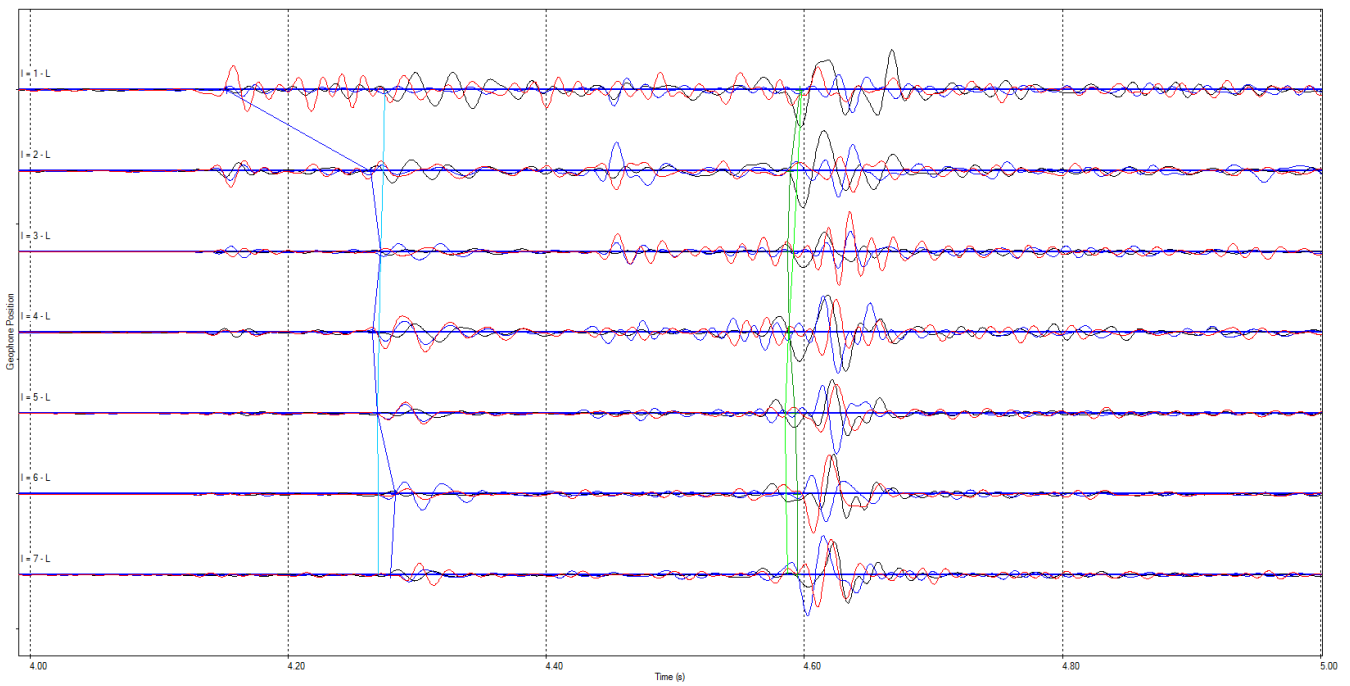
06/04/14 14:47:18

Stedum Well

Poor match with STD P wave arrivals due to low amplitude arrival. Good match with other arrivals.

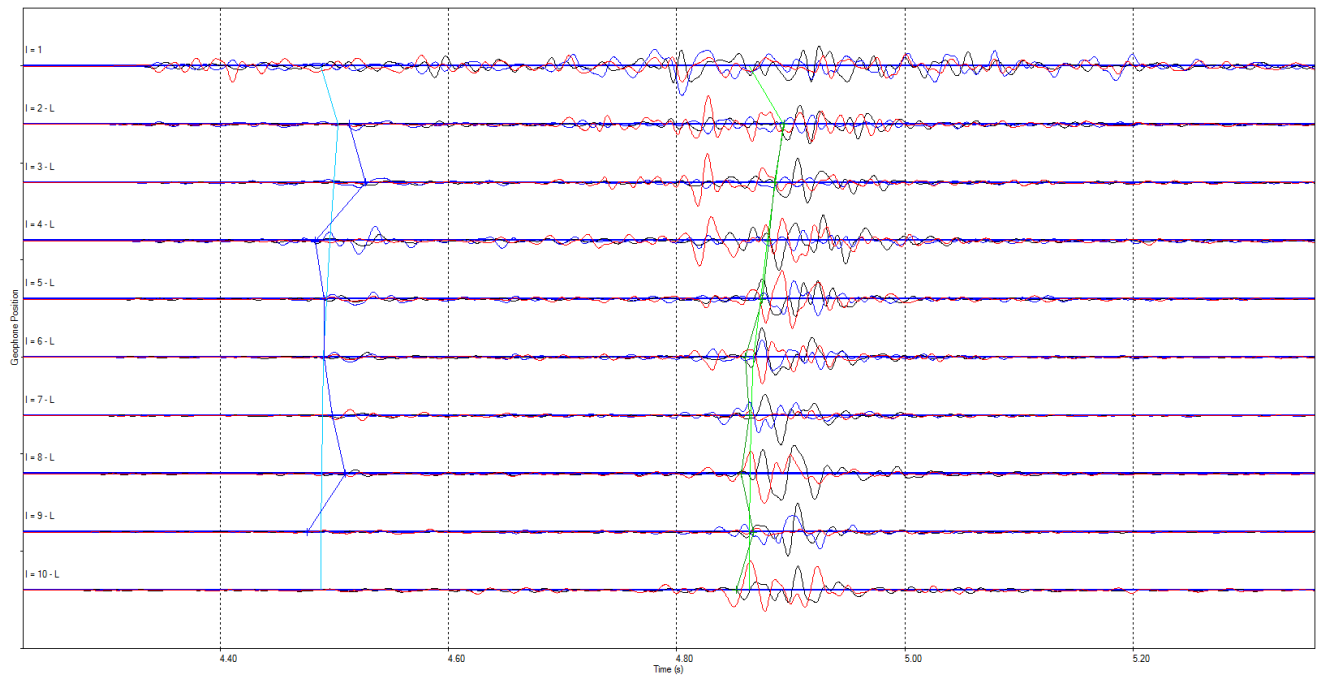


Zeerijp



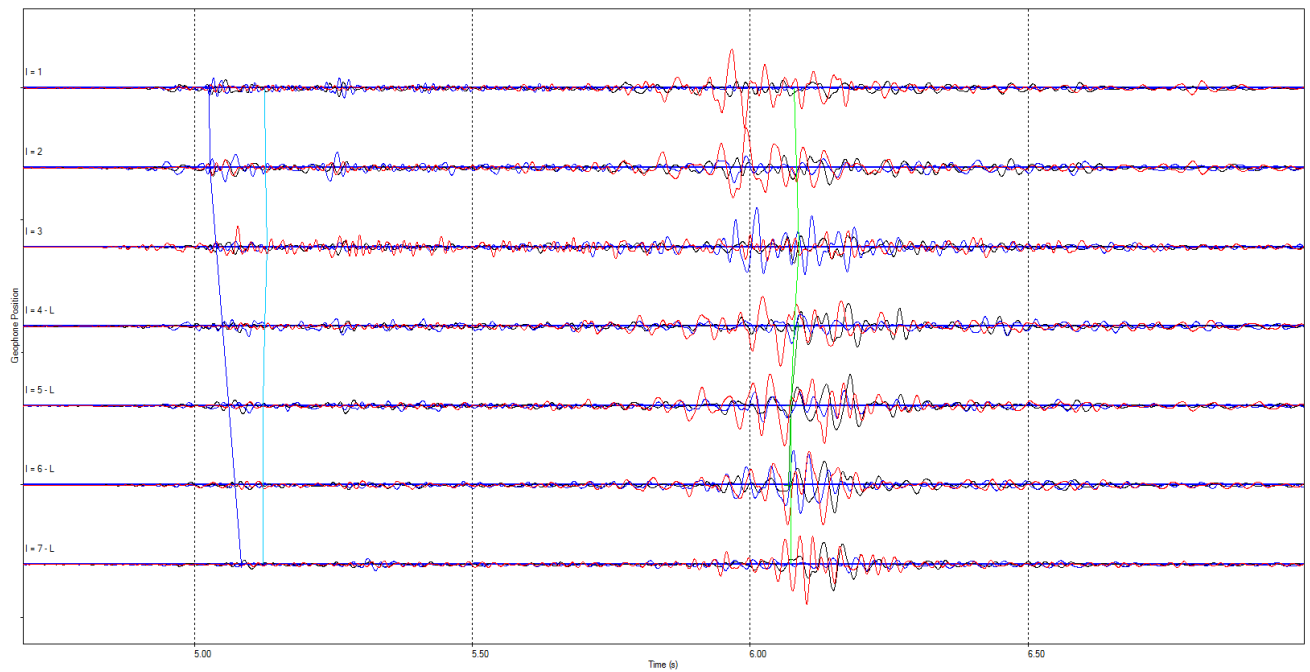
10/04/14 20:56:15

Stedum Well



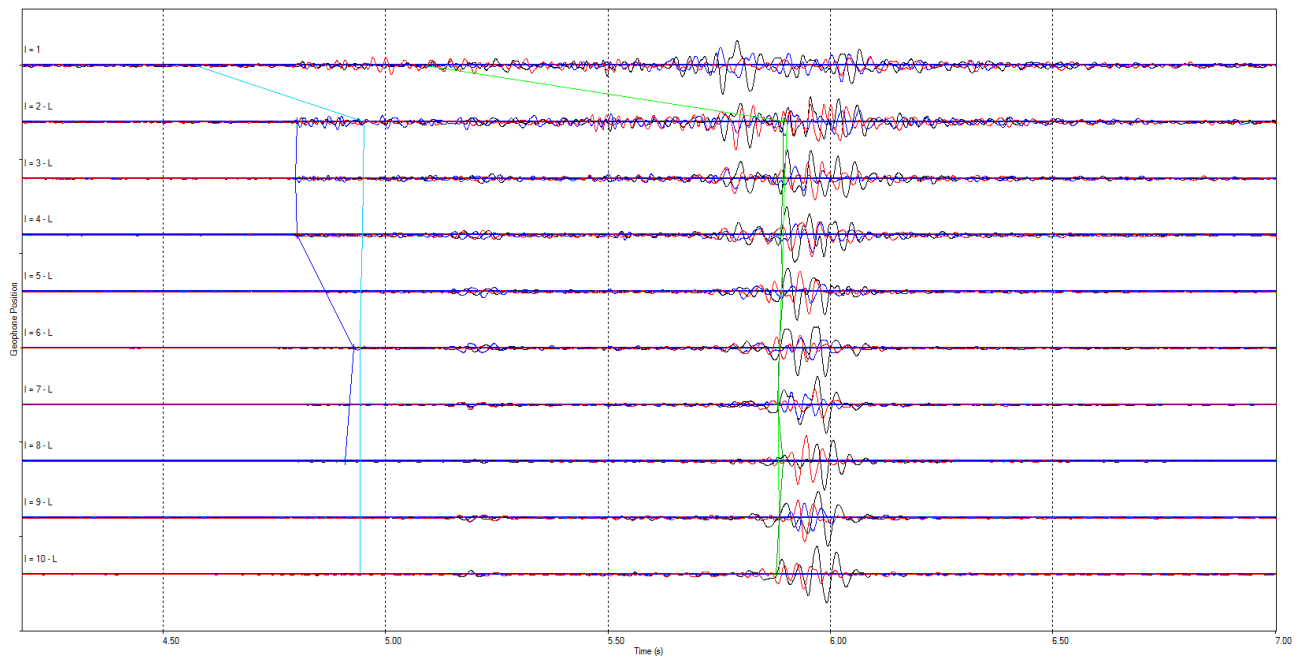
Zeerijp Well

Event was very difficult to interpret and only three P and S picks were made on this array. Location was largely based around the arrival times at the Stedum well.

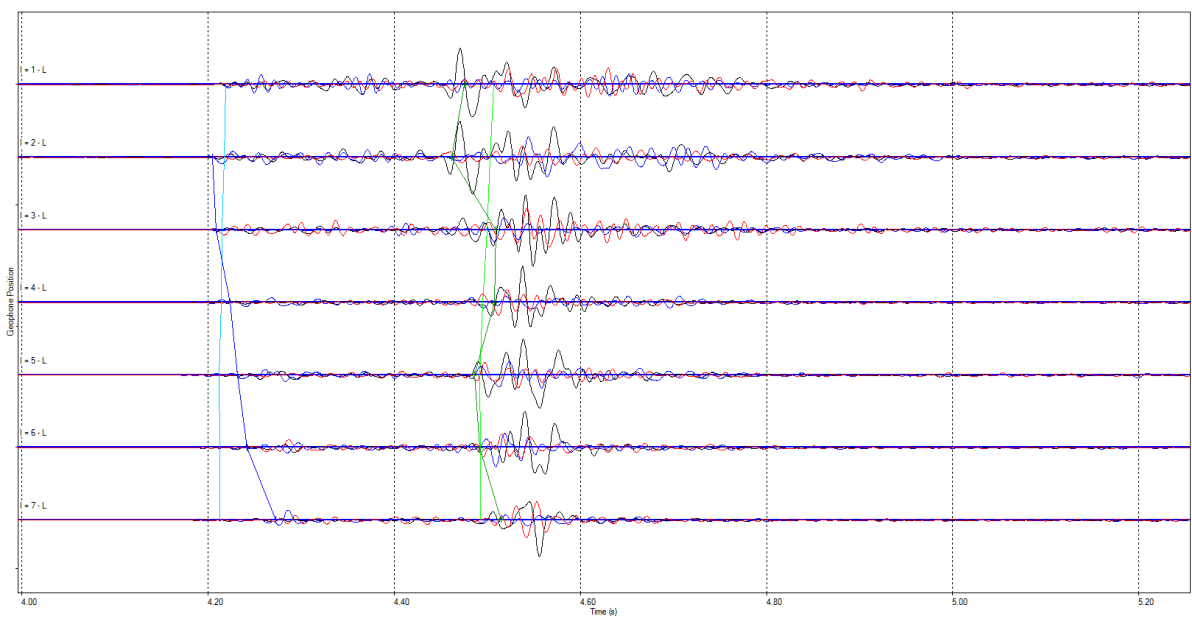


11/04/14 20:48:31

Stedum Well



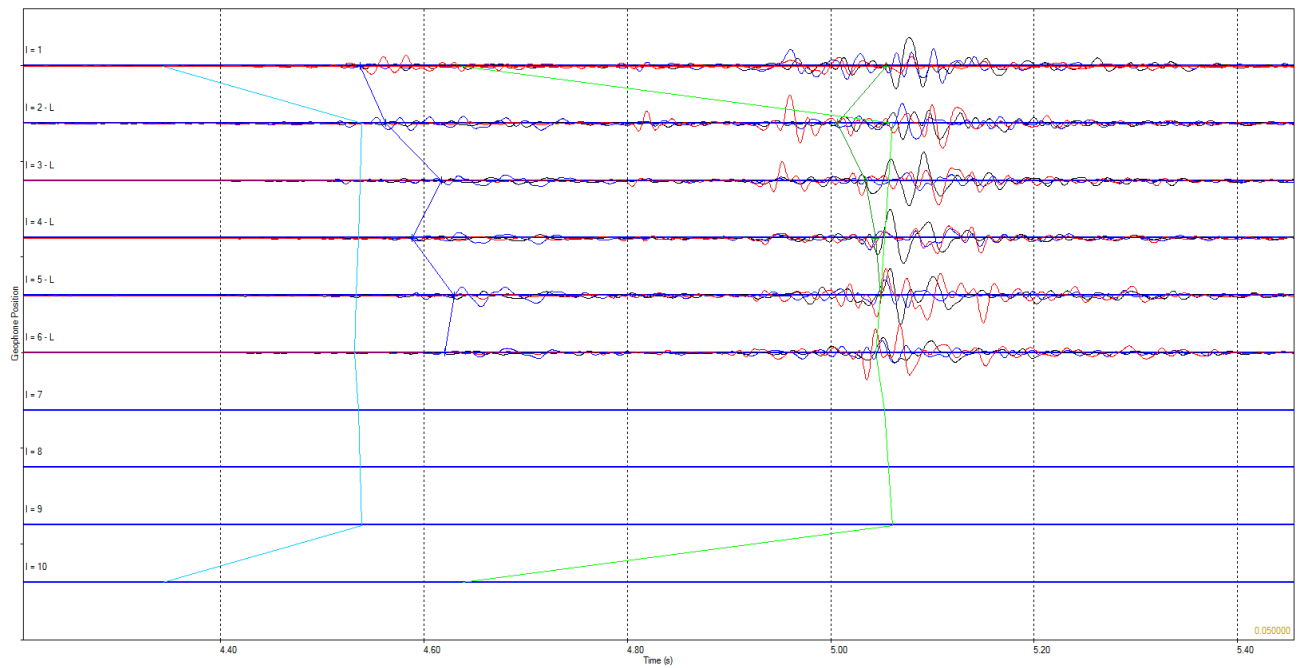
Zeerijp Well



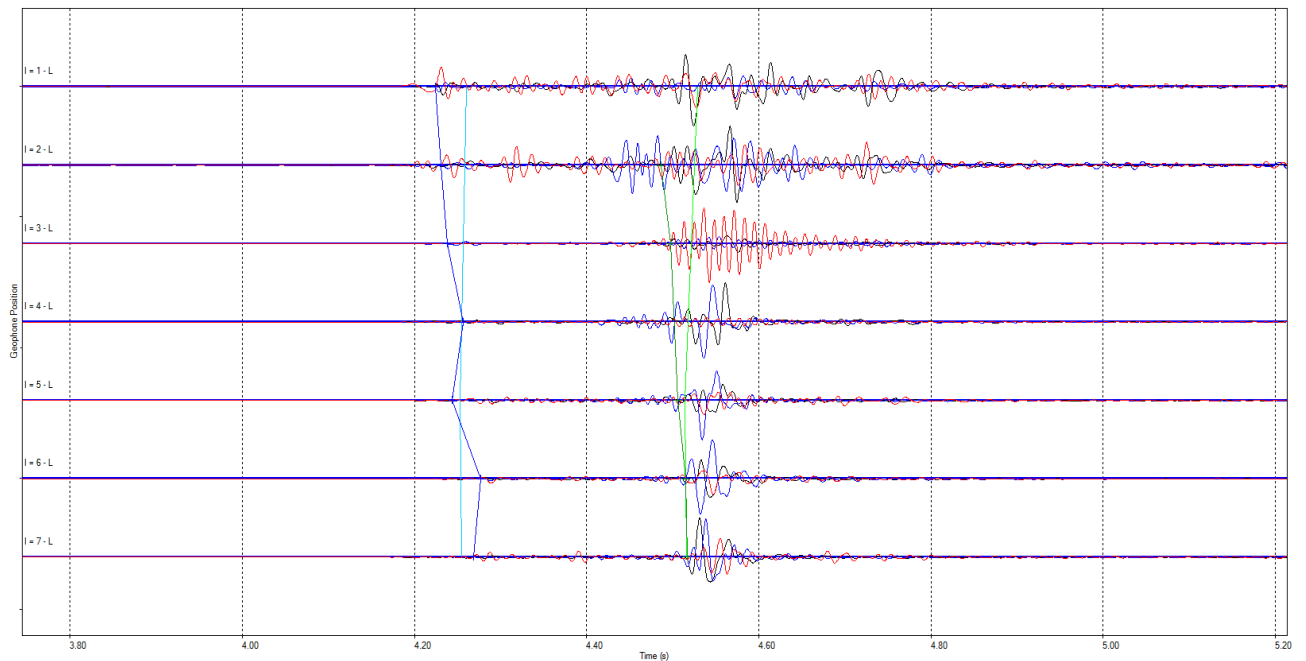
03/05/14 20:39:06

Stedum Well

Poor match on P wave picked and computed arrival times.



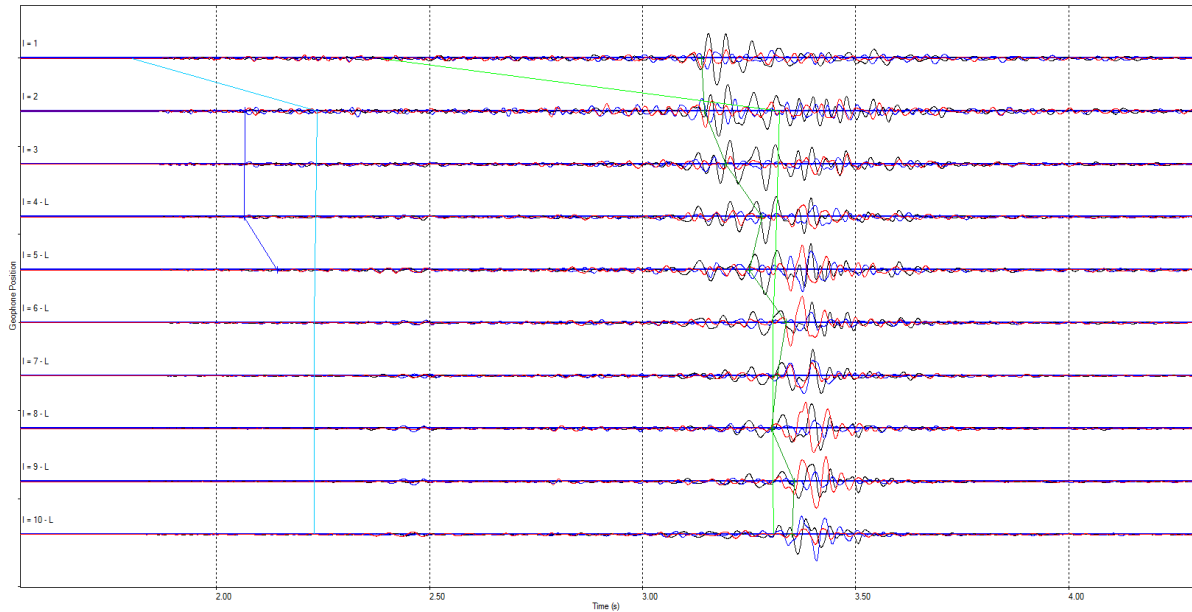
Zeerijp Well



17/12/13 21:37:55

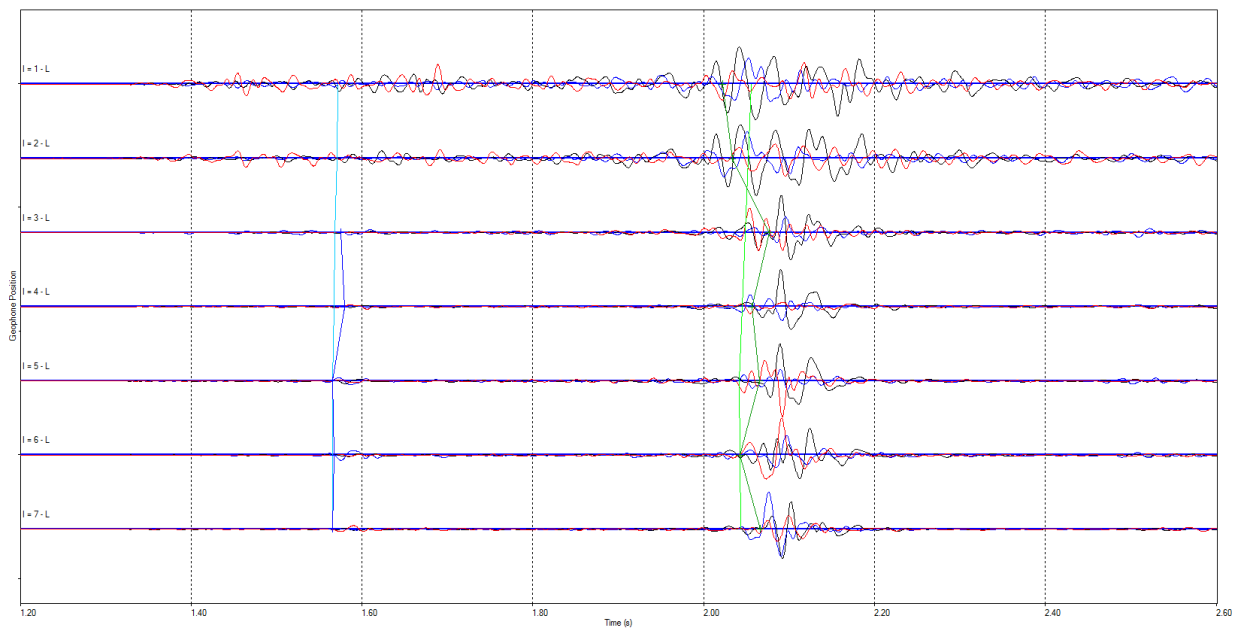
Stedum well

P direct arrivals difficult to identify and only 3 picks were made, a large residual can be seen between the computed and picked P arrival times.



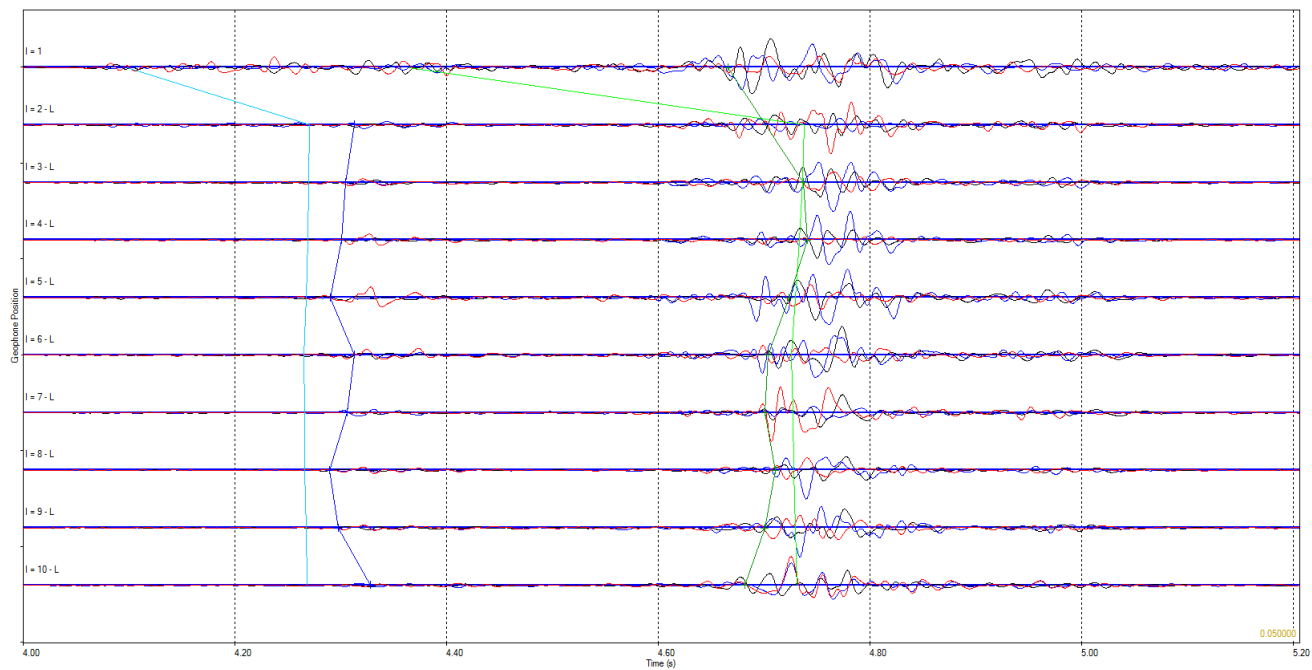
Zeerijp

Computed arrivals appeared to match picked with a low residual error. It was difficult to interpret the P arrivals in the first two geophones.

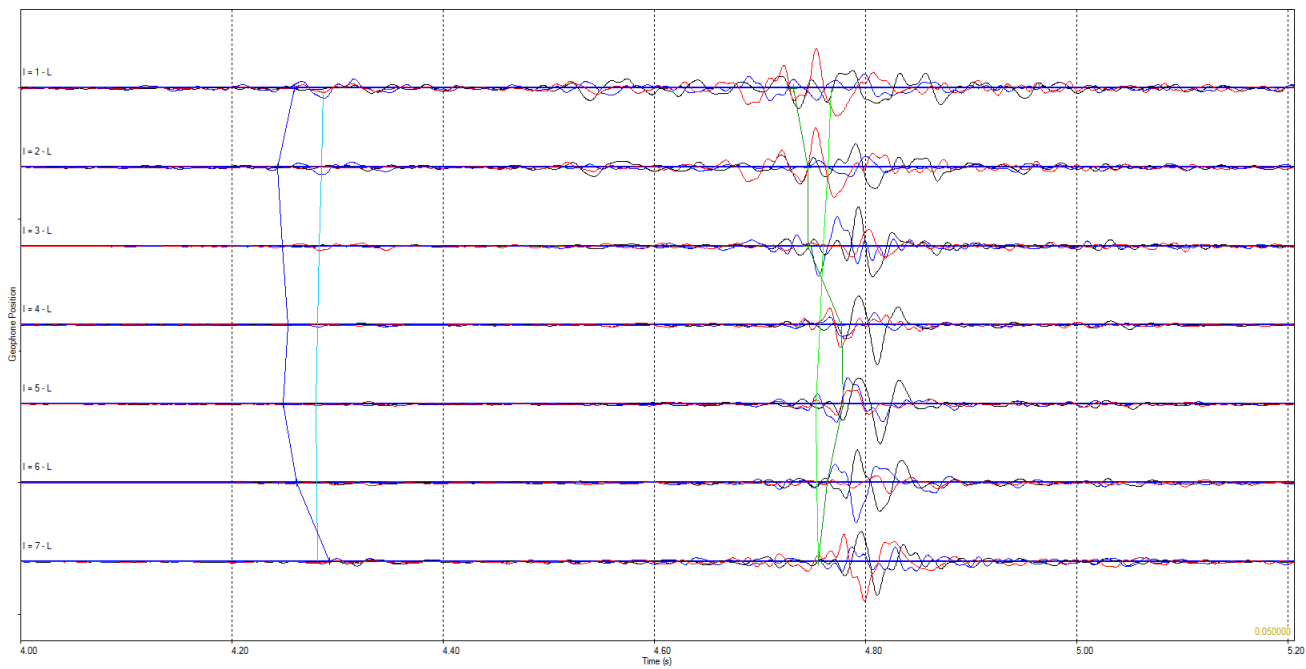


01/12/13 09:21:03

Stedum well

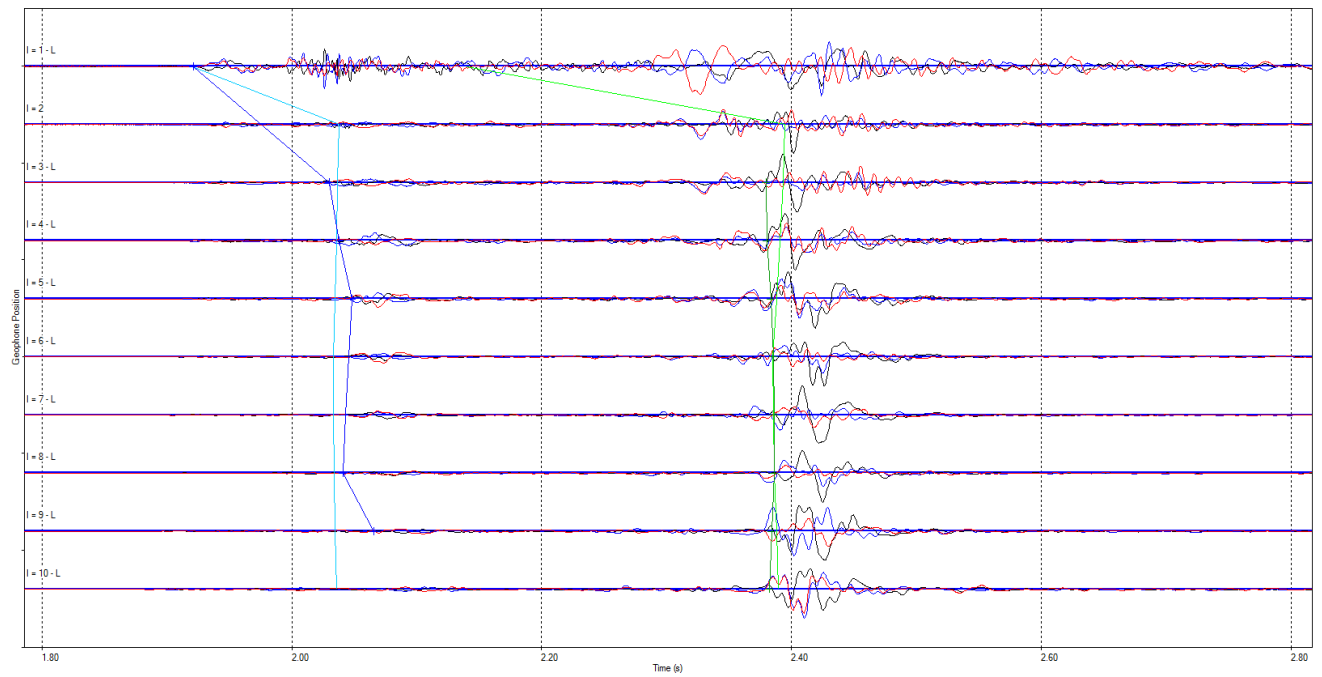


Zeerijp well

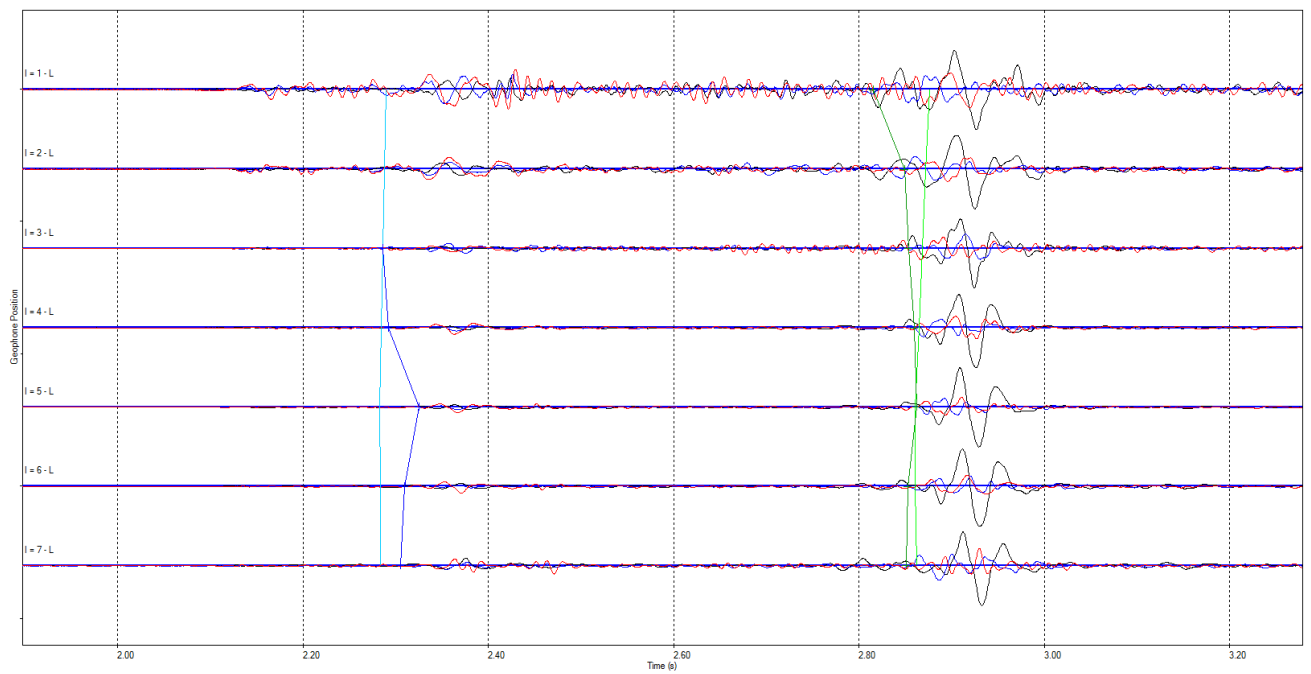


23/03/14 02:23:55

Stedum well



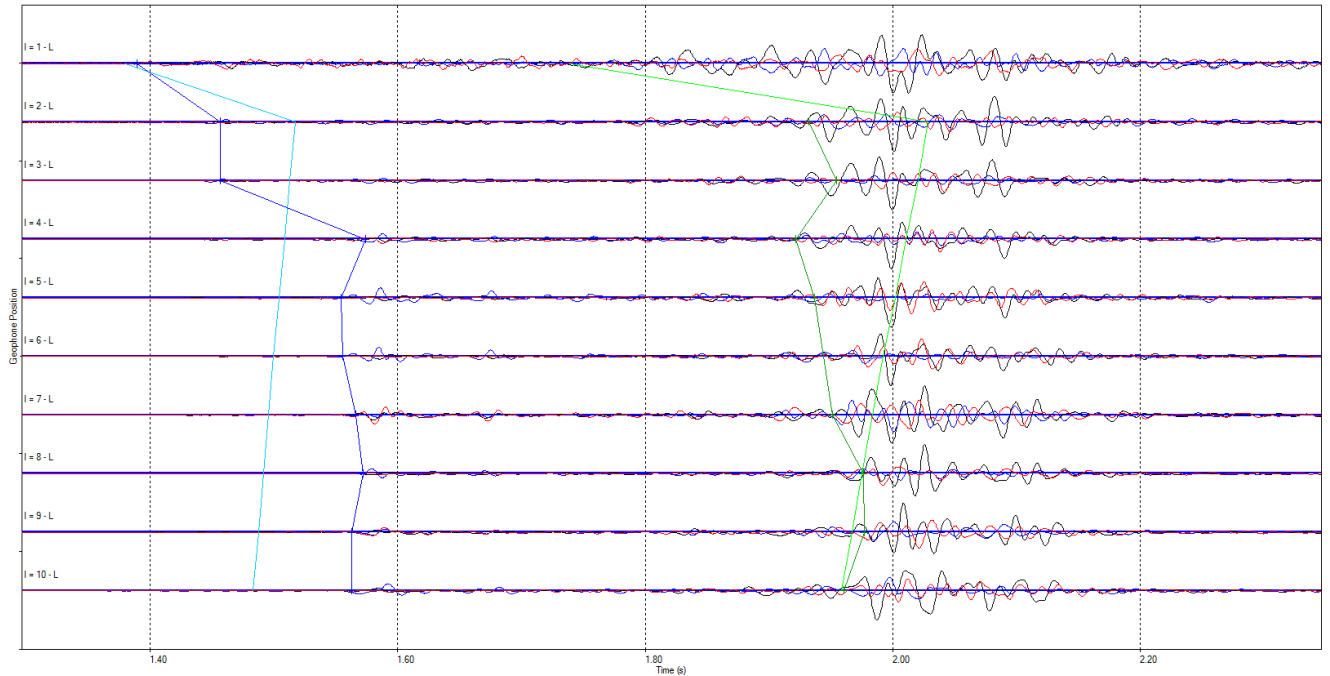
Zeerijp Well



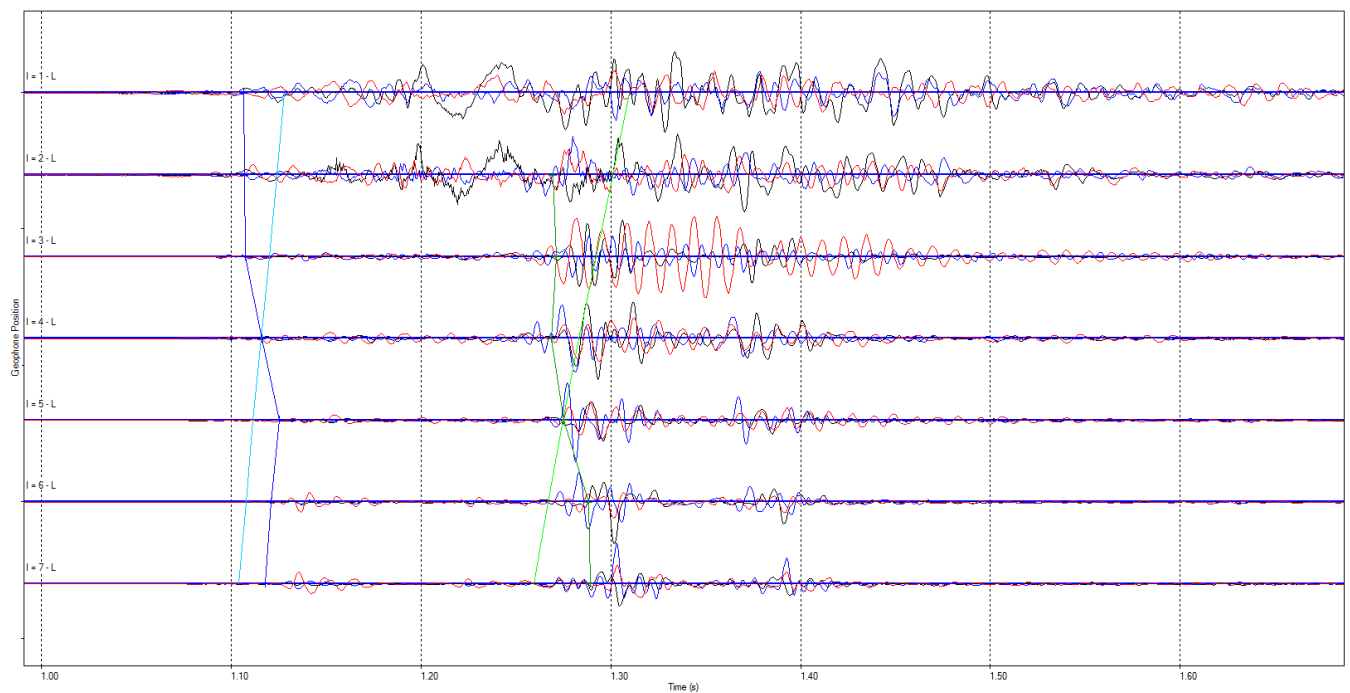
21/03/14 11:28:25

Poor match seen between arrivals with a large residual error. This may be the fault of the velocity model which may provide a poor representation of the subsurface around this point. Rayvectors indicate that the event has originated inside the Carboniferous.

Stedum

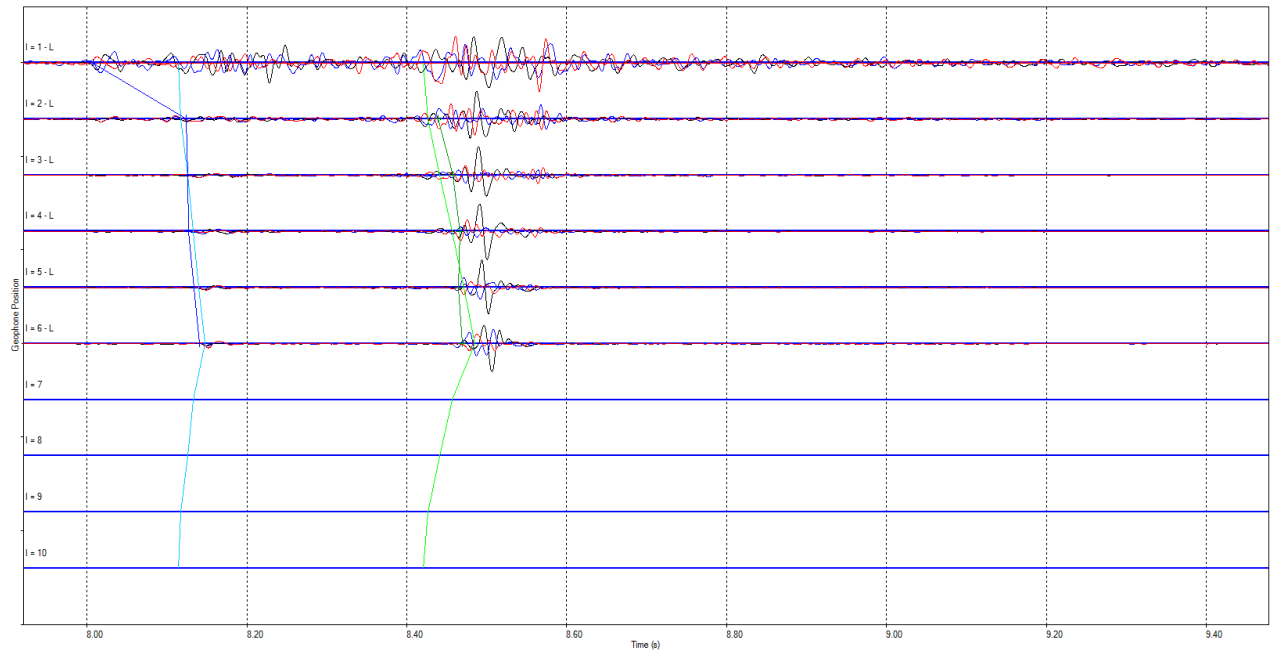


Zeerijp

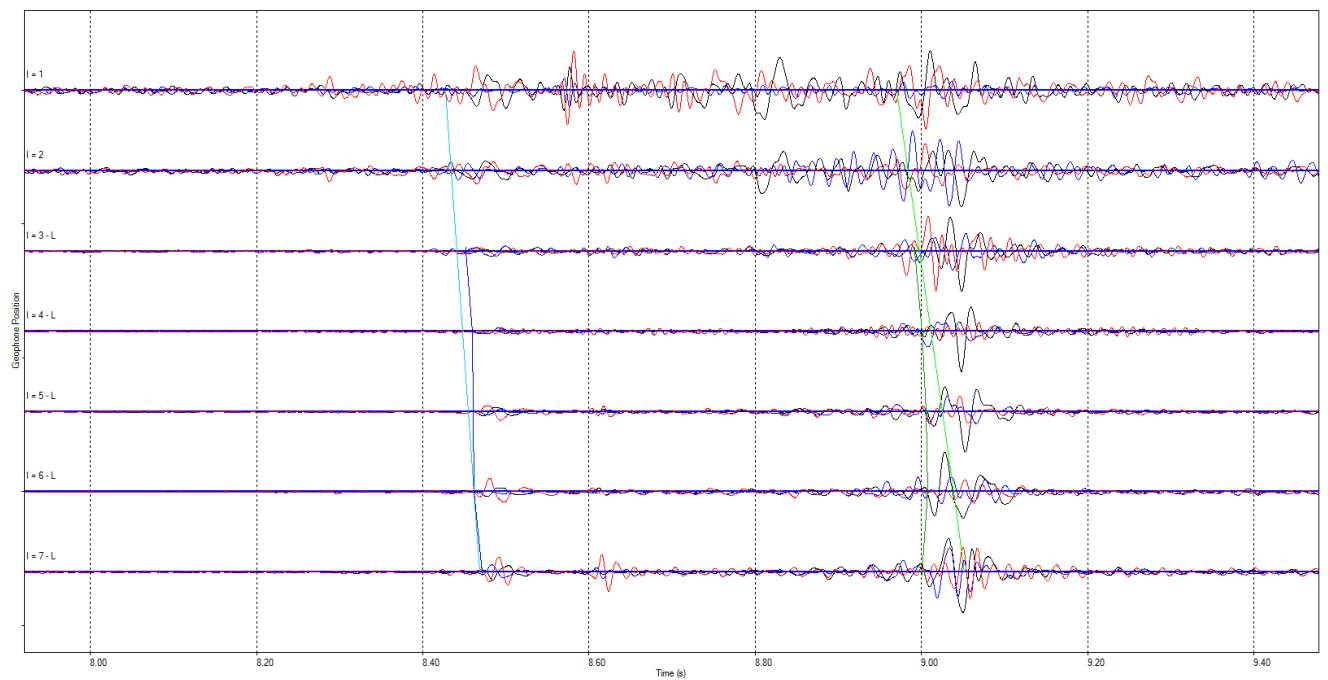


20/04/14 11:20:14

Stedum Well



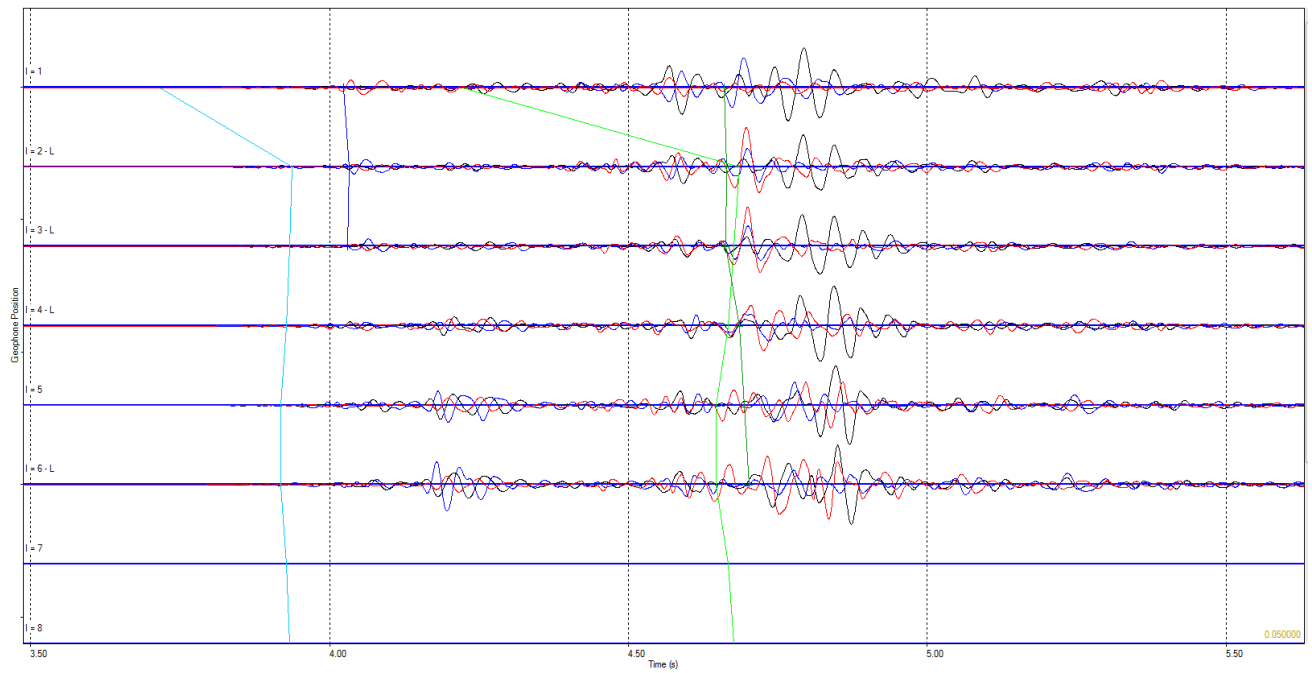
Zeerijp Well



20/04/14 08:36:00

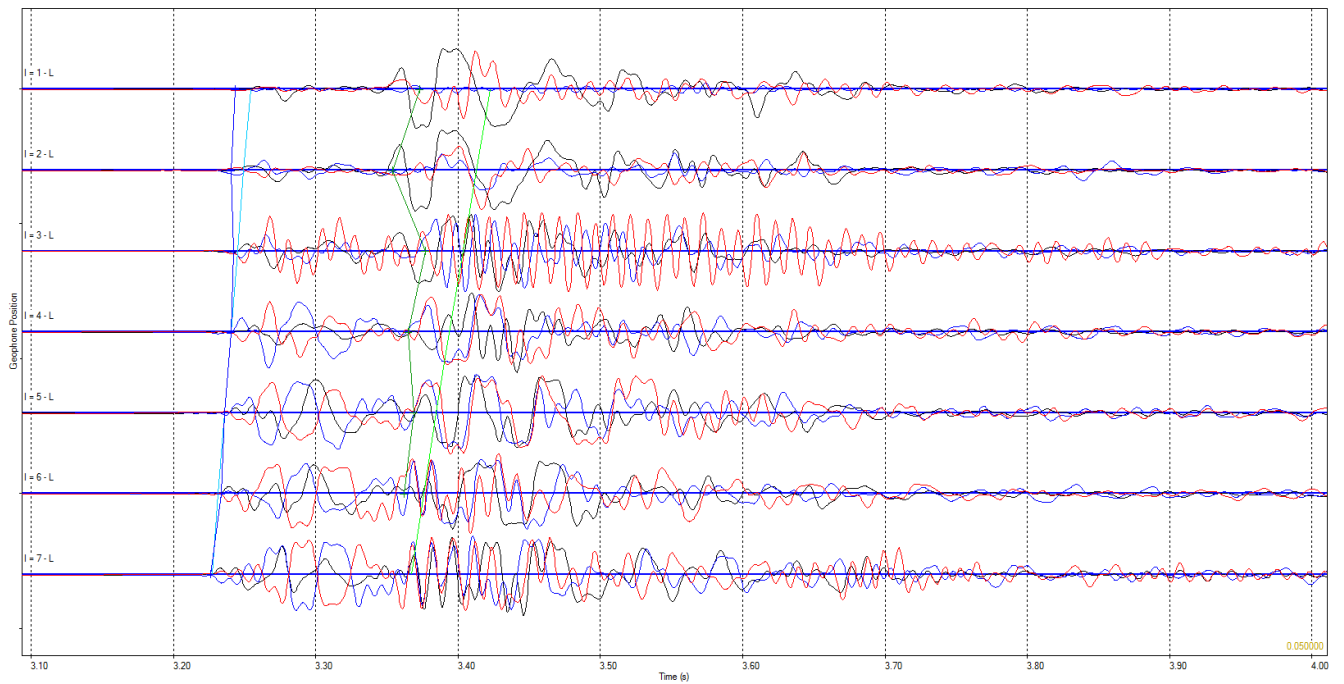
Stedum Well

Mis-match between picked and computed direct P arrivals



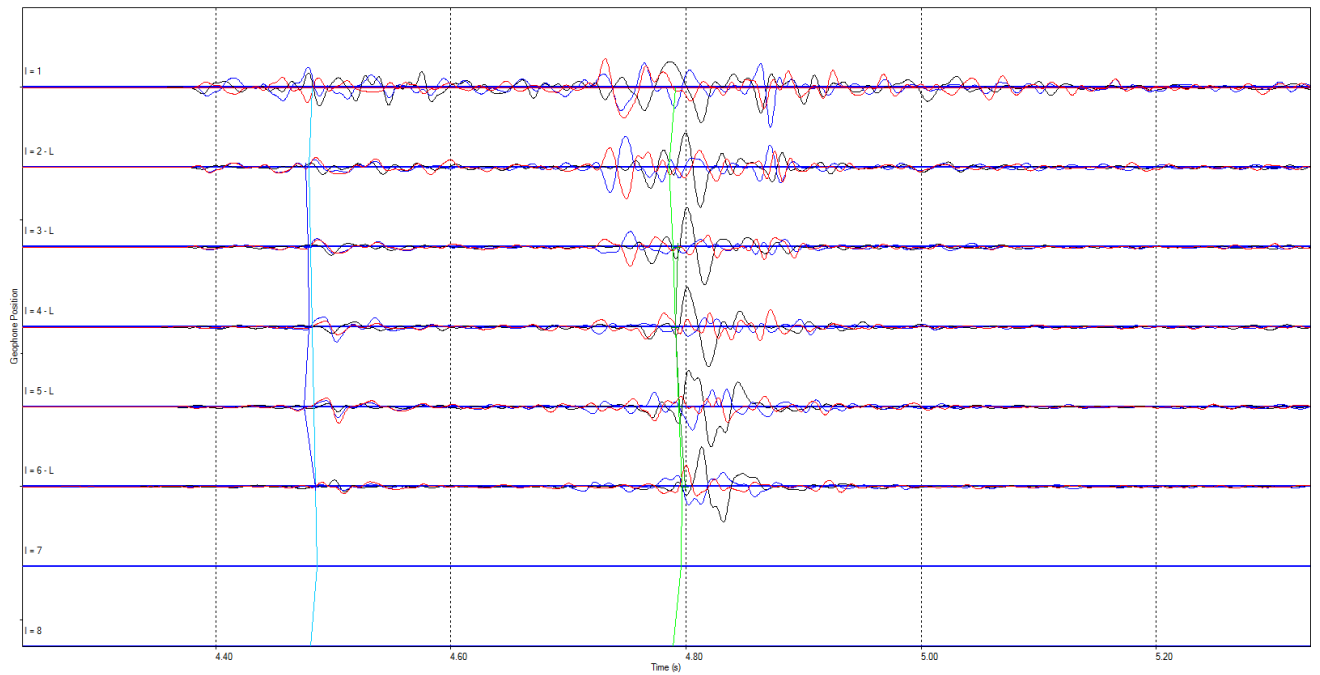
Zeerijp well

Event located close to well giving high amplitude arrivals.

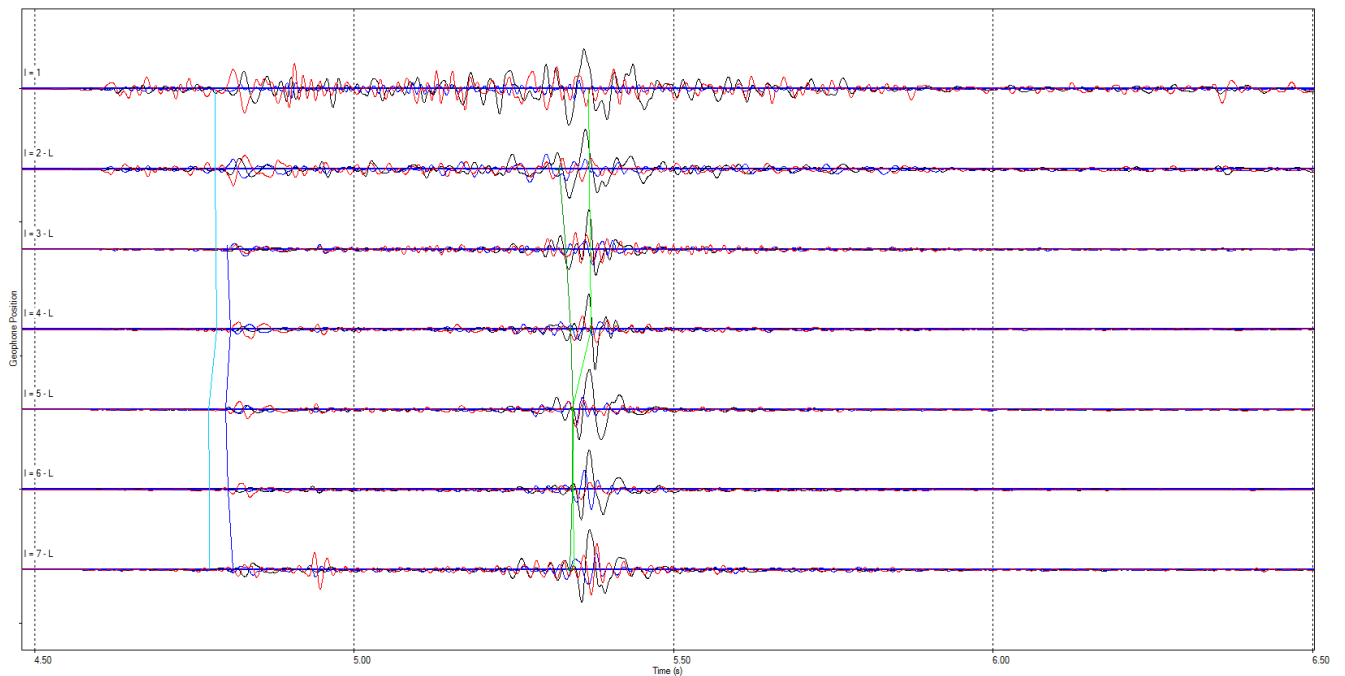


17/04/14 01:46:35

Stedum Well

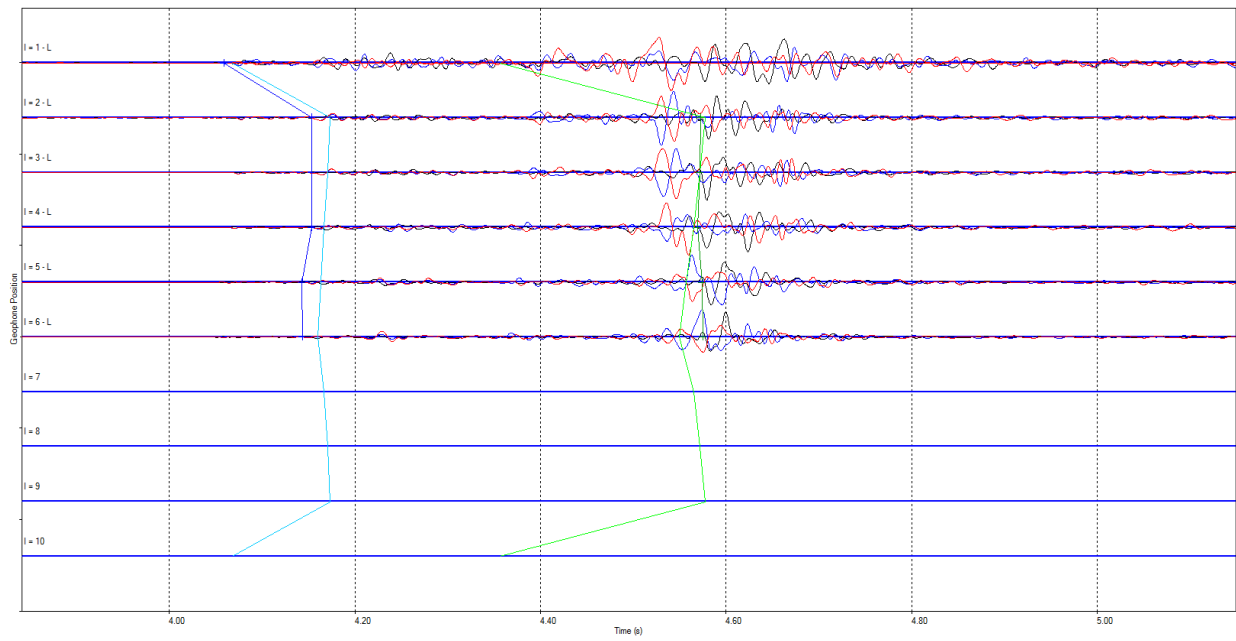


Zeerijp Well

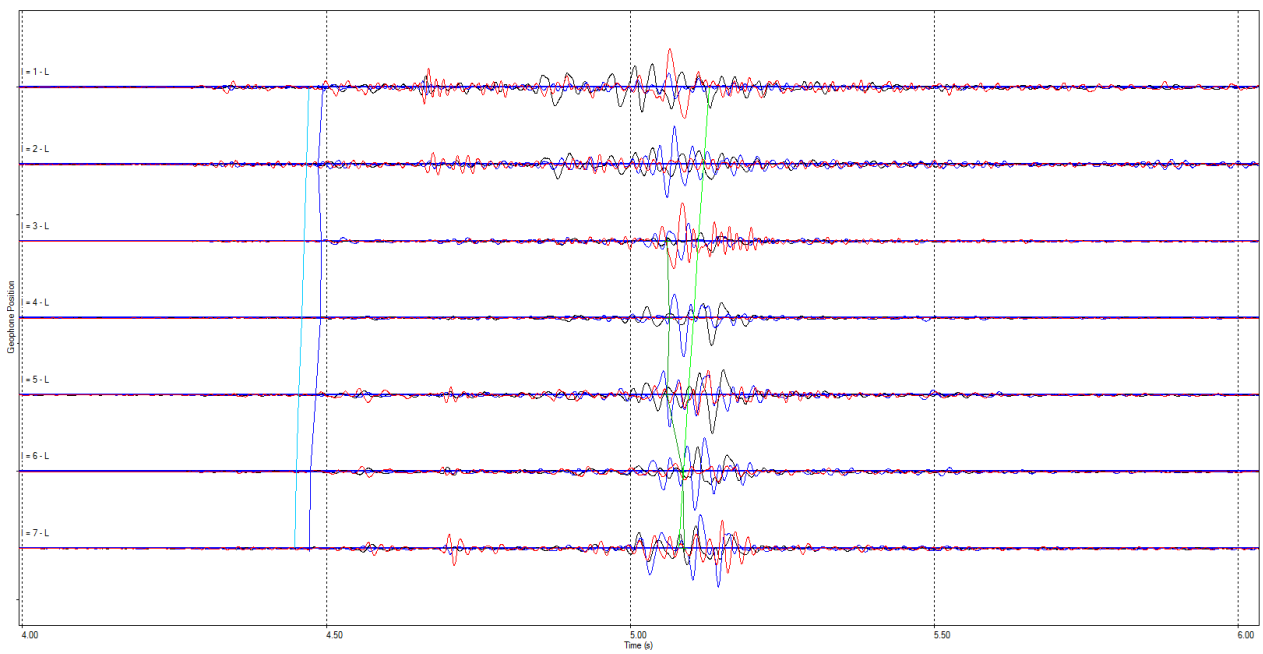


06/05/14 03:23:58

Stedum well

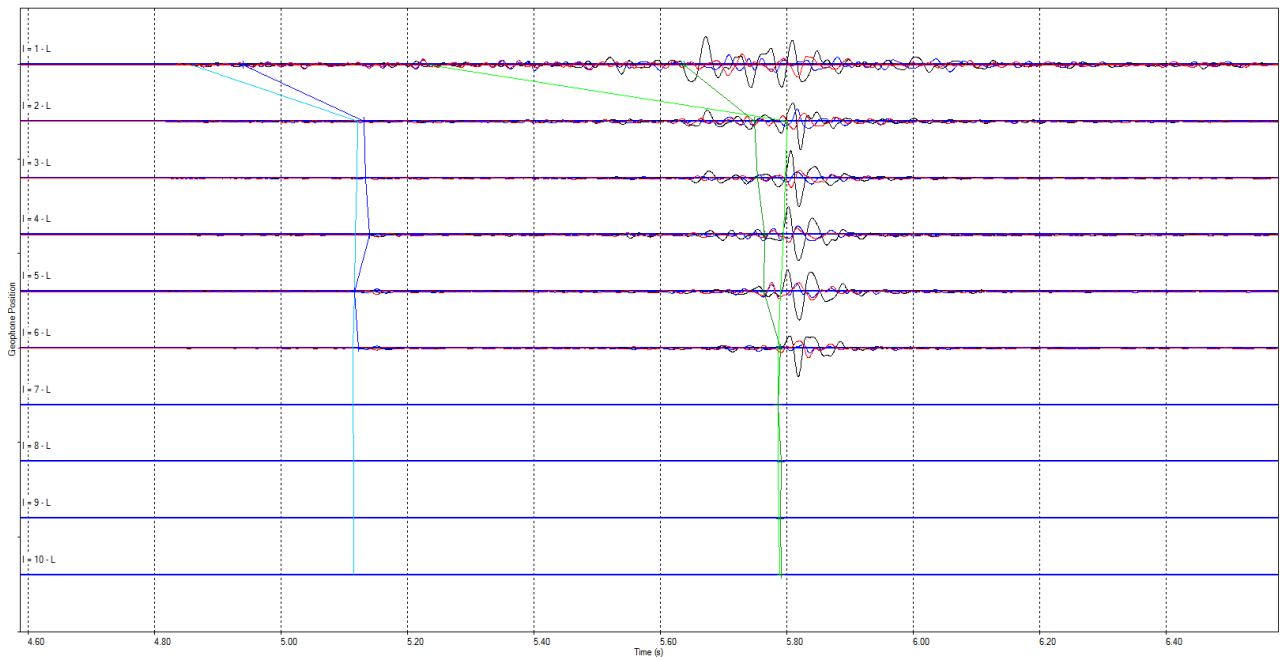


Zeerijp well

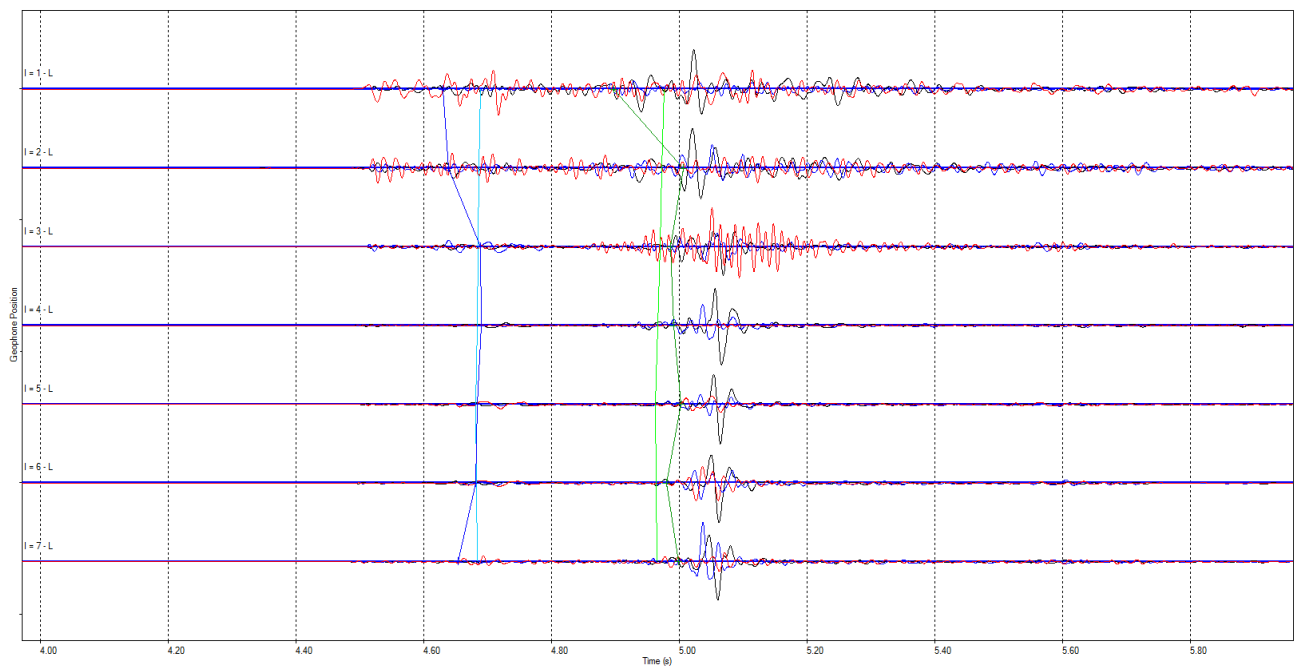


06/05/14 11:31:57

Stedum Well



Zeerijp well



Bibliographic information

Classification	Restricted
Report Number	
Title	A re-estimate of the earthquake hypocenter locations in the Groningen Gas Field.
Author(s)	Matt Pickering
Date of Issue	August 2014
Issuing Company	Shell International Exploration and Production P.O. Box 60 2280 AB Rijswijk The Netherlands

The copyright of this document is vested in Shell International Exploration and Production, B.V., The Hague, The Netherlands. All rights reserved.

Neither the whole nor any part of this document may be reproduced, stored in any retrieval system or transmitted in any form or by any means (electronic, mechanical, reprographic, recording or otherwise) without the prior written consent of the copyright owner.